[redacted]

[redacted]D

Saturn D Preliminary Design Study [U]

Final Report

Volume III

Appendices A through E

Report No. AS61-1017

1 November 1961

Contract NAS 8-1600

Prepared by

General Dynamics/Astronautics Division

General Dynamics Corporation

San Diego, California

for

George C. Marshall Space Flight Center

Huntsville, Alabama

[redacted]

[redacted]

[redacted] GROUP I

EX[redacted]DING:

DOD DIR 5200.10 DOES NOT APPLY

[redacted]

This [redacted] Sections 793 and 794. Its transmission or the revelation of its contents in [redacted]

Cy 4

[redacted]

This page intentionally left blank.

FOREWORD

Volume III contains Appendices A through E. Each of these appendices represents an investigation performed in support of a topic in Volume II, and either too detailed for incorporation in that volume or not as directly related to the principal line of study as Volume II material.

TABLE OF CONTENTS, VOLUME III

TABLE OF CONTENTS, VOLUME III (CONTINUED)

LIST OF ILLUSTRATIONS, VOLUME III

LIST OF TABLES, VOLUME III

LIST OF TABLES, VOLUME III (CONTINUED)

This page intentionally left blank.

APPENDIX A
SAMPLE SHIELDING CALCULATION

This appendix presents a sample shielding calculation that was conducted for the SN-IV nuclear engine. The calculation presented is generally representative of shielding studies that were performed for the engines with larger power, in that it was necessary to scale-up data previously obtained for engines of NERVA and PHOEBUS power levels; the need for scaling data arises from lack of definitive information on radiation fluxes in high power level reactors.

A.1 CALCULATION. The shield shape chosen for analysis was a frustum (see Figure A-1). The taper observed at points A and B starts at the edge of the active core. Points C and D are located at a point on the line joining the midpoint of the outside surface of the reactor and the tangent to the propellant tank.

The calculation for heat transfer of the SN-IV nuclear engine is based on and referenced to a 1500-MW unshielded reactor which deposits 1600 Btu/sec of heat into a full liquid-hydrogen tank, 257-inches in diameter. This reference 1500-MW reactor, subtends a solid angle of 0.785 steradians from the center of the reactor to the tank. The 1600 Btu/sec of heat consists of 720 Btu/sec from gamma rays, 500 Btu/sec from secondary gamma rays, and 380 Btu/sec from neutrons.

The SN-IV nuclear engine is powered by a 20,000-MW reactor; therefore:

$$\frac{20{,}000\ \text{MW}}{1{,}500\ \text{MW}} \times 1600\ \frac{\text{Btu}}{\text{sec}} = 21{,}300\ \text{Btu/sec},$$

the heat transferred by a 20,000 MW reactor which hypothetically has the same solid angle, separation distance and tank diameter as the 1500-MW reactor. Since the solid angle is a function of reactor/tank separation distance and tank diameter, heat transfer (Q) values for the 20,000-MW reactor were determined by multiplying 21,300 Btu/sec by the ratio of various solid angles to the reference solid angle (0.785 steradions). An LH_2 tank diameter of 380 inches and assumed reactor/tank separation distances of 175, 200, 225, 250, 275 and 300

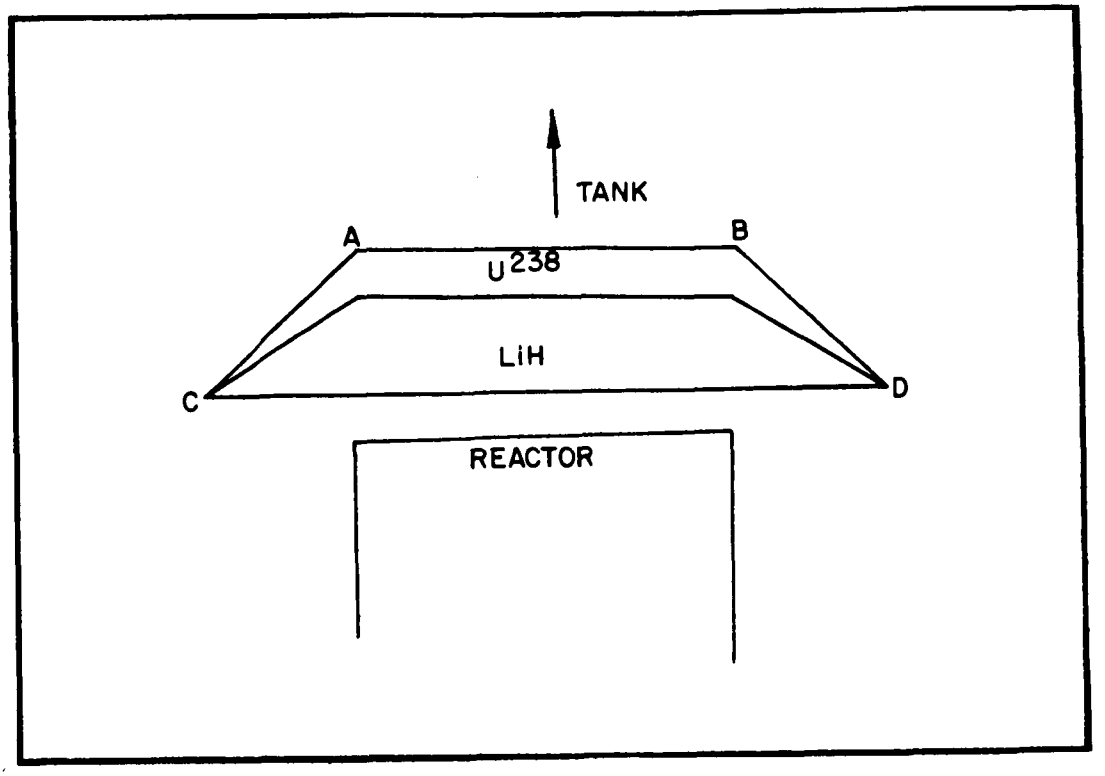

Figure A-1. Shield Geometry

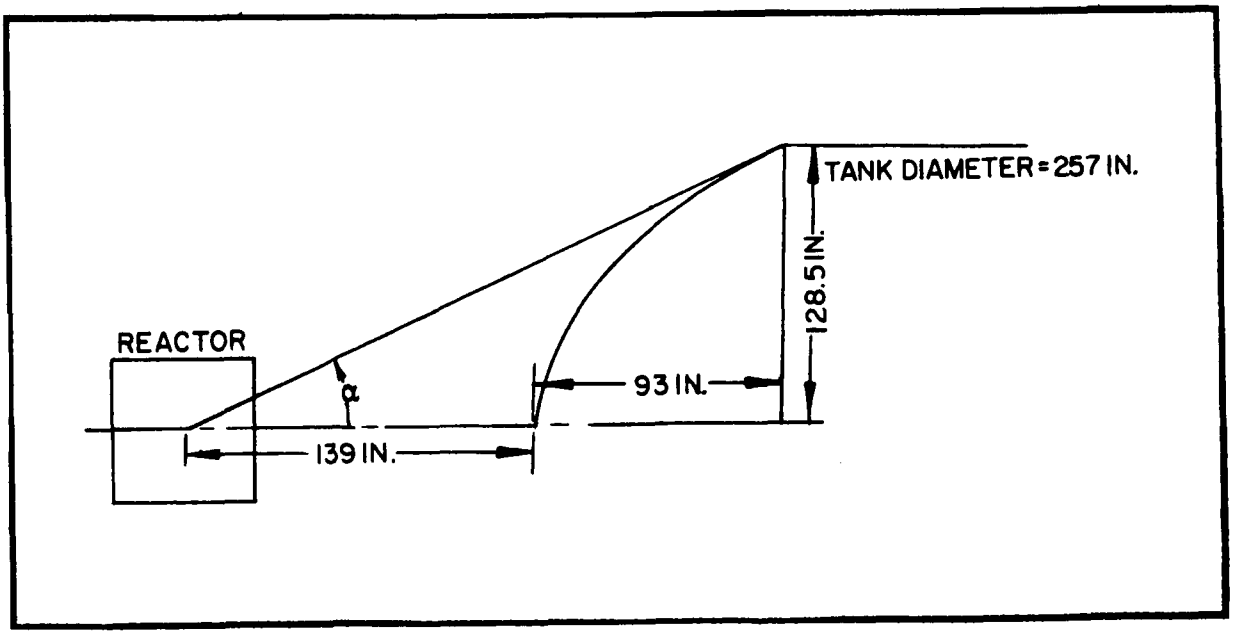

Figure A-2. Solid Angle Calculation

inches were used for heat transfer calculations of the SN-IV reactor. The reactor/tank separation distances are measured from the end of the reactor to the bottom of a hypothetical elliptical bulkhead which has an axis ratio of 1.38:1. This bulkhead is called hypothetical because the actual bulkhead may not have a 1.38:1 ratio; however the distance is measured relative to this surface.

The reference reactor/tank dimensions are shown in Figure A-2 and these dimensions are used for the reference solid angle calculation.

For a 1.38:1 elliptical bulkhead the minor axis is $\frac{128.5}{1.38}$ = 93 inches.

Separation distance from the reactor center to the bottom of the tank is 139 inches,

then, $\tan \alpha = \frac{128.5}{93+139} = \frac{128.5}{232} = 0.555$

and $\alpha = 29.0°$, $\alpha/2 = 14.5°$

The solid angle (Ω) = $4\pi \sin^2 \alpha/2 = 0.785$ steradians.

For the 20,000-MW SN-IV reactor with 380-inch tank, the geometry shown in Figure A-3 was used for the calculations as follows:

$\bar{EF} = 1/2L + S_1 + S_2$

where: L = 90 inches (reactor length),

S_1 = 175, 200, 225, 250, 275, and 300 inches (distance from the top of the reactor to the 1.38:1 bulkhead),

and S_2 = 190/1.38 = 137.8 inches.

From Figure A-3,

1/2 L = EH = 1/2 (90) = 45 inches

S_1 = HI = (175 + ΔSN)

where: Δ S = the increment of separation distances

and, N = 0, 1, 2, 3, 4, 5 (number of increments investigated).

then, $\bar{EF} = 45 + 137.8 + S_1 = 182.8 + S_1$

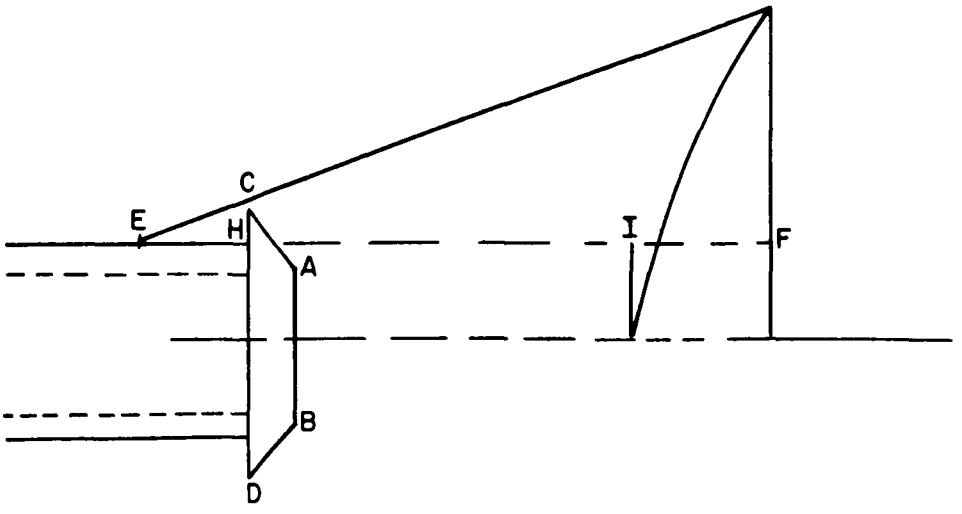

Figure A-3. Reactor - Shield - Tank Geometry

By calculating $\overline{EF}$ using the assumed separation distances, the solid angles can be obtained. For solid angles and data derived from these equations, see Table A-1.

Table A-1. Solid Angle for Six Values of S_1

$\overline{EF}$	Tan α	α(DEG)	$\alpha/2$(DEG)	$\sin^2 \alpha/2$	Ω	$\frac{\Omega}{0.785}$
357.8	0.532	28.0	14.0	0.0585	0.735	0.936
382.8	0.496	26.4	13.2	0.0520	0.654	0.832
407.8	0.466	25.0	12.5	0.0467	0.586	0.746
432.8	0.440	23.7	11.85	0.0421	0.530	0.675
457.8	0.415	22.5	11.25	0.0380	0.476	0.606
482.8	0.393	21.5	10.75	0.0348	0.436	0.556

Heat transfer values calculated by the method outlined are presented in Table A-2.

Table A-2. Values Used in Computing the Heat Transfered

SEPARATION DISTANCE, S_1 (in.)	$Q = \frac{\Omega}{0.785} \times 21300$ (BTU/SEC)	Q/C_p *$(\frac{LB-°F}{SEC})$
175	20000	8000
200	17720	7100
225	15900	6360
250	14400	5760
275	12920	5170
300	11880	4750

* $C_p = 2.5$

The rate of temperature rise as a function of time is shown in Table A-3.

The fraction (f) of propellant remaining after a particular time interval is noted in the Table. To correct for the radiation escaping from the surface of the thin layer of propellant left after 720 seconds of operation, a correction factor at f=0.01 must be calculated.

To calculate the depth of propellant of f=0.01
Tank radius = 190 inches
Tank cross section area = 7.31×10^5 cm^2
Propellant loading 800,000 lb = 3.63×10^8 gm
For a density of $\rho = 0.07$ gm/cm^3

$$\text{Vol of } LH_2 = \frac{3.63 \times 10}{7 \times 10^{-2}} = 5.18 \times 10^9 \text{ cm}^3$$

$$\text{then, } \frac{5.19 \times 10^9}{7.31 \times 10^5} = 7070 \text{ cm depth of } LH_2$$

which is 232 ft (full tank).

At f=0.01, LH_2 depth = 2.32 ft = 27.8 inches.

CONFIDENTIAL

Table A-3 Rate of Temperature Rise

f	M(f)	$\frac{Q}{C_p M(f)}$ 175 in.	$\frac{Q}{C_p M(f)}$ 200 in.	$\frac{Q}{C_p M(f)}$ 225 in.	$\frac{Q}{C_p M(f)}$ 250 in.	$\frac{Q}{C_p M(f)}$ 275 in.	$\frac{Q}{C_p M(f)}$ 300 in.	TIME (SEC)
1.0	800,000	0.0100	0.00887	0.00795	0.00721	0.00646	0.00594	0
0.75	600,000	0.01333	0.01182	0.0106	0.00962	0.00863	0.00791	182
0.5	400,000	0.0200	0.01775	0.01592	0.0144	0.01294	0.01188	364
0.25	200,000	0.0400	0.0355	0.0318	0.0288	0.02585	0.0238	545
0.1	80,000	0.100	0.0887	0.0795	0.0721	0.0646	0.0594	654
0.01	8,000	0.308	0.273	0.245	0.222	0.199	0.183	720

$$\frac{Q}{C_p M(f)} = {}^{\circ}F/_{Sec}$$

Let f be the fraction of propellant remaining after time t;

M(f) is the number of pounds of propellant remaining after time t.

Figures A-4 and A-4A are plots of the ratio of the fraction of gammas and neutrons absorbed as a function of LH_2 propellant.

From Figure A-4 read the gamma ratio = 0.146 at 27.8 inches.

From Figure A-4 read the neutron ratio = 0.832 at 27.8 inches.

To determine the heat absorption in 27.8 inches of LH_2 due to radiation, assume the secondary radiation can be added to the primary radiation. Full tank radiation = 1600 Btu (720 Btu/sec - gamma, 500 Btu/sec - secondary gamma and 380 Btu/sec - neutrons).

Then: (0.832) (380) + (0.146) (720 + 500) = 494 Btu/sec

The correction factor is:

$$C.F = \frac{494}{1600} = 0.308$$

The values at f = 0.01 in Table A-3 have been multiplied by the correction factor 0.308.

The values in Table A-3 are plotted as a function of burning time and are shown in Figure A-5. Integrating these values numerically, the total rise in temperature during the burning phase is obtained. The integration is accomplished by adding the °F/sec at the midpoint of each 100 second interval. The sum is then multiplied by the interval width to obtain °F of temperature rise (see Table A-4). The incremental pressure rise in relation to incremental temperature rise is presented in Table A-5. By dividing the applied temperature rise in Table A-5 by the unshielded temperature rise in Table A-4, the transmission factor is obtained (see Table A-6). The large total value in Table A-4 is the unshielded temperature rise, the smaller total value is the shielded temperature rise. A family of curves of attenuation versus LiH thickness for uranium thicknesses (see Table A-7) are shown in Figure A-6.

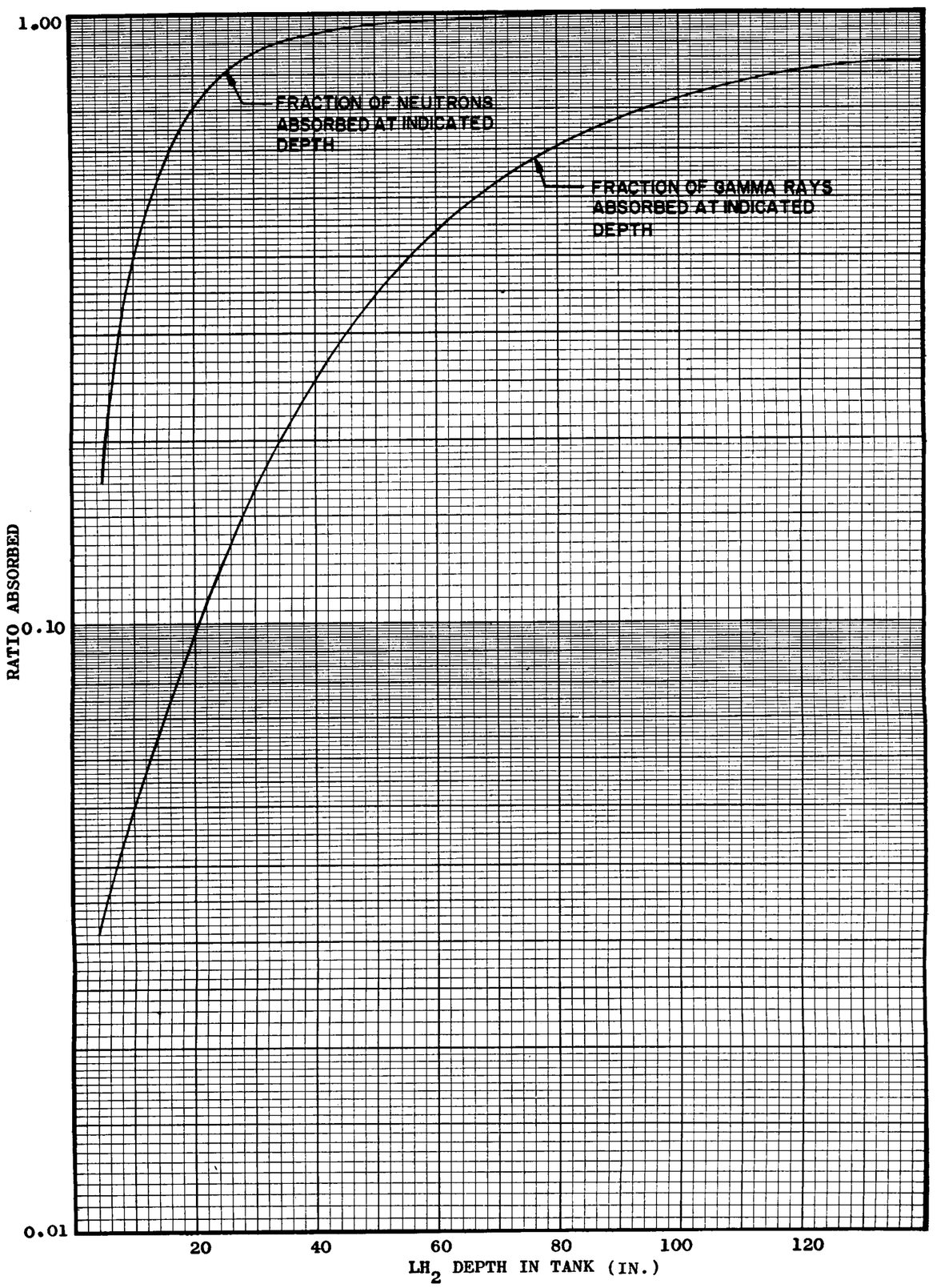

Figure A-4. Attenuation of Neutron and Gamma Radiation in LH_2 Propellant

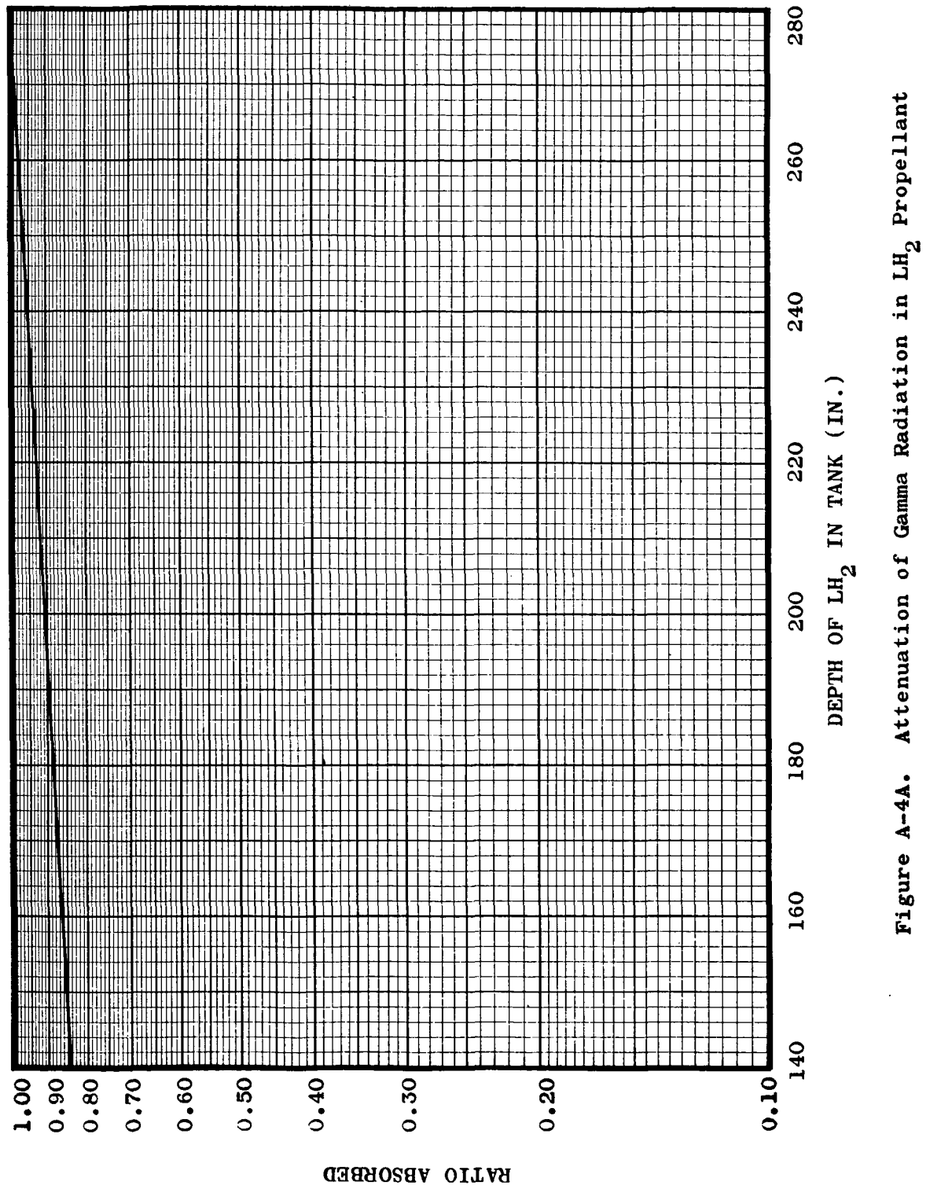

Figure A-4A. Attenuation of Gamma Radiation in LH_2 Propellant

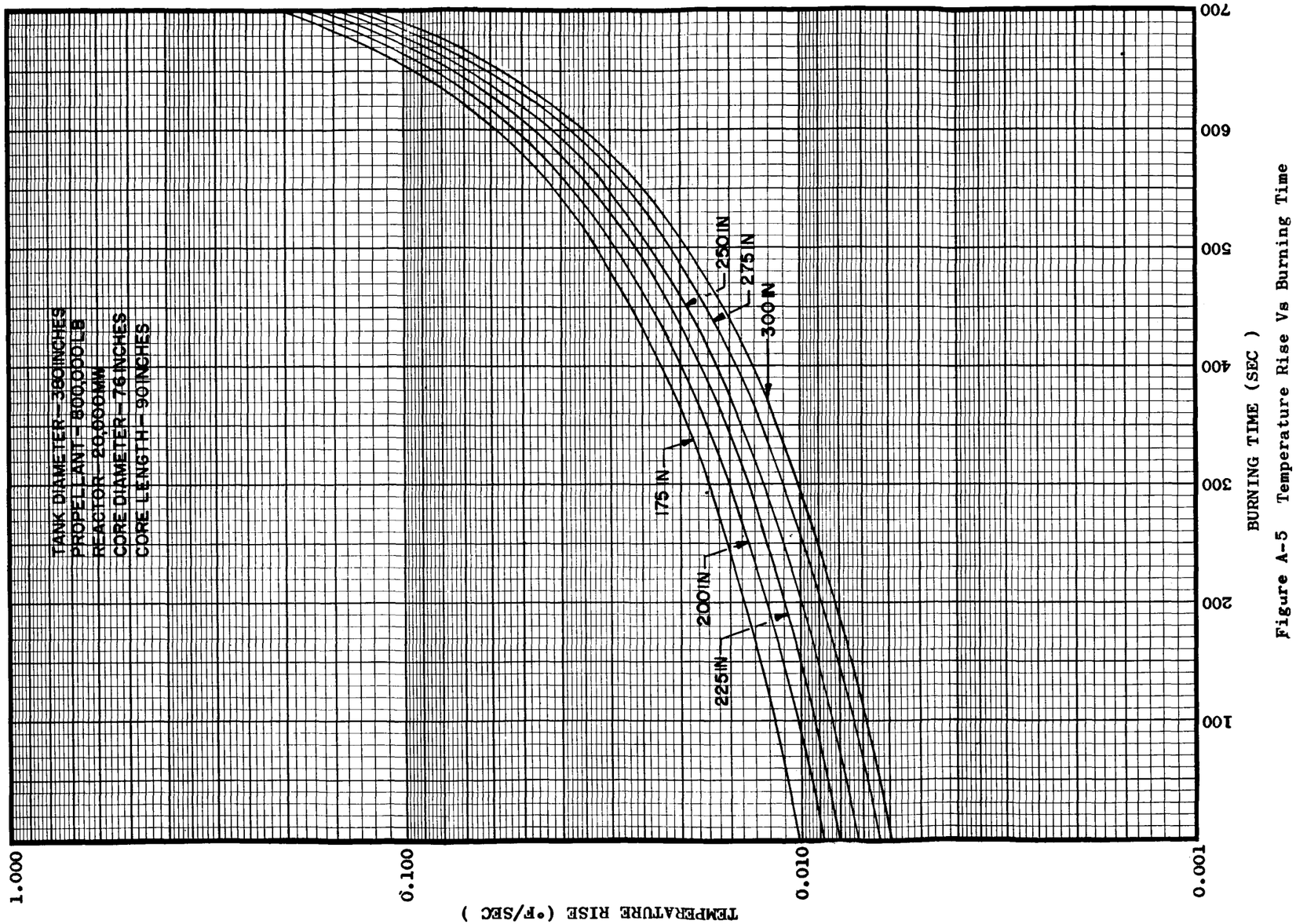

Figure A-5 Temperature Rise Vs Burning Time

Table A-4. Integration of Temperature Rise

	SEPARATION DISTANCES					
	175 in.	200 in.	225 in.	250 in.	275 in.	300 in.
	0.0106	0.00945	0.00855	0.00780	0.00700	0.00640
	0.0126	0.01100	0.01000	0.00915	0.00810	0.00745
	0.0151	0.01320	0.01200	0.01100	0.00980	0.00900
	0.0191	0.01690	0.01500	0.01390	0.0123	0.0114
	0.0261	0.02310	0.02070	0.01900	0.0170	0.0155
	0.0410	0.03700	0.03300	0.03000	0.0270	0.0246
	0.0870	0.08600	0.07600	0.07000	0.0620	0.0580
Totals	0.2115	0.19665	0.17525	0.16085	0.1432	0.1324
Total unshielded rise	21.15°F	19.66°F	17.52°F	16.08°F	14.32°F	13.24°F

Table A-5. Pressure Temperature Relation

Δ P (PSI)	Δ T °F
0.5	0.178
1.0	0.390
2.0	0.75
4.0	1.36
6.0	1.94

Table A-6. Transmission Factors

ΔP (PSI)	175 in.	200 in.	225 in.	250 in.	275 in.	300 in.
0.5	0.00842	0.00906	0.01015	0.01109	0.01240	0.01343
1.0	0.01849	0.01988	0.0223	0.0243	0.02725	0.0295
2.0	0.0354	0.0382	0.0428	0.0466	0.0523	0.0566
4.0	0.0644	0.0692	0.0775	0.0846	0.0949	0.1028
6.0	0.0917	0.0987	0.1105	0.1208	0.1352	0.1462

Table A-7. Thickness of LiH and U in CM

ΔP (PSI)	175 in.	200 in.	225 in.	250 in.	275 in.	300 in.	
0.5	34.0	33.0	34.0	34.7	33.8	32.4	LiH
	6.5	6.5	6.0	5.5	5.5	5.5	U
1.0	34.6	32.5	32.2	32.2	34.2	31.1	LiH
	4.5	4.5	4.25	4.25	3.75	3.75	U
2.0	28.9	29.3	31.6	28.0	28.3	31.8	LiH
	3.5	3.25	3.0	3.0	2.75	2.5	U
4.0	33.7	28.1	31.8	25.5	26.2	23.2	LiH
	2.25	2.25	2.0	2.0	1.75	1.75	U
6.0	30.2	24.8	26.8	22.2	24.2	32.0	LiH
	1.75	1.75	1.5	1.5	1.25	1.0	U

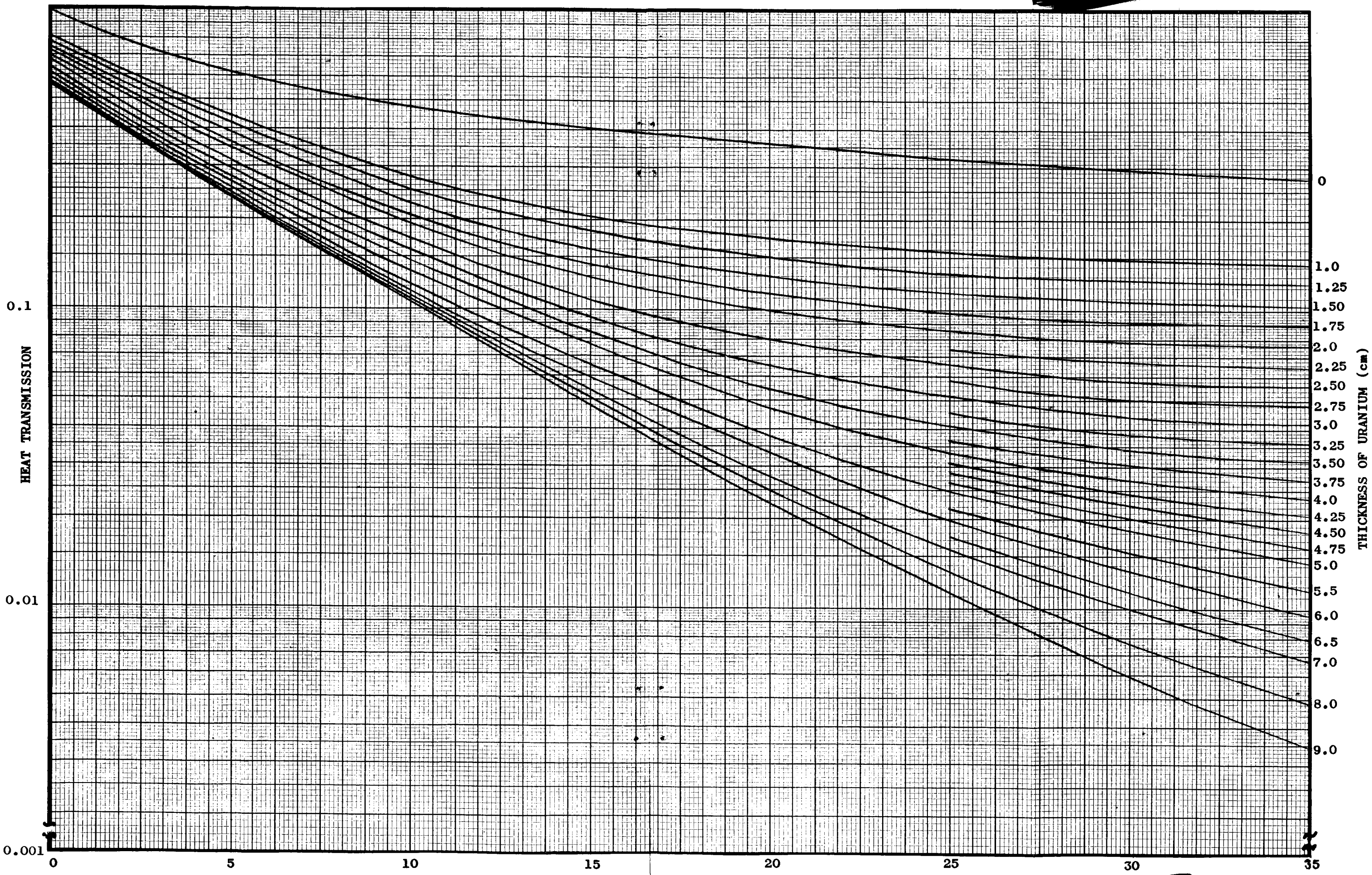

Figure A-7. Attenuation of Heat Vs LiH Thickness and Uranium Thickness

The values in Table A-7 are converted to shield weight (in pounds) by multiplying the thickness by a derived constant. The volume of a frustum is given by:

$$V = 1/3\ (A_1 + A_2 + \sqrt{A_1\ A_2})\ h$$

where: A_1 and A_2 are the areas of the two bases and h is the thickness. Since the radii of A_1 and A_2 are known, V/h can be calculated. Using the density of LiH as 0.507 gm/cm^3 (30 percent reduced for void fraction) and 13.1 gm/cm^3 for U also 30 percent reduced, the density (ρ) is calculated in lb/cm^3.

Then: $\frac{V}{h}\ (\rho) = \frac{V}{h}$ x lb/cm^3 = lb/cm (weight of shield per cm of material),

$\frac{V}{h}$ = 46,400, 45,226, 43,993, 43,090, 42,213, 41,450 cm^2

Multiplying these values by the densities of LiH and U,

LiH/cm = 51.9, 50.6, 49.2, 48.4, 47.4, 46.4 lb/cm

U/cm = 1340, 1308, 1270, 1249, 1220, 1198 lb/cm

Then, lb/cm x thicknesses in Table A-7 = shield weight in pounds (see Table A-8).

A plot of shield weight versus separation distance appears in Volume II, Section 3.8 (Figure 3-73).

Table A-8. Shield Weights in Pounds

ΔP PSI	175 IN.	200 IN.	225 IN.	250 IN.	275 IN.	300 IN.		
0.5	1760	1670	1675	1680	1600	1500	lb	LiH
	8710	8500	7610	6860	6700	6590	lb	U
Total	10470	10170	9285	8440	8300	8090	lb	
1.0	1795	1641	1585	1558	1622	1441		
	6040	5890	5400	5300	4570	4500		
Total	7835	7531	6985	6858	6192	5941		
2.0	1500	1480	1555	1354	1340	1475		
	4700	4250	3810	3740	3350	3000		
Total	6200	5730	5365	5094	4690	4475		
4.0	1749	1420	1565	1230	1240	1076		
	3020	2940	2540	2500	2140	2100		
Total	4769	4360	4105	3730	3380	3176		
6.0	1568	1253	1320	1072	1146	1485		
	2340	2290	1905	1870	1525	1198		
Total	3908	3543	3225	2942	2671	2683		

This page intentionally left blank.

APPENDIX B

SOLAR FLARE RADIATION DAMAGE IN MATERIALS

B.1 GENERAL. In order to compare the radiation damage due to Van Allen belt high ($E > 100$ Mev) and low ($E < 100$ Mev) energy protons to the radiation damage due to a solar flare, the effects of each will be calculated and tabulated.

The particular solar flare which will be chosen for this study is the Class 3+ flare of 10 May 1959 since it was the largest 3+ flare recorded during this solar cycle.

Attention is drawn to the fact that a Class 4 flare such as the one of 23 February 1956 was not considered in this study. In addition, no consideration will be given to shielding possibilities in the calculation of atomic displacements.

B.2 APPROACH AND ANALYSIS

B.2.1 Basic Theory of Collision and Energy Loss. The basic problem to be considered in this section is the means by which energy is transferred and the rate at which energy is transferred from a particle traveling with velocity, v, to an atom assumed to be at rest.

There are three types of collisions which a charged particle* can experience.

a. Rutherford.
b. Hard-sphere type.
c. The gray area in which the collisions are neither Rutherford nor hard sphere.

B.2.1.1 Rutherford Collisions. In the high energy range the collisions are primarily of the Rutherford type. According to the presentation of Dienes and Vineyard of the analysis by Bohr, the

* Charged particles other than electrons. The electrons will be treated separately.

approaching charged particle interacts with the stationary atom with a screened coulomb potential of the form:

$$V(r) = \frac{Z_1 Z_2 e^2}{r} e^{-r/a} \qquad \text{B-1}$$

where: Z_1 = atomic number of the moving particle with total charge $Z_1 e$

Z_2 = atomic number of the stationary atom with total charge $Z_2 e$.

r = separation distance

a = screening radius

$$a \cong a_o / (Z_1^{2/3} + Z_2^{2/3})^{1/2} \qquad \text{B-2}$$

$a_o \cong$ Bohr radius of hydrogen = 5.29×10^{-9} cm.

Since energy is conserved in Rutherford Collisions, one may apply conservation of energy in scattering calculations, and utilize this screening potential as derived by Bohr. For example, if the screening is neglected * and a Coulomb potential of the form (B-3) is used;

$$V(r) = \frac{Z_1 Z_2 e^2}{r} \qquad \text{B-3}$$

and the classical distance of closest approach can be obtained as follows:

Initial Energy of incoming particle = Energy of scattered particle + V(r)

$$1/2\ MV^2 = 1/2\ MV'^2 + \frac{Z_1 Z_2 e^2}{r} \qquad \text{B-4}$$

If all the energy is transferred, then $V' = 0$, and the distance of closest approach is:

$$r = \frac{2Z_1 Z_2 e^2}{MV^2} \qquad \text{B-5}$$

* Screening accounts for the Coulomb interaction between the electron cloud surrounding the stationary nucleus and the incoming particle.

Generally the reduced mass concept is used, i.e., M in B-5 is replaced by μ, which is:

$$\mu = \frac{Mm}{M+m} \qquad \text{B-6}$$

In order to more clearly define the energy regions in which the specialized cases of collisions apply, the parameter b/a is introduced such that:

$$b = \frac{2Z_1 Z_2 e^2}{\mu V^2} \qquad \text{B-7}$$

and a is defined by B-2. When the reduced mass concept is used, r, the distance of closest approach neglecting screening becomes b. Examination of B-1 in this light then gives insight into the types of collisions and possible energies, since b is an indication of the reciprocal of the initial energy of the incident particle. If $b/a \ll 1$, the exponential function may be neglected and the interaction is of the Rutherford type. This type will now be considered.

A proper measure of the probability that the incoming particle and the stationary nucleus will interact at all is the cross section which the incoming particle sees. Following Dienes and Vineyard, the cross section for Rutherford scattering valid for Coulomb interactions is:

$$\int_T d\sigma = \int_T 4\pi \; a_o^2 \left(\frac{M_1}{M_2}\right) Z_1^2 \, Z_2^2 \left(\frac{E_R}{E}\right)^2 \frac{dT}{T^2} \qquad \text{B-8}$$

where: M_1 = mass of incoming particle

M_2 = mass of stationary nucleus

T = energy transferred to stationary nucleus

$d\sigma$ = differential cross section for energy transfer T to T + dT

E_R = Rydberg energy = 13.60 ev

E = energy of incoming particle

The particular cross section of interest in this case is the displacement cross-section, and since it is generally assumed that there is a minimum energy* E_d below which no displacements occur, then:

$$\sigma_d = \int_{E_d}^{T_m} d\sigma = \frac{16\pi\, a_o^2\, Z_1^2\, Z_2^2\, M_1^2\, E_R^2}{(M_1+M_2)^2\, E_d\, T_m} \qquad \text{B-10}$$

Assuming that $T_m/E_d \gg 1$. Equation B-10 is valid for $b \ll a$.

$$T_m = \frac{4M_1M_2}{(M_1+M_2)^2}$$

E = the maximum energy transfer allowable by the conservation of energy and momentum.

The degradation in energy/unit distance suffered by the incident particle due to these displacement collisions alone is:

$$\left(\frac{dE}{dX}\right)_d = N_o \int_{E_d}^{T_m} T \frac{d\sigma}{dT}(T)\, dT \qquad \text{B-11}$$

$$\left(\frac{dE}{dX}\right)_d = N_o \int_{E_d}^{T_m} T\, C\, \frac{dT}{T^2} \qquad \text{B-12}$$

where: $C = 4\pi\, a_o^2 (M_1/M_2)\, Z_1^2\, Z_2^2\, (E_R^2/E)$

and N_o = Atom number density of the target

$$\left(\frac{dE}{dX}\right)_d = N_o\, C \left(\ln \frac{T_m}{E_d}\right) \qquad \text{B-13}$$

Since the energy loss due to displacements alone is in a rather restricted region, the energy loss over the entire Coulomb region will be calculated for the purpose of later comparing with ionization losses. According to the method of Seitz and Koehler:

* This minimum energy is assumed throughout the report as 25 ev.

$$\left(\frac{dE}{dX}\right)_c = N_o \int_{T_a}^{T_m} T \frac{d\sigma(T)}{dT} dt \qquad \text{B-14}$$

$$\left(\frac{dE}{dX}\right)_c = N_o C \ln\left(\frac{T_m}{T_a}\right) \qquad \text{B-15}$$

where: T_a is the larger of T_a' or T_a''

$$T_a' \cong 4 Z_1^2 Z_2^2 \frac{E_R^2}{E} \frac{M_1}{M_2} \left(\frac{a_o}{a}\right)^2 \qquad \text{B-16}$$

$$T_a' \cong 4 Z_1^2 Z_2^2 \frac{E_R^2}{E} \frac{M_1}{M_2} (Z_1^{2/3} + Z_2^{2/3}) \qquad \text{B-17}$$

$$K = 2Z_1 Z_2 \left(\frac{E_R}{E} \cdot \frac{M_1}{M_e}\right) > 1 \qquad \text{B-18}$$

and

$$T_a \cong \frac{m}{M_2} (Z_1^{2/3} + Z_2^{2/3}) E_R \quad \text{for } K < 1 \qquad \text{B-19}$$

where: m_e is the mass of the electron.

If the energy of the incident charged particle is greater than the ionization threshold E_i, the energy loss due to ionization begins to become important. Dienes and Vineyard present a formula which accounts for the energy loss due to ionization between E_i and below the relativistic region. This formula is as follows.

$$-\left(\frac{dE}{dX}\right)_e = (4\pi e^4 Z_1'^2 / Mv^2) N_o Z_2' \ln(2Mv^2/J) \qquad \text{B-20}$$

where:

$J \cong 10 Z_2$ ev.

Z_2' = the number of electrons whose excitation energy is less than $(M/M_1)E$.

$Z_1'e$ = charge of the moving atom.

Finally, when the energy of the charged particle reaches the relativistic range, Seitz and Koehler point out that the ionization loss is given by:

$$\left(\frac{dE}{dx}\right)_c \cong \frac{8\pi N_o Z_1^2 E_R^2 a_o^2 Z_2}{M V^2}\left[\log \frac{(M_1 V^2)^2}{(1-\beta^2)Z_2^2 I^2} - \beta^2\right] \qquad \text{B-21}$$

If $\frac{Z_1}{137\beta}$ is negligible in comparison with 1, then:

$$\beta = V/C \qquad IZ \cong 13.6\, Z_1 \qquad \text{B-22}$$

B.2.1.2 Hard-sphere Collisions. In the hard-sphere interactions, the incoming particle is in the low energy range and the energy will be lost to the stationary atoms primarily through inelastic collisions. The parameter $b/a \gg 1$ and the screening cannot be neglected in this case; however, the common practice is to treat the collisions from a classical mechanics point of view. The reader is referred to Seitz and Koehler for the subtle details of the failure of classical mechanics in hard-sphere collision.

B.2.1.3 Intermediate-Energies. The intermediate energy range ($b \backsim a$) where neither Rutherford nor hard-sphere collisions take place is extremely complicated. The means by which this region has been investigated has been as follows: Rutherford scattering occurs for $b/a \ll 1$ and the scattering law is of the form:

$$d\sigma \propto \frac{dT}{T^2} \qquad \text{B-23}$$

On the other hand, in hard-sphere collisions $b/a \gg 1$, and the scattering law is of the form:

$$d\sigma \propto dT \qquad \text{B-24}$$

$$\frac{dE}{dX}_c = N_o \int_{T_a}^{T_m} T \frac{d\sigma(T)}{dT} dt \qquad \text{B-14}$$

$$\frac{dE}{dX}_c = N_o C \ln\left(\frac{T_m}{T_a}\right) \qquad \text{B-15}$$

where: T_a is the larger of T_a' or T_a''

$$T_a' \cong 4 Z_1^2 Z_2^2 \frac{E_R^2}{E} \frac{M_1}{M_2} \left(\frac{a_o}{a}\right)^2 \qquad \text{B-16}$$

$$T_a' \cong 4 Z_1^2 Z_2^2 \frac{E_R^2}{E} \frac{M_1}{M_2} (Z_1^{2/3} + Z_2^{2/3}) \qquad \text{B-17}$$

$$K = 2Z_1 Z_2 \left(\frac{E_R}{E} \cdot \frac{M_1}{M_e}\right) > 1 \qquad \text{B-18}$$

and

$$T_a \cong \frac{m}{M_2} (Z_1^{2/3} + Z_2^{2/3}) E_R \quad \text{for } K < 1 \qquad \text{B-19}$$

where: m_e is the mass of the electron.

If the energy of the incident charged particle is greater than the ionization threshold E_i, the energy loss due to ionization begins to become important. Dienes and Vineyard present a formula which accounts for the energy loss due to ionization between E_i and below the relativistic region. This formula is as follows.

$$-\frac{dE}{dX}_e = (4\pi e^4 Z_1'^2 / Mv^2) N_o Z_2' \ln(2Mv^2/J) \qquad \text{B-20}$$

where:

$J \cong 10 Z_2$ ev.

Z_2' = the number of electrons whose excitation energy is less than $(M/M_1)E$.

$Z_1'e$ = charge of the moving atom.

Finally, when the energy of the charged particle reaches the relativistic range, Seitz and Koehler point out that the ionization loss is given by:

$$\left(\frac{dE}{dx}\right)_c \cong \frac{8\pi N_o Z_1^2 E_R^2 a_o^2 Z_2}{M V^2}\left[\log \frac{(M_1 V^2)^2}{(1-\beta^2)Z_2^2 I^2} - \beta^2\right] \qquad \text{B-21}$$

If $\frac{Z_1}{137\beta}$ is negligible in comparison with 1, then:

$$\beta = V/C \qquad IZ \cong 13.6\, Z_1 \qquad \text{B-22}$$

B.2.1.2 Hard-sphere Collisions. In the hard-sphere interactions, the incoming particle is in the low energy range and the energy will be lost to the stationary atoms primarily through inelastic collisions. The parameter $b/a \gg 1$ and the screening cannot be neglected in this case; however, the common practice is to treat the collisions from a classical mechanics point of view. The reader is referred to Seitz and Koehler for the subtle details of the failure of classical mechanics in hard-sphere collision.

B.2.1.3 Intermediate-Energies. The intermediate energy range ($b \backsim a$) where neither Rutherford nor hard-sphere collisions take place is extremely complicated. The means by which this region has been investigated has been as follows: Rutherford scattering occurs for $b/a \ll 1$ and the scattering law is of the form:

$$d\sigma \propto \frac{dT}{T^2} \qquad \text{B-23}$$

On the other hand, in hard-sphere collisions $b/a \gg 1$, and the scattering law is of the form:

$$d\sigma \propto dT \qquad \text{B-24}$$

which simply means that all energy transfers from 0 to T_m are equally probable.

The scattering law for the intermediate energies (b ~ a) is somewhere between the two, and is conventionally taken as:

$$d\sigma \propto \frac{dT}{T^n} \qquad 1 < n < 2 \qquad \text{B-25}$$

This cross section is valid for the following energy ranges

$$b = \frac{2Z_1 Z_2 e^2}{\mu V^2}$$

$$a = \frac{a_o}{(Z_1^{2/3} + Z_2^{2/3})^{1/2}}$$

and for b = a

$$\text{then:} \quad 2 Z_1 Z_2 \cdot 2 E_R a_o = \frac{a_o M_1 M_2 V_A^2}{(M_1+M_2)(Z_1^{2/3}+Z_2^{2/3})^{1/2}}$$

where: $\frac{1}{2} M_1 V_A^2$ is the energy E_A for which b = a

Hence

$$E_A = \frac{2 Z_1 Z_2 E_R (M_1+M_2)}{M_2} (Z_1^{2/3}+Z_2^{2/3})^{1/2} \qquad \text{B-26}$$

B.2.2 Mechanisms of Dosage Criteria for Correlation. The passage of nuclear radiation through matter can not only change the electronic configuration of an atom, thus causing ionization, but, it can also produce actual displacements of the atom from its host lattice as pointed out in Section B.2.1. The total energy loss per centimeter of path length experienced by the colliding particle in the encounter is:

$$\frac{dE}{dx} = \left(\frac{dE}{dx}\right)_e + \left(\frac{dE}{dx}\right)_c \qquad \text{B-27}$$

where:
the subscripts e and c denote energy loss due to ionization and coulomb encounters (elastic collisions) respectively.

Since the purpose of this report is to investigate radiation damage to materials due to solar flares, the primary interest will be devoted to protons, neutrons and electrons. Particles heavier than protons will not be considered.

The general approach which will be used will be to assume that the particular damage parameter being investigated is directly a function of the number of atomic displacements plus effects caused by ionization, cf., Section B.2.3. In this way then extrapolations can be made on the basis of existing data.

B.2.3 Displacement Calculations - Low Energy. The basic equation governing the number of displacements which will be produced by the passage of charged or atomic particles through matter is:

$$N_d = \phi t \sigma_d N_o \bar{\nu} \qquad \text{B-28}$$

where, in accordance with the nomenclature in Dienes and Vineyard:

N_d = total number of atomic displacements per unit volume
ϕ = number of bombarding particles per unit area per unit time
t = bombardment time
σd = microscopic displacement cross section
N_o = particle number density that is,

$$N_o = \frac{N_A \rho}{A}$$

where: N_A = Avogadro's number B-29
ρ = Density
A = Atomic weight

$\bar{\nu}$ = mean number of displaced atoms per primary knock-on , averaged over the energy spectrum of the primary knock-on.*

* This is not quite true in the case of charged particles as will be seen shortly.

Notice that N_d may be also written as:

$$N_d = N_p \cdot \overline{\nu} \qquad \text{B-30}$$

where N_p = number of primary knock-ons produced per unit volume ($N_p = \phi\, t\, \sigma_d\, N_o$).

The energy sensitive portions of (B-28) which must be analyzed on a separate basis are σ_a and $\overline{\nu}$. At present, a theory has not been developed which will account for displacements produced for very high energy interactions, that is, the energy of the bombarding particle being greater than 100 Mev. Some work has been done in theory of displacements by relativistic electrons and will be presented in Section B.2.3.2.1. The following sections are devoted to the separate analyses of σ_d and $\overline{\nu}$.

B.2.3.1 Protons

B.2.3.1.1 Non-relativistic. From Section B.2.1.1, the displacement cross section for a charged particle is:

$$\sigma_d = \frac{16\ a_o^2\ Z_1^2\ Z_2^2\ M_1^2\ E_R^2}{(M_1 + M_2)^2\ E_d\ T_m} \qquad \text{B-31}$$

for $T_m >> E_d$. The quantity E_A, defined by (B-26), is the limiting parameter which determines the applicability of (B-31), therefore, E_A will now be computed for protons.

$$E_A = \frac{27.2\ Z_2\ (1+M_2)}{M_2}\ (1+Z_2^{2/3})^{1/2} \qquad \text{B-32}$$

Therefore, if E (proton)$>>$ E_A, then (B-31) applies.

At this point, some time will be devoted to a discussion of presently available models for the average number of displacements produced per primary knock-on.

Since the incident particle is charged, the average energy transferred is no longer high but very close to E_d, the common averaging technique

$$\bar{f} = \frac{\int f dA}{\int dA}$$

where: A is some parameter over which f is to be averaged, is no longer applicable.

Several models are available at present, to account for this non-linearity; however, the author has chosen to use the model of Kinchin and Pease because of its simplicity and because of its general acceptance.

Following Dienes and Vineyard again, if a probability function P(E) is defined so that once there is a collision, the probability per unit energy interval that the primary knock-on received an energy E is this function P(E), and that the probability for displacing the atom with energy transfer E is p(E), then P(E) is given by:

$$P(E) = \frac{\sigma(E)\ p(E)}{\int_0^\infty \sigma(E)\ p(E)dE} \qquad \text{B-33}$$

where $\sigma(E)$ is the cross section for energy transfer E.
therefore:

$$\bar{\nu} = \int_0^\infty \nu(E)\ P(E)dE \qquad \text{B-34}$$

In accordance with the Kinchin-Pease model, if it is assumed that the target atom cannot be displaced from its host lattice if the energy E transferred is less than E_d, and if it is assumed that atoms with energies between E_d and $2E_d$ are displaced but cannot produce further displacements while atoms of energy greater than $2E_d$ are always transferred, then the number of displacements $\nu(E)$ is:

$$\nu(E) = 0 \qquad 0 \leq E \leq E_d \qquad \text{B-35a}$$

$$\nu(E) = 1 \qquad E_d \leq E \leq 2E_d \qquad \text{B-35b}$$

$$\nu(E) = \frac{E}{2E_d} \quad \text{for } E > 2E_d \qquad \text{B-35c}$$

It should be noted that the $\nu(E)$'s are actually obtained by solving a simple integral equation with suitable boundary conditions. The reader is referred to either Dienes and Vineyard, or Seitz and Koehler for the details of the solution of integral equations for the number

of displacements in a monatomic solid.

On the other hand P(E) is defined as follows:

$$p(E) = 0 \qquad \text{for } E < E_d \qquad \text{B-36a}$$

and

$$p(E) = 1 \qquad \text{for } E > E_d \qquad \text{B-36b}$$

then from the fact that $\sigma(E) \propto \frac{1}{E^2}$ for Rutherford collisions:

$$P(E) = \frac{\frac{K_1}{E^2}}{K_1 \int_{E_d}^{T_m} \frac{dE}{E^2}} \qquad P(E) = \left(\frac{T_m E_d}{T_m - E_d}\right) E^{1/2} \qquad \text{B-37}$$

Now then from (B-34), (B-35) and (B-37)

$$\bar{\nu} = \int_{E_d}^{2E_d} \frac{(T_m E_d)}{(T_m - E_d)} \frac{1}{E^2} \cdot dE + \int_{2E_d}^{T_m} \frac{(T_m E_d)}{(T_m - E_d)} \frac{dE}{E \cdot 2E_d}$$

$$\bar{\nu} = \frac{T_m}{T_m - E_d} \left[\frac{E_d}{E_d} - \frac{E_d}{2E_d} + \tfrac{1}{2} \ln \frac{(T_m)}{(2E_d)} \right]$$

$$\bar{\nu} = \frac{T_m}{2(T_m - E_d)} \left[1 + \ln \left(\frac{T_m}{2E_d} \right) \right] \qquad \text{B-38}$$

B.2.3.1.2 High Energies. The theory governing the calculation of the displacement cross sections and the number of displacements $\bar{\nu}$ becomes quite inadequate at energies even lower than relativistic.

For energies above E_i, the ionization threshold and up to 100 Mev, the calculation for $\bar{\nu}$ is as follows:
At energies this high, the number of displacements produced is directly a function of the energy expended in elastic collisions. Huwitz and Clark, as reviewed by Dienes and Vineyard, defined a function which is the amount of energy loss in elastic collisions (only) in slowing down from an energy E to 0 as:

$$G(E) = \int_0^E \left[\frac{\left(\frac{dE}{dx}\right)_c}{\left(\frac{dE}{dx}\right)_c + \left(\frac{dE}{dx}\right)_e} \right] dE \qquad \text{B-39}$$

Following Hurwitz and Clark and using the probability function defined by (B-33), the probability P(E) that, given a collision, the energy transferred from the proton to the atom is E, then as before:

$$P(E) = \frac{\sigma\ (E)\ p(E)}{\int_0^\infty \sigma\ (E) p(E) dE} \qquad \text{B-40}$$

and as before:

$$= \frac{(T_m\ E_d)}{(T_m - E_d)} \frac{1}{E^2} \qquad \text{B-41}$$

for $E_d < E < T_m$, therefore:

$$\overline{G}\ (E) = \frac{T_m\ E_d}{T_m - E_d} \frac{1}{E^2} \int_0^{T_m} G(E)\ dE \qquad \text{B-42}$$

The best estimate for $\overline{\nu}\ (e)$ is simply:

$$\overline{\nu}\ (E) = \frac{\overline{G}\ (E)}{2E_d}. \qquad \text{B-43}$$

where the functions in G(E) are defined by equations (B-15) and (B-20) in the region of interest. A graphical integration will yield the required $\overline{\nu}\ (E)$. A rough estimate of $\overline{\nu}\ (E)$ in this energy range is:

$$\overline{\nu}\ (E) = \frac{E_i}{2E_d} \qquad \text{B-44}$$

A calculation of either of the parameters σ_d or $\overline{\nu}$ (E above 100 Mev) has not been accomplished to date because of the inadequacy of existing theories. The main reasons being that small scale spallation products are formed in addition to the production of star reactions. In particular, Denny and Pomeroy indicate, on the basis of experimental evidence of Smoluchowski's, that protons above 100 Mev will

produce between 1 to 5 times as many defects/cm^3 as the lower energy protons generally considered important.

B.2.3.2 Electrons

5.2.3.2.1 Relativistic. In the case of electrons the main concern in displacement calculations is electrons of relativistic energies. The maximum emergy which can be transferred in this case becomes:

$$T_m = \frac{2(E + 2\,mc^2)}{M_2\,C^2} E \qquad \text{B-45}$$

where it was assumed that $m \ll M_2$ and $E \ll M_2 C^2$. The following cross-sections are applicable in the T_m energy ranges indicated:

$$\sigma_d = \frac{16\pi a_o^2\, Z_2^2\, M^2\, E_R^2}{(M+M_2)^2\, T_m^2} (T_{m/E_d} - 1) \text{ for } E_d \leq T_m \leq 2E_d \qquad \text{B-46}$$

where:

T_m is given by B-45 or:

$$\sigma_d = \frac{8\pi\, a_o^2\, Z_2^2\, E_R^2}{M_2 C^2 E_d} \text{ for } T_m \gg E_d. \qquad \text{B-47}$$

B.2.3.3 Neutrons

B.2.3.3.1 Low Energies-Thermal Through Fission. In this energy range, the assumption of elastic collision is to be used, and with the proper integral equation and suitable boundary conditions, it can be shown that:

$$\bar{\nu}(E) + 1 \quad E_d < E < 2E_d \qquad \text{B-48a}$$

$$\bar{\nu}(E) = E/2E_d \quad 2E_d < E < E_i \qquad \text{B-48b}$$

$$\bar{\nu}(E) = G(E)/2E_d \quad E > E_i \qquad \text{B-48c}$$

In these neutron encounters (neglecting nuclear reactions), the actual displacements are assumed to be caused by elastic collisions of the neutron which has no charge.

The commonly accepted practice in determing the displacement cross section analytically is to assume that the neutrons are scattered isotropically* in elastic collisions are with the nucleus. In these collisions all energy transfers are equally probable and it can be shown

* Actually at higher energies, forward scattering becomes extremely important.

that: $d\sigma = \frac{\sigma_s}{T_m} dt$ B-49

or: $\sigma_d = \frac{\sigma_s}{T_m} (T_m - E_d) \cong \sigma_s$ B-50

assuming is not a function of energy. Actually this assumption is not too bad at higher energies, because, as Billington points out, 2 barns $\leq \sigma_s \leq$ 4 barns for 0.5 Mev $\leq E \leq$ 10 Mev. At energies lower than fission though, $\sigma_s = f(E)$. At present, this report will not be concerned with neutrons of energies higher than fission from a theoretical standpoint, because, here again, the theory is lacking, and very little experimental work has been accomplished.

B.2.4 Displacement Calculations - High Energy. As mentioned before, the high energy range ($E > 100$ Mev) is the most troublesome in displacement calculations because the theory is incomplete. Be that as it may, a brief presentation will now be made on existing theories in high energy reactions.

Most of the present sources employ the following two-step process in their calculations. The incoming high energy particle inelastically strikes the target nucleus causing nucleon excitation*. The parent particle continues on with a reduced energy causing continued nucleon excitation and cascade reactions, until it reaches a much lower energy and comes to rest in a nucleus. The excited nucleons however, are evaporated from the excited nucleus. Generally speaking, protons and neutrons are evaporated from the nucleus, although heavier fragments are possible. As Denny and Pomeroy point out, the energy of the evaporated particles is in the range of 5 to 20 Mev, which is, of course, the range most urgently stressed in radiation damage calculations. Metropolis et al have documented typical cross sections for high energy pion production. But rather than go into the actual mechanics of high energy nuclear reactions ($E > 100$ Mev), a magic number to use at this stage of the calculations would be 1 to 45 times the radiation damage occurring at lower energies (1-20 Mev). Denny

* Pion production (i.e., π^-, π°, π^+) is the major reaction for E greater than approximately 400 Mev.

and Pomeroy performed a calculation based on the experimental results of Smoluchowski on ionic crystals. This calculation formed the basis for this 1 to 5 figure.

B.3 APPLICATION OF DISPLACEMENT THEORY

B.3.1 Particle Spectra. This section is devoted entirely to the calculation of displacements in predetermined materials after traveling directly through the center of the inner Van Allen Belt, through the outer belt and finally to a parking orbit at some distance beyond the outer belt. It will be assumed that the vehicle will be in full view of the sun during each solar flare so that the worst possible case of radiation damage can be estimated. It will also be assumed that the vehicle will be in orbit for one complete year.

The following spectra of Naugle of Kniffen will be assumed.

Inner Van Allen Belt:

$$N(E) = \frac{85 \pm 4 \times 10^6}{E^{4.5 \pm 0.2}} \quad \text{protons/cm}^2\text{-Sec-Mev} \quad 10 \leq E \leq 40 \text{ Mev} \qquad \text{B-51}$$

and

$$N(E) = \frac{12 \pm 6 \times 10^3}{E^{1.7 \pm 0.3}} \quad \frac{\text{protons}}{\text{cm}^3}\text{-Sec-Mev} \quad \text{for } 40 \text{ Mev} \leq E \leq 100 \text{ Mev} \qquad \text{B-52}$$

For the present effort, the damage due to electrons will be neglected since they compose only a small amount* of the total radiation received** on a trajectory of this nature. In addition to the inner belt radiation, the 10 May 1959 solar flare spectra will be assumed since it was the largest 3+ flare reported during this solar cycle. This flare was of class 3+ with maximum particle energy of approximately 1 Bev. The associated integral energy spectra on May 12

* The small amount referred to here is in regard to total radiation including solar flare protons.

** With only the shielding of the vehicle skin (2 grams/cm^2), the ratio of total accumulated dose of electrons to protons on a lunar ascent trajectory was computed to be 27 percent.

(not the peak) was:

$$N(>E) = 3.16 \times 10^{10} E^{-3.6} \qquad \text{B-53}$$

for 110 Mev $<E<$ 220 Mev

Although the energy range is definitely limited as far as the calculations in this report are concerned, Anderson, et al, report on a private communication from Rothwell that the spectrum of the Class 3, 22 August 1958 flare could be extrapolated down to 30 Mev. Due to the nature of the calculations, an extrapolation must be made down to 1 Mev for the 10 May 1959, Class 3+ flare*. Actually the flare spectra would not be as steep as $E^{-4.6}$, but rather E^{-2} or E^{-3} in the range of 1 to 20 Mev. Therefore, the flare spectrum becomes:

$$N(E)\,dE = 1.14 \times 10^{11} E^{-4.6}\,dE \qquad \text{B-54}$$

for 1 Mev $\leq E \leq$ 220 Mev

With these established spectra, material damage will now be examined.

B.3.2 Material Damage. The purpose of this report is to examine the following materials for radiation damage:

a. Mica
b. Teflon
c. Mylar
d. Polystyrene
e. Tantalum
f. Carbon
g. Nickel
h. Ceramic
i. Silicon
j. Silicone Fluids
k. Germanium
l. Mineral Oil and Wax
m. Glass (Kovar and Compression)
n. Phenolic (Mineral Filled)

B.3.2.1 Silicon - Sample Calculation. In the following calculations, all displacement cross sections will be assumed to be in the Rutherford range for simplicity. Therefore:

$$\sigma d = \frac{16\pi a_o^2 Z_1^2 M_1^2 E_R^2}{(M_1 + M_2)^2 E_d T_m} \qquad \text{B-55}$$

* Robey used 23 Mev as the lower limit on the basis of calculations by Anderson and co-workers. These calculations extended the spectrum down to 23 Mev so that cosmic noise absorption could be completely accounted for by flare protons.

but

$$T_m = \frac{4M_1M_2}{(M_1+M_2)^2} \qquad \text{B-56}$$

therefore

$$\sigma_d = 50.24(5.29\text{x}10^{-9})^2(1^2)(14^2M_1^2)(13.6 \times 10^{-6})^2$$

Finally for silicon:

$$\sigma_d = \frac{1.81 \times 10^{-20}}{E} \quad (E \text{ in Mev}) \qquad \text{B-57}$$

or in general

$$\sigma_d = 26 \times 10^{-22} \left(\frac{Z^2}{E_m}\right) \qquad \text{B-58}$$

for a substance of atomic weight M and being bombarded with protons of energy E Mev.

Since the bombarding particle is charged and the primary knock-ons are created in Rutherford collisions, then $\bar{\nu}$, for $T_m > 2E_d$, is:

$$\bar{\nu} = \tfrac{1}{2}\left(\frac{T_m}{T_m - E_d}\right) \left[1 + \ln \frac{T_m}{2E_d}\right] \qquad \text{B-59}$$

and for silicon

$$T_m = \frac{4M_1M_2}{(M_1+M_2)^2} = 0.133\ E \text{ and } E_d = 25 \text{ ev.} \qquad \text{B-60}$$

$$\bar{\nu} = \tfrac{1}{2}\ 1 + \ln \frac{0.133E}{2 \times 25 \times 10^{-6}} \qquad \bar{\nu} = 0.5 + \frac{7.9}{2} + \tfrac{1}{2} \ln E$$

$$\bar{\nu} = \tfrac{1}{2}\ 1 + \ln \frac{133E \times 10^{-3}}{50 \times 10^{-6}} \qquad \bar{\nu} = 4.4 + \tfrac{1}{2} \ln E$$

where E is in Mev. Using equations B-51, B-52, B-57 and B-60 of this section the following calculation is made for the number of displacements produced by Van Allen Belt protons.

$$N_d = N_o \int_{40}^{100} \left(\frac{1.8 \times 10^4}{E^2}\right) \left(\frac{1.81 \times 10^{-20}}{E}\right) \left[4.4 + \tfrac{1}{2} \ln E\right] dE$$

$$+ N_o \int_{10}^{40} \left(\frac{89 \times 10^6}{E^{4.7}}\right)\left(\frac{1.81 \times 10^{-20}}{E}\right) \left[4.4 + \tfrac{1}{2} \ln E\right] dE$$

where:

$$N_o = \frac{6.02 \times 10^{23} \text{ Atoms/mol} \times 2.4 \text{ g/cc}}{28 \text{ grams/mol}}$$

$$N_o = 5.15 \times 10^{22} \text{ Atoms/cc}$$

$$N_d = 16.8 \times 10^6 \int_{40}^{100} \left[4.4 + \tfrac{1}{2} \ln E\right] \frac{dE}{E^3}$$

$$+ 8.28 \times 10^{10} \int_{10}^{40} \left[4.4 + \tfrac{1}{2} \ln E\right] \frac{dE}{E^{5.7}}$$

$$\underline{\text{High Energy}} \qquad \underline{\text{Low Energy}}$$

$$N_d = 19{,}500 + 8{,}840 + 15.51 \times 10^5 + 4.4 \times 10^5$$

$$= 2 \times 10^6 \text{ Displacements/cm}^3 - \text{sec}$$

It is immediately obvious that the high energy component, that is from 40 to 100 Mev, is insignificant (~ 1 percent) compared to the low energy component.

Denny and Pomeroy suggest that 50 percent of the Van Allen Belt protons have energies above 100 Mev and that these 50 percent produce from 1 to 5 times as many defects as do the protons with energies below 100 Mev. Therefore, on this basis:

$$\frac{5N_d\big]_{1\text{-}100}}{N(>10) + N(>40)} = \frac{N_d\big]_{100\text{-}700}}{N(>100)} \qquad \text{B-62}$$

The number of protons with energies greater than 10 Mev using the spectra of Naugle and Kniffen is:

$$N(>10) = \int_{100}^{40} 8.9 \times 10^6 \, dE \qquad \text{B-63}$$

$$= 2.405 \times 10^6 \quad 2.00 \times 10^{-4}$$

$$N(>10) = 481 \text{ protons/cm}^2\text{-sec.}$$

$$N(>40) = \int_{40}^{100} \frac{1.8 \times 10^3 dE}{E^2} \qquad \text{B-64a}$$

$$N(>40) = 90 \text{ protons/cm}^2\text{-sec.}$$

Using the Freden and White spectra for protons above 100 Mev, it is found that:

$$N(E) = 8.28 \, f(E) \, e^{-E/170} \text{ protons/cm}^2\text{-sec - Mev} \qquad \text{B-64b}$$

$$100 \leq E \leq 700 \text{ Mev}$$

where: $f(E)$ is a slowly varying function of E. For the purposes of the calculation, assume $f(E) = 1$,
which will overestimate N(E).
Therefore:

$$N(>100) = 8.28 \int_{100}^{700} e = {}^{-E/170}{}_{dE}$$

$$N(>100) = 756 \text{ protons/cm}^2\text{-sec} \qquad \text{B-65}$$

With these integrated fluxes then, the number of displacements in silicon due to the high energy protons alone is:

$$N_d = \frac{5 \times 2 \times 10^6 \times 756}{90 + 481}$$

$$N_d = 1.32 \times 10^7 \text{ Displacements/cc/sec} \qquad \text{B-66}$$

The remaining problem is to determine the amount of time the vehicle will be exposed to these proton fluxes during the ascent part of the flight. An IBM 650 code has been developed which determines the radiation dose level, total accumulated dose, elapsed time and altitude while traversing the Van Allen Belts. This code used the proton spectra of Freden and White, the electron spectra of Walt, and an assumed vehicle skin thickness of 2.0 grams/cm^2. One test case was run using this code so that the total elapsed time could be anticipated. The author prefers to use the newer spectra of Naugle and Kniffen. However, the elapsed time of the test case trajectory will be used to calculate the total number of displacements/cm^3. The total time for traversal of the belt according to these results is 1366 seconds (25 counts/second is assumed for the ambient count level). Therefore, the total number of displacements/cm^2 produced during the ascent portion of the flight for just the Van Allen belt protons* is:

$$(N_d)_{vap} = 2.08 \times 10^{10} \text{ Displacements/cc} \qquad \text{B-67}$$

* This figure appears to be in conflict with Denny and Pomeroy calculation. However, the time of stay in the belt is the deciding factor in the number of displacements. The flight takes 10^3 seconds which gives rise to 10^{10} displacements and Denny and Pomeroy indicate a stay of a 10^7 sec gives rise to 10^{14} displacements. With this in mind then, the calculations are certainly compatible.

CONFIDENTIAL

The remaining problem is to estimate the number of displacements produced by a solar flare. The 10 May 1959 flare differential proton spectra given by B-54 is very pessimistic (probably the wrost possible case), in view of the fact that an intense low energy component was assumed. However, since the results of the calculations presented in this report are to be pessimistic and in view of the scarce literature on the subject of displacement calculations for these energies, this spectra will be assumed. According to Denny and Pomeroy, the majority of the displacements in solids occur due to incident protons in the 1 to 20 Mev range, and roughly 1 to 5 times as many defects (in NaCl and KCl) are produced by protons with energies above 100 Mev then in the 1 to 20 Mev range. The assumption which will be made here is the following:

$$\frac{(5N_d)_{1\text{-}20\ \text{Mev}}}{N(>1)} = \frac{(N_d)_{E>100\ \text{Mev}}}{N(>100)} \qquad \text{B-68}$$

This simply says that five times the number of displacements per unit integrated flux at low energy is the same as the number of displacements per unit integrated flux at high energies. This fact is approximately true for NaCl and KCl. Very lengthy calculations are required to obtain this multiplication factor for other elements and will not be attempted at this point. On this basis, the following calculations are made:

Assuming the spectra given by B-54 the total number of protons with energies above 1 Mev is:

$$N(>1) = 1.14 \times 10^{11} \int_1^{100} E^{-4.6} dE$$

$$= 3.166 \times 10^{10}\ \text{protons/cm}^2\text{-sec}$$

$$= 1.397 \times 10^{13}\ \text{protons/cm}^2\text{-hr}$$

According to Robey, the total extent of the flare was 29.5 hours and the flux decayed with a rate of $e^{-0.575t}$. Follwoing Robey then, the total proton flux received over the duration of the flare is:

$$N(>1) = 1.397 \times 10^{13} \int_0^{\infty} e^{-0.575t}\, dt + 1.397 \times 10^{13} \times 29.5$$

$$N(>1) = 4.35 \times 10^{14}\ \text{protons/cm}^2 \qquad \text{B-69}$$

CONFIDENTIAL

This figure may be compared to $N\ (>23) = 4.49 \times 10^{10}$ protons/cm^2. In other words, the assumed intense low energy component magnifies the approximately correct $N(>23)$ by 10^4 fold.

The number of protons with energies greater than 100 Mev is:

$$N(>100) = 1.14 \times 10^{11} \int_{100}^{200} E^{-4.6}\, dE$$

$$= 1.397 \times 10^{13}\ 6.3 \times 10^{-8}$$

$$= 8.80 \times 10^5 \text{ protons/cm}^2\text{-hr}$$

The total flux received over the duration of the flare is then:

$$N(>100) = 8.80 \times 10^5 \int_0^{\infty} e^{-0.575t} dt + 8.80 \times 10^5 \times 29.5$$

$$N(>100) = 15.30 \times 10^5 + 259.6 \times 10^5$$

$$N(>100) = 2.649 \times 10^6 \text{ protons/cm}^2 \qquad \text{B-70}$$

In view of this result and in view of the fact that the estimate given by B-69 could conceivably be off by a magnitude 4 if the low energy component is neglected altogether, it may be concluded that;

$$\frac{(5N_d)_{1\text{-}20} \times N(>100)}{N(>1)} \sim 0 \qquad \text{B-71}$$

in comparison with the original number of displacements. This simplification lightens the burden of calculation considerably. Using the equations for silicon which were developed for Van Allen Belt protons.

$$\sigma_d = \frac{1.81 \times 10^{-20}}{E}$$

$$\bar{\nu} = 4.4 + \tfrac{1}{2} \ln E$$

$$N_o = 5.15 \times 10^{22} \text{ atoms/cc}$$

$$\phi = 1.14 \times 10^{11} E^{-4.6} \qquad \text{B-72}$$

therefore:

$$N_d = \int_1^{100} \phi\, n_o\, \bar{\nu}\, \sigma_d dE$$

or $N_d = 3.74 \times 10^{17}$ displacements/cm^2-hr.

The total number of displacements, as before, is calculated as follows:

$$N_d = 3.74 \times 10^{17} \int_0^{\infty} e^{-0.575t} dt + 3.74 \times 10^{14} \times 29.5 \qquad \text{B-73}$$

$$N_d = 1.16 \times 10^{19} \text{ displacements/cc.}$$

The last point on the curve of P_{max} versus flux of the Loferski-Rappaport data using 17.6 Mev protons is approximately 3×10^{11} protons/cm^2 with a 60 percent reduction in solar cell output power. This corresponds to:

$$N_d = 3 \times 10^{11} \times 5.15 \times 10^{22} \times \frac{1.80 \times 10^{-20}}{17.6} \times (4.4 + \tfrac{1}{2} \ln 17.6)$$

$$N_c = 9.16 \times 10^{13} \text{ displacements/cm}^3. \qquad \text{B-74}$$

In view of the number of displacements calculated, it may be concluded that silicon solar cells would become inoperable after being irradiated by this flux.

It is interesting at this point to compare threshold values of silicon transistors to the previously computed solar cell damage due to the solar flare. If it is assumed that the meaning of threshold is that value of flux at which the device becomes incompatible with established specifications, that is, operates beyond a given range of values, then the following calculation is valid. Mitchell indicates a threshold value of the next section it is shown that $\overline{\nu}$=900 for fast neutrons;

$$N_d = 10^{12} \text{ neutrons/cm}^2 \times 5.15 \times 10^{22} \text{ atoms/cc} \times 10^{-23} \text{ cm}^2\text{/atom} \times 900 \text{ d/neutrons}$$

$$N_d = 5 \times 10^{14} \text{ displacements/cc}$$

If this N_d is off by a conservative factor of 5, which some investigators claim, and the calculation on silicon solar cells is a factor of 2 conservative (which is certainly likely), the conclusion is reached that both thresholds are about the same, and both types of units will become inoperable when subjected to these fluxes.

B.3.2.2 Carbon - Sample Calculation. Most of the existing data on carbon has been in terms of damage due to neutron fluxes. For the present effort, fast neutron damage data will be used.

$\sigma_d \cong \sigma_s$ which is pessimistically $1 \leq \sigma_s \leq 10$ barns for fission energies instead of $2 \leq \sigma_s \leq 4$ barns as pointed out

* That is neutrons in the Mev range.

previously. The energy averaged mean number of displaced atoms per primary knock-on $\overline{\nu}$ (E) for neutrons is:

$$\overline{\nu}(E) = \frac{\overline{G}(E)}{2E_d} \qquad \text{B-75}$$

$\overline{G}$ (E) for carbon is, according to Dienes and Vineyard

$\overline{G}$ (E) = 45,000 ev hence

$\overline{\nu}$ (E) = 900.

The atom density for carbon (crystals) is:

$N_o = 1.76 \times 10^{22}$ atoms/cc

Mitchell indicates that the nuclear radiation damage threshold for carbon resistors is of the order of 10^{15} fast neutrons/cm^2.

Therefore:

$N_d = 10^{15} \times 10^{-23} \times 900 \times 1.76 \times 10^{22}$

$N_d = 1.6 \times 10^{17}$ displacements/cc produced by fission neutrons.

Further substantiation of this result can be obtained from Chapin's work as follows:

Chapin, based on Admiral's results, indicates that peak change in resistance of -7 percent for a 1 megohm, non-energized carbon resistor, occurs at an irradiation time of 40×10^4 seconds. The flux in the reactor was 2.3×10^9 fast neutrons/cm^2-sec and 3.9×10^4 ergs/g-sec. Assuming the gamma flux negligible,

$N_d = 1.5 \times 10^{17}$ displacements/cc.

Lower value resistors in similar tests indicate even less damage, that is the other extreme was an 100 ohm resistor which peaked out at -2 percent. Prolonged irradiation tended to partially anneal incurred damage: For example, the one megohm resistor tailed off to -5 percent after 180×10^4 seconds with a gentle slope from the peak. Although Chapin does not say, the resistors are probably $\pm$ 5 percent resistors (carbon-epoxy type).

The number of displacements which will occur during the solar flare can be computed as follows:

$$N_d = 1.766 \times 10^{23} \int_1^{100} \frac{1.14 \times 10^{11}}{E^{4.6}} \cdot \frac{7.8 \times 10^{21}}{E} (4.322 + \tfrac{1}{2} \ln E)\, dE$$

$N_d = 6.058 \times 10^{17}$ d/cc/hr.

Preceeding as before then: $\int_o^\infty e^{-0.575t} dt + 6.058 \times 10^{17} \times 29.5$

(N_d) total = 6.05×10^{17}

(N_d) total = 1.392×10^{13} d/cc.

On the basis of the previous calculation regarding threshold damage, it may be concluded that (assuming pure carbon) carbon resistors will be damaged after being subjected to these fluxes.

The results of the remainder of the calculations on elements are summarized in Table B-1.

Table B-1 Summary of Radiation Damage Calculations

MATERIAL	VAN ALLEN BELT (LOW)	VAB (HIGH)	SOLAR FLARE	DAMAGE THRESHOLD	REMARKS
Nickel $n_o = 9.22 \times 10^{22}$ $\sigma_d = \frac{3.472 \times 10^{-20}}{E \text{ (Mev)}}$ $\bar{\nu} = 4.089 + \frac{1}{2} \ln E$ $T_m = 0.0658E$ (Mev)	8.96×10^9 d/cc	4.458×10^{10} d/cc	3.750×10^{19} d/cc	3.1×10^{22} d/cc See Remarks	This threshold value is not threshold per sec; radiation damage was caused by $\emptyset = 1.1 \times 10^{17}$ d/cm^2 (12 Mev deuterons) at temperatures between 140°K to 121°K. This integrated dose resulted in anomalous changes in resistivity
Silicon $n_o = 5.15 \times 10^{22}$ $\sigma_d = \frac{1.81 \times 10^{-20}}{E}$ $\bar{\nu} = 4.4 + \frac{1}{2} \ln E$ $T_m = 0.133 E$	2.73×10^9 d/cc	1.366×10^{10} d/cc	1.171×10^{19} d/cc	$\sim 5 \times 10^{14}$ d/cc σ_s=10 barns $\bar{\nu}$ = 900 $\emptyset t = 10^{12}$ n/cm^2	
Germanium $n_o = 4.52 \times 10^{22}$ $\sigma_d = \frac{3.66 \times 10^{-20}}{E}$ $\bar{\nu} = 3.980 + \frac{1}{2} \ln E$ $T_m = 0.0536 E$	4.535×10^9 d/cc	2.268×10^{10} d/cc	1.86×10^{19} d/cc	$\sim = 4 \times 10^{15}$ d/cc σ_s=10 barns $\bar{\nu}$ =900 $\emptyset t = 10^{13}$ n/cm^2	

Table B-1 Summary of Radiation Damage Calculations (Continued)

MATERIAL	VAN ALLEN BELT (LOW)	VAB (HIGH)	SOLAR FLARE	DAMAGE THRESHOLD	REMARKS
Tantalum $n_o = 5.52 \times 10^{22}$ $T_m = 0.022\ E$ $\sigma_d = \frac{7.657 \times 10^{-16}}{E}$ $\bar{\nu} = 3.543 + \frac{1}{2} \ln E$	1.062×10^{12} d/cc	5.310×10^{12}	4.305×10^{21}	$\sim = 5 \times 10^{17}$ d/cc $\sigma_s = 10$ barns $\bar{\nu} = 900$ $\phi t = 10^{15}$ n/cm^2	Calculated on worst possible case basis
Carbon $n_o = 1.766 \times 10^{22}$ $T_m = 0.284\ E$ $\sigma_d = \frac{7.8 \times 10^{-21}}{E}$ $\bar{\nu} = 4.822 + \frac{1}{2} \ln E$	4.475×10^{3} d/cc	2.238×10^{10} d/cc	1.892×10^{19} d/cc	$\sim 10^{17}$ d/cc $\sigma_s = 10$ barns $\bar{\nu} = 900$ $\phi t = 10$ n/cm^2	

B.4 DISCUSSION AND CONCLUSIONS. One point which has been intentionally overlooked in this effort is the atomic displacements in materials which are contained in shielded vehicles. The vehicle skin will provide a certain amount of shielding and other specifications may require even more. Moderate shielding will screen out the low energy protons which are effective in producing displacements. However, there is a distinct possibility that secondary neutron generation by the remaining protons will constitute a radiation damage hazard equal to the original unshielded proton flux. Preliminary estimates on biological doses delivered by the 10 May 1959 flare indicated severe problems regarding secondary neutron flux. The secondary neutrons could possibly magnify the radiation damage problem since neutrons are more effective in producing displacements than protons by as much as a factor of 100 or more.

In addition to the low energy component, the reader will recall that the high energy particles were neglected in this report since the flux was orders of magnitude lower than the important low energy flux. It is conceivable that with shielding, the high energy particles could produce secondaries which would significantly effect radiation damage calculations.

With reference to the Van Allen Belt, a trajectory was chosen so that the vehicle would travel directly through the heart of the inner Van Allen Belt; however, the stay-time was low (1,366 seconds total). In the event that a vehicle is to stay longer than 10^6 to 10^7 seconds, new radiation damage calculations will have to be made to insure reliable component functioning.

The last item to be discussed before presenting the conclusions is the problem of radiation damage in compounds. Due to time limitations, no consideration was given to radiation damage in compounds. In the preliminary literature search on this effort, ample evidence was found which indicated the mechanism of radiation damage in compounds is well documented. Two separate areas are envisioned at this time and they are diatomic solids and organic materials (due to the difference in bonding mechanisms).

B.4.1 Radiation Damage. The following conclusions have been reached as a result of the study*.

a. Silicon devices such as solar cells and transistors may become inoperable during and after the flare.

b. Germanium transistors may become inoperable during and after the flare.

c. Tantalum capacitors may become inoperable during and after the flare.

d. Carbon resistors may become inoperable during and after the flare.

e. Materials of nickel will not be significantly affected during or after the flare.

f. Any attempt at shielding (with the exception of liquid hydrogen), will give rise to secondaries which are potentially more lethal than the original protons.

g. High energy reactions may play an important part in total radiation damage when shielding is provided.

h. The total radiation damage is very sensitive to time of exposure and therefore to trajectory.

i. Crude estimates indicate a radiation damage to the diatomic solids and certain hydrocarbons. The estimates are close enough to the damage threshold to warrant further study.

j. The transient behavior of some materials is presently being given considerable attention in the literature and will certainly warrant consideration.

k. Throughout the report homogeneous production of displacements was assumed with no annealing. Refinements such as displacement spikes and annealing should be taken into consideration in the final analysis.

* The radiation damage listed here is based on the flare of 10 May 1959 with the assumption of no shielding on irradiated materials.

APPENDIX C
TRANSPORTATION ROUTE SURVEY

C.1 SUMMARY. It was determined, from the limiting factors and existing conditions of the route surveyed, that a combination transporter and load, 36 feet in diameter and 120 feet in length, can travel from San Diego, California to Mercury, Nevada. A trailer transporter with a maximum wheel base length of 80 feet and steerable rear wheels can negotiate the curves and intersections encountered.

It is economical and physically feasible to use the route surveyed since the route will not require extensive and costly modification such as complete rebuilding of roads, bridges, etc. However, the route will require adequate modification needed for a transporter and load of the size indicated above. This modification will involve removal of obstructions such as various road signs, signal lights, railroad crossing signals, street lights, telephone poles, etc. Numerous trees will have to be trimmed. Wires of all types (telephone cables, high tension power lines, etc.) will have to be raised or removed to permit passage. Arrangements for removal of the obstructions, wires, etc. will be made with the cities, townships and personnel involved well in advance of the actual trip.

A mockup of the object to be transported (on the carrier designed for transport) will travel the route prior to the actual transport of the object. This mockup will be designed and used for the advance trip to determine and detail the obstructions, wires, etc. to be removed. The mockup can be made of plywood (hinged at critical points) and constructed in such a way that all critical points of clearance can be checked. A road construction crew should precede the actual transportation of the object to prepare the route (fill for dips or humps, grading, planking bridges if necessary, etc.)

The time required to transport the object from San Diego, California

to Mercury, Nevada (a distance of 400 miles) will be approximately five to ten days. Trip-time will be governed by weather conditions, speed at which the road crew can prepare the route, and the speed of the tractor/trailer transport.

A map of the route from San Diego, California to Mercury, Nevada and a more detailed map of the route through Riverside, California and San Bernardino, California is presented in Figures C-1 and C-2. A description of the route is presented in Section C-1.5.

C.1.1 Assumptions. The survey was made on the assumption that the trailer used for transport would be designed with steerable rear wheels to negotiate intersections and curves. Further, the survey was made assuming travel would be accomplished with existing conditions of the route and therefore, no attempt was made to foresee future conditions of the route.

C.1.2 General. The survey was performed to locate the limiting factors that affect transport of the largest possible object (width and length) from San Diego, California to Mercury, Nevada. These limiting factors could be the minimum width of a through-cut, the minimum turn-area of an intersection, the sharpest curve that would be negotiated, etc. The limiting factors were located by a process of elimination of the points of interest investigated, and then were analyzed. The limiting factor which determined the maximum width was a through-cut 30.9 miles from San Diego, California. The limiting factor which determined the maximum length was the intersection of Etiwanda Avenue and Highland Avenue (San Bernardino, California) 103.2 miles from San Diego, California. Other problem areas were noted and are presented in later text. A table of the points of interest investigated is presented in Section C.1.5.

C.1.3 Limiting Factors

C.1.3.1 Through-Cut. The maximum width that can be transported was limited by a through-cut 30.9 miles from San Diego, California, just north of Escondido. This cut, Figure C-3, has high almost-vertical walls of solid rock which measured 38 feet at the most

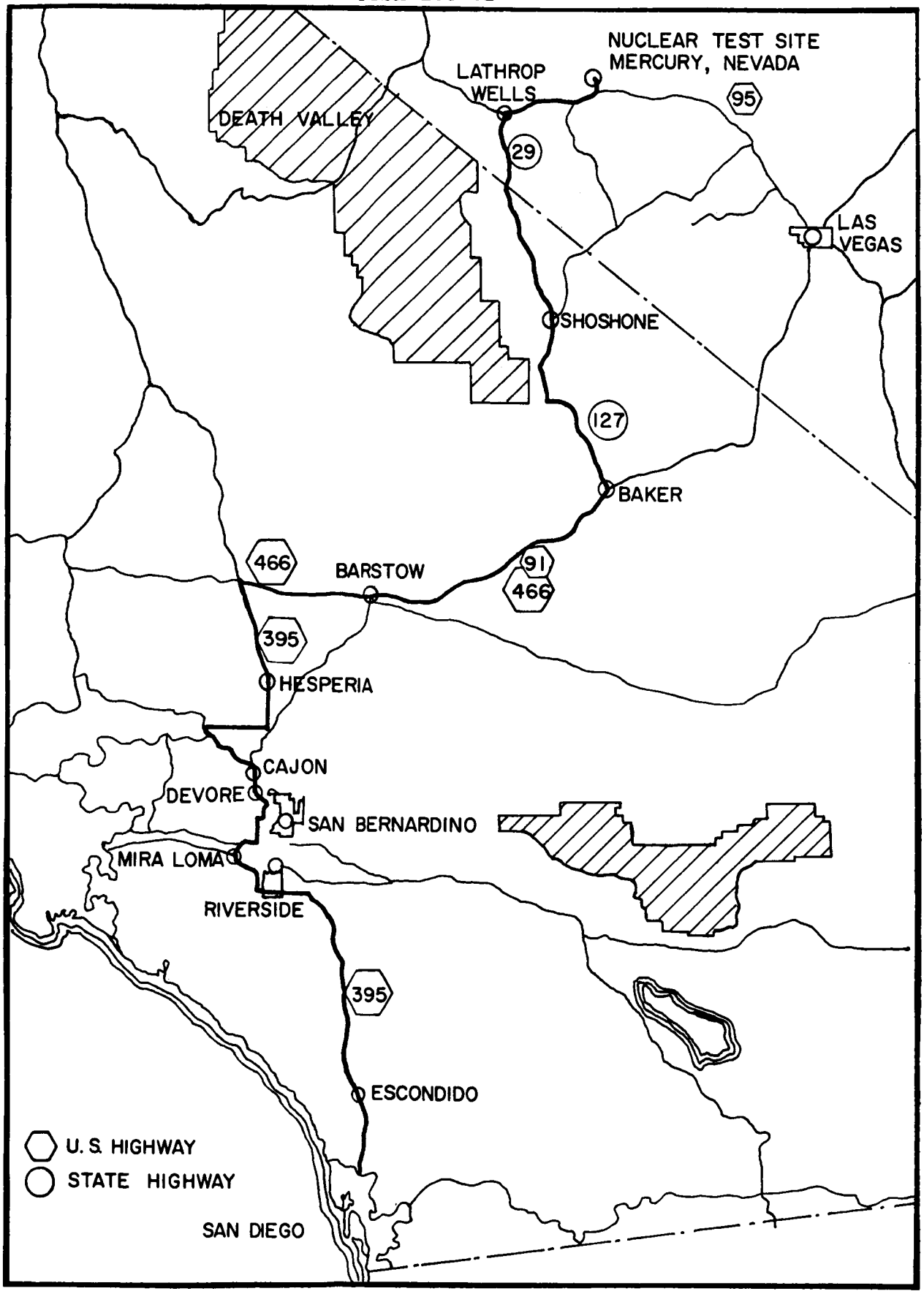

Figure C-1. Route from San Diego, California to Mercury, Nevada.

CONFIDENTIAL

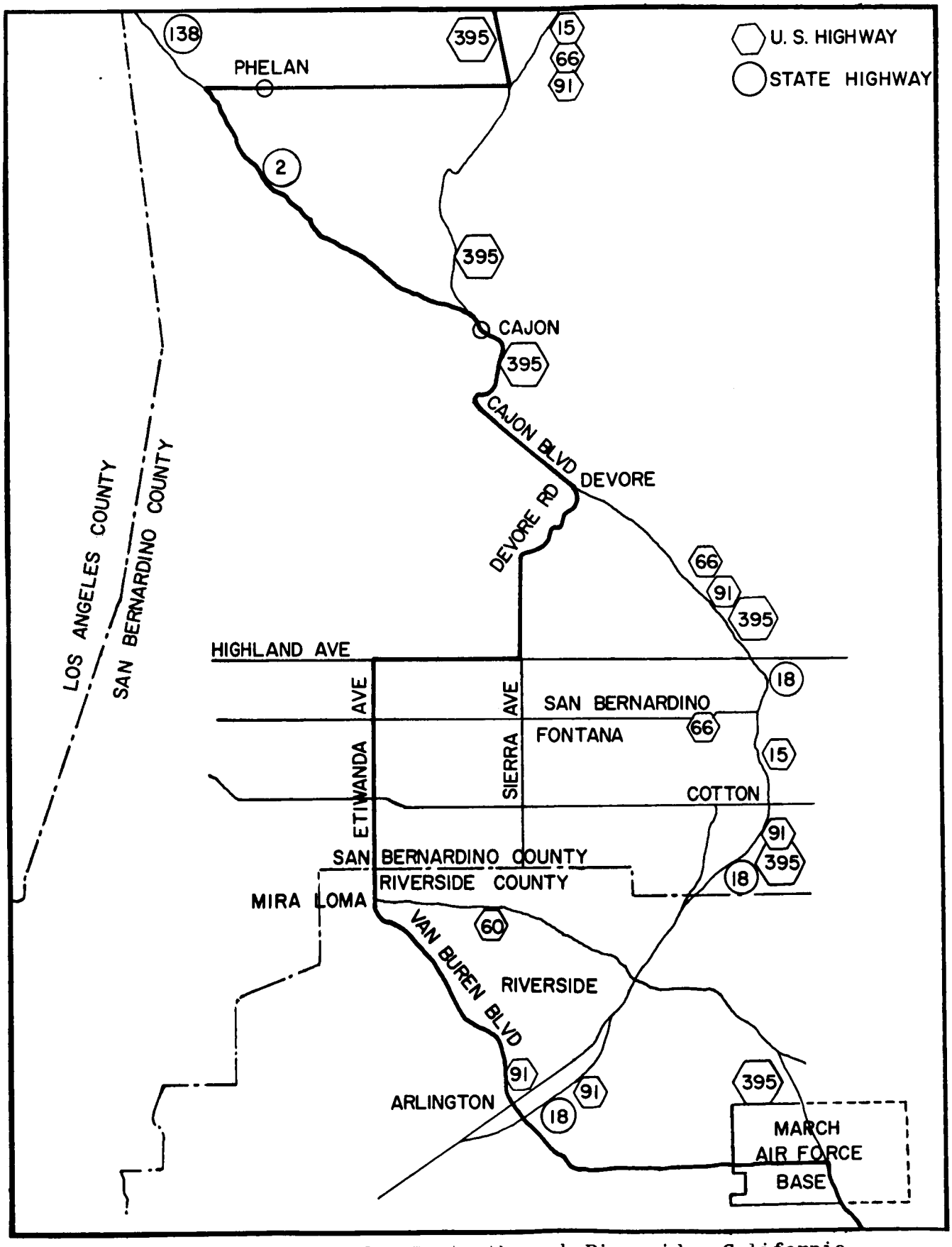

Figure C-2. Route through Riverside, California and San Bernardino, California

CONFIDENTIAL

limiting point. This cut is only 0.2 mile in length and a width of 36 feet could be transported through this cut with little difficulty. It would be possible to widen this cut, however, considerable expense would be involved.

One other through-cut which would present a problem is on Highway 127, 325.3 miles from San Diego, California. This cut, Figure C-4, has a roadbed width of 28 feet and a width of 32 feet from wall to wall (six feet above the road level). The walls of the cut widen at the top to approximately 50 feet. The west wall of the cut is 25 feet high and the east wall is 15 feet high. The east wall consists of crached or fractured malapi rock and clay and can be bladed down with little difficulty at relatively low cost.

C.1.3.2 Intersection. The intersection of Etiwanda and Highland Avenues, north of Mira Loma in San Bernardino, California and 103.2 miles from San Diego, would limit the length of the object that would travel this route. A diagram of the intersection is shown in Figure C-5. Photographs of the intersection are presented in Figures C-6 and C-7. On the southeast corner of the intersection, palm trees (shown in Figure C-6) will have to be removed in order to negotiate the turn. With these trees removed, a much larger turn-area is obtained and the transporting vehicle can travel across the inner-corner which has a good gravel/rock/sand base. This corner would need rock and/or gravel fill to modify it for travel. Also, fill could be used to modify the curb on the east side of Etiwanda Avenue to avoid jumping the curb.

Trees lining both sides of Highland Avenue will have to be trimmed. These trees are only forty-one feet apart (measuring across the road from tree trunk to tree trunk) at their nearest point.

Other intersections investigated were not as limiting as the intersection mentioned above. These intersections, however, would need to be modified slightly by grading, removal of road signs, etc.

CONFIDENTIAL

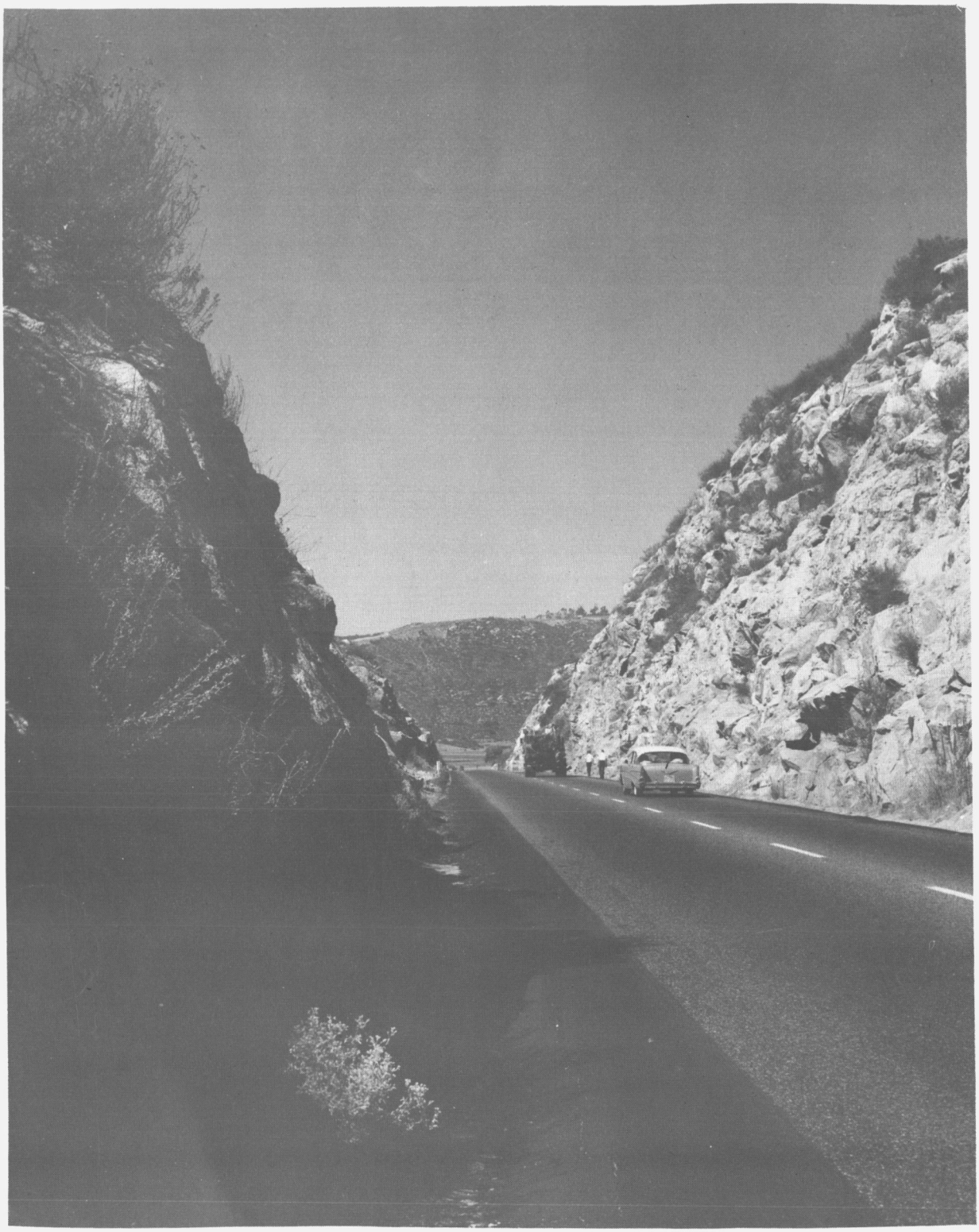

Figure C-3. Limiting Through-cut (looking north), North of Escondido, California U.S. Highway 395

CONFIDENTIAL

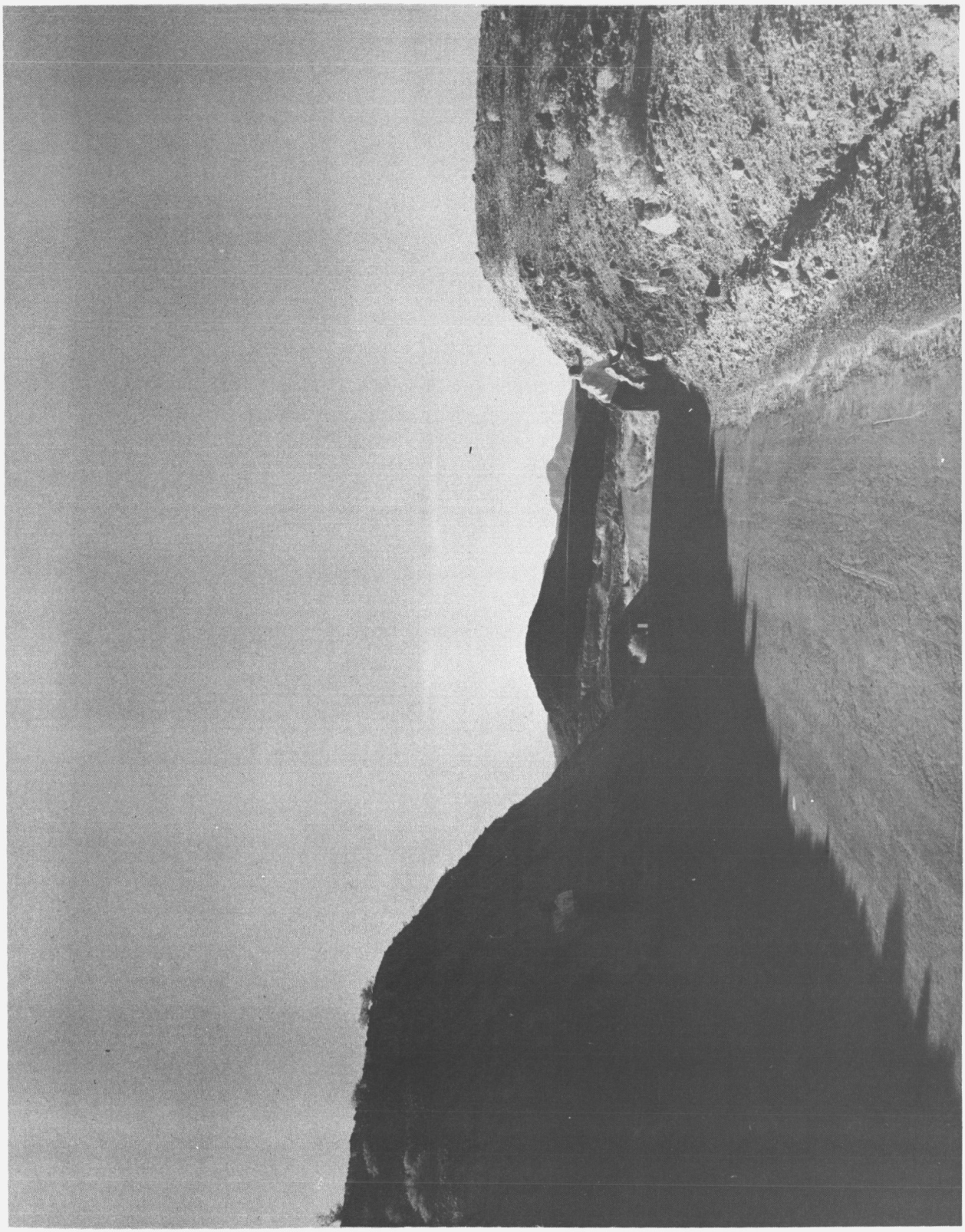

Figure C-4. Through-cut (looking north), North of Shoshone, California

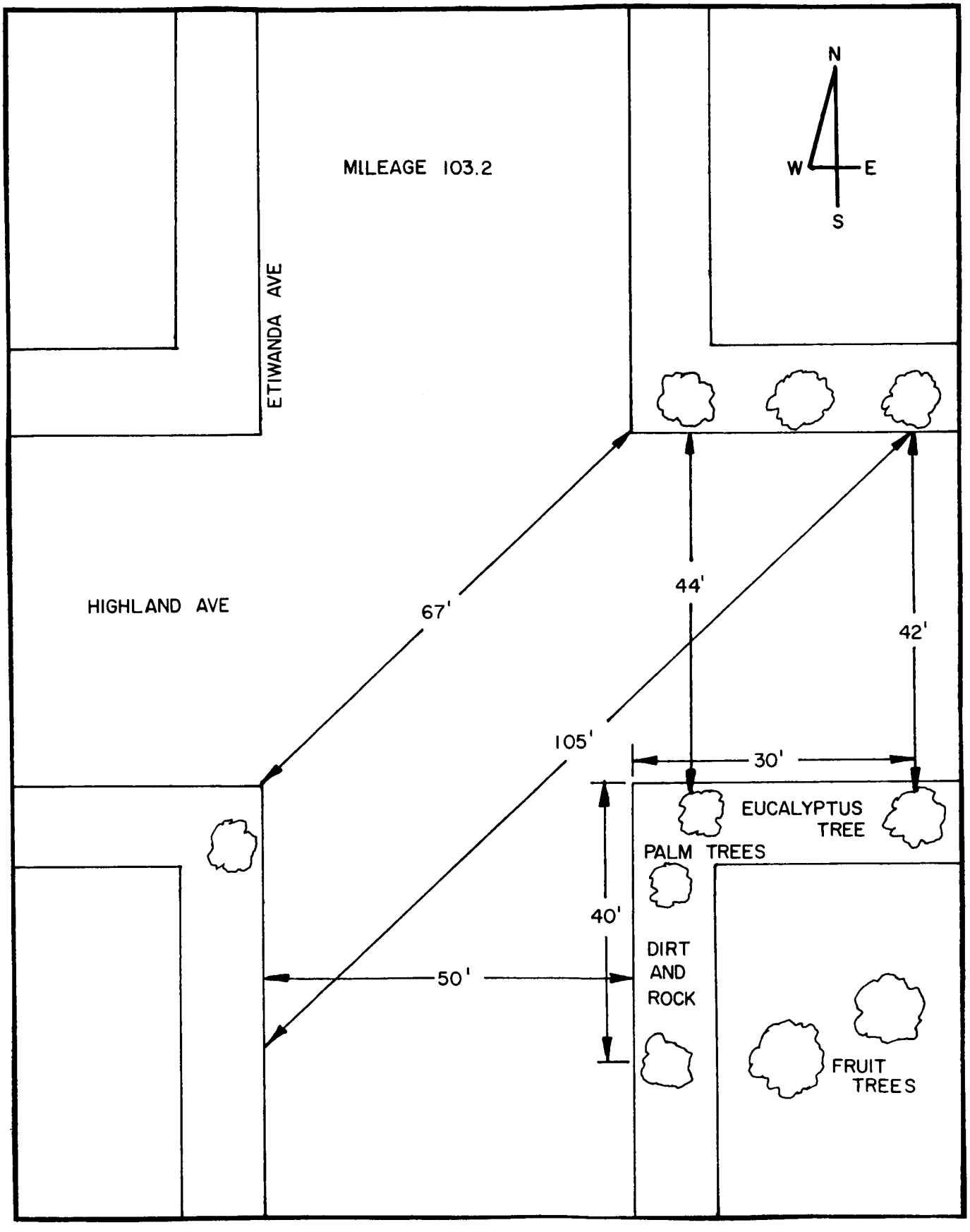

Figure C-5. Limiting Intersection at Etiwanda Avenue and Highland.

Figure C-6. Intersection of Etiwanda Avenue and Highland Avenue (looking southeast) in San Bernardino, California

CONFIDENTIAL

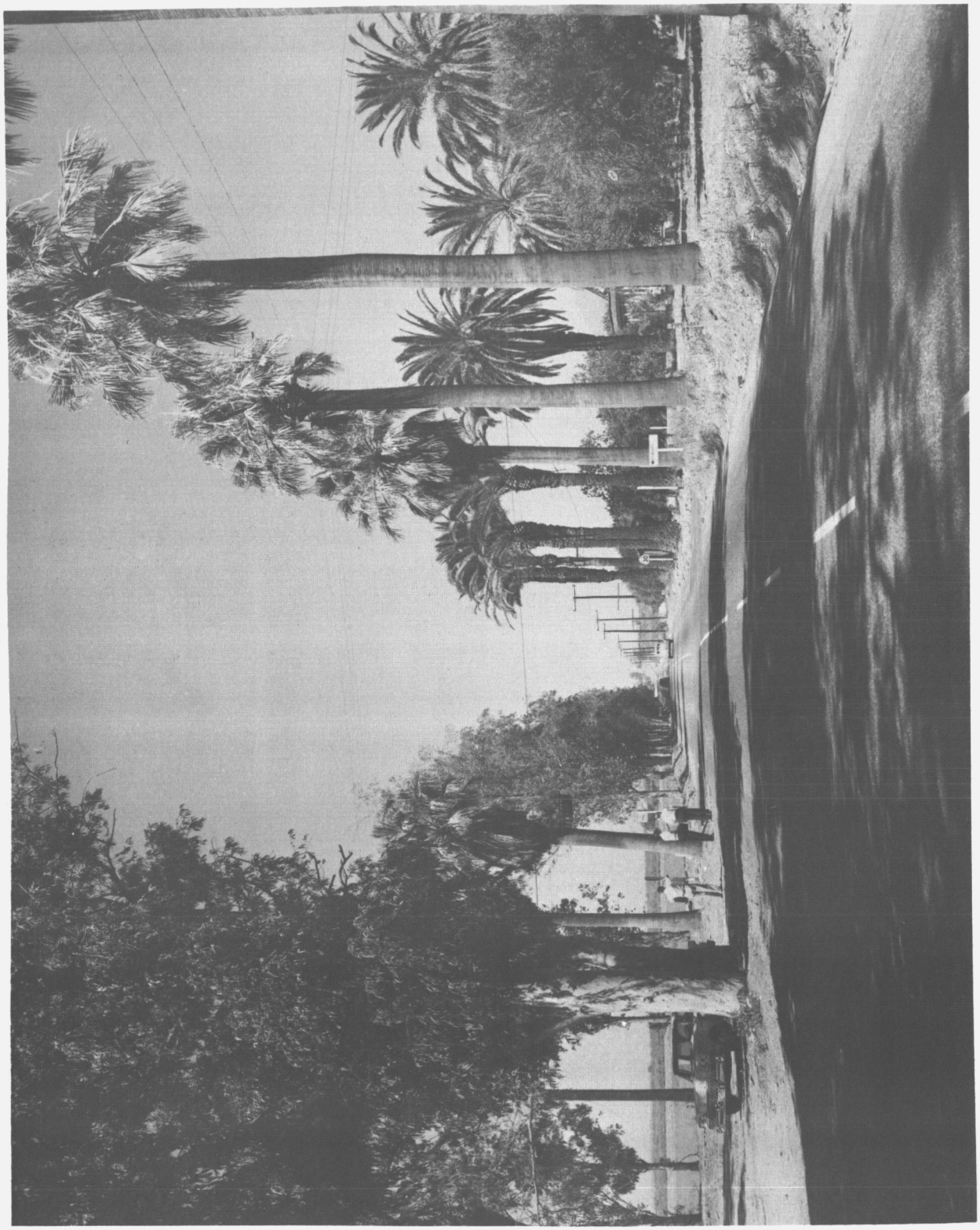

Figure C-7. Intersection of Etiwanda Avenue and Highland Avenue in San Bernardino, California (looking west on Highland Avenue)

CONFIDENTIAL

C.1.4 Problem Areas

C.1.4.1 Overpasses. Due to the height of the object being transported, overpasses are avoided by rerouting when possible. However, on the route surveyed, two overpasses were encountered which could not be avoided nor could the route be revised. The overpass itself presented the solution. These two overpasses are now under construction; one on U.S. Highway 395 at Perris, California and the other on U.S. Highway 91/466, seven miles east of Barstow, California. It will be possible to bypass each overpass by using the up- and down-ramps on the overpass. In each case, the bypass can be effected by entering the up-ramp on the right of the highway, crossing the overhead road on the overpass and proceeding on the down-ramp to the highway. These up- and down-ramps are 24 feet in width from curb to curb and have six-foot shoulders. Figures C-8 and C-9 illustrate the up- and down-ramps of the overpass on U.S. Highway 395. The two overpasses are similar in construction and will provide the same type of bypass.

C.1.4.2 Bridges. Two bridges, of the many encountered, were studied for possible bypass due to poor construction. The bridges, Figure C-10, located 111.6 miles from San Diego on Devore Road in San Bernardino, California, are of wooden construction (2-inch by 12-inch wood members 20 feet in length, supported on the 2-inch side, running length-wise with the road). The width of the bridge is 24 feet (guard rail to guard rail). A bypass of these two bridges can be accomplished by means of a shoe-fly on the southeast side of the road. The shoe-fly is a partially paved road and can be used during dry weather if sufficient fill is brought in to shape-up the road. Three telephone poles to the right of the shoe-fly would have to be set back if this shoe-fly is used. Photographs of this shoe-fly are presented in Figures C-11 and C-12.

Between Barstow, California and Baker, California there are some 46 bridges of wooden construction (6-inch by 15-inch wood members, supporting the bridge on the 6-inch side, spaced 2 feet apart, run

CONFIDENTIAL

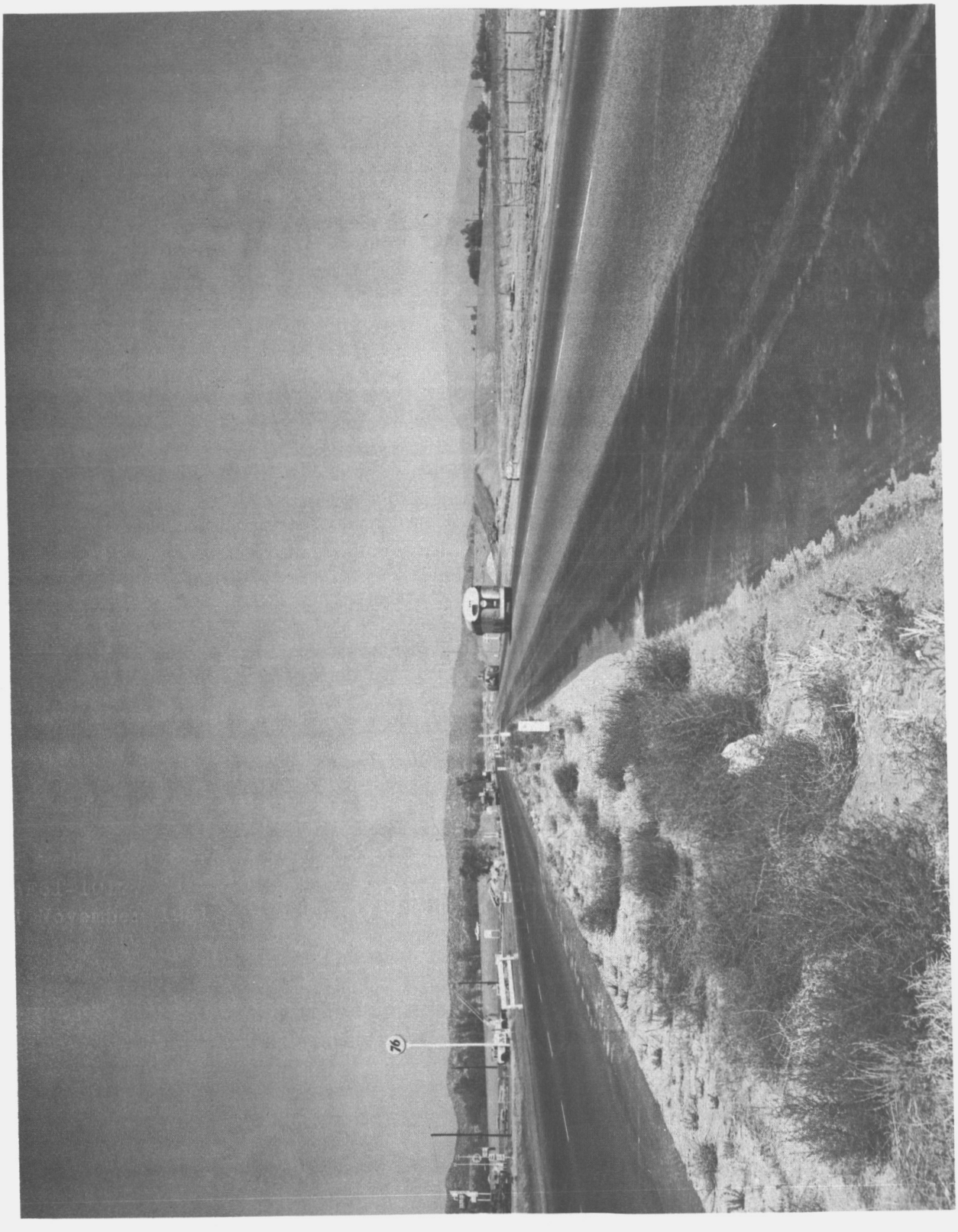

Figure C-8. Construction of Overpass on U. S. Highway 395, Perris, California (looking north)

CONFIDENTIAL

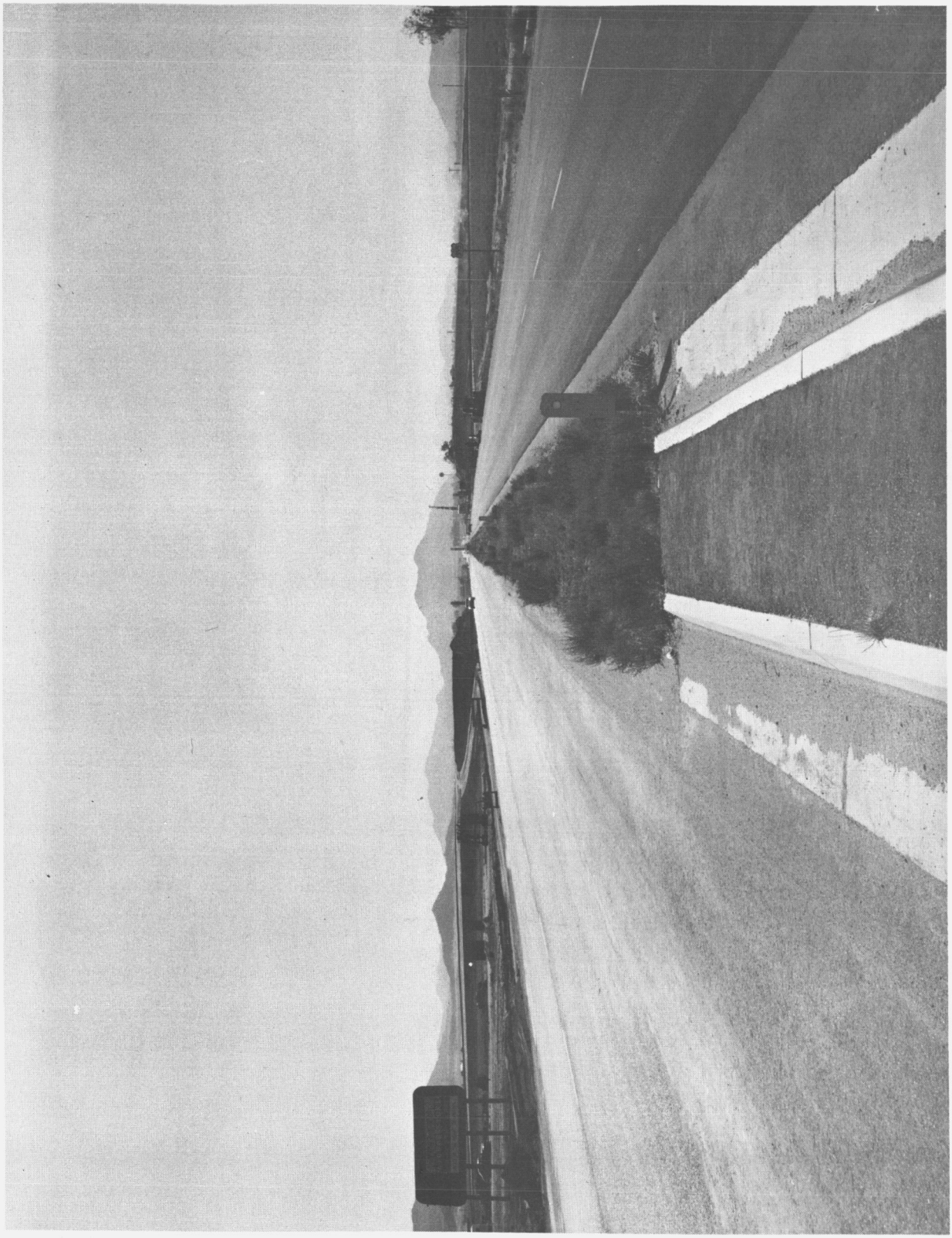

Figure C-9. Construction of Overpass on U. S. Highway 395 (looking south)

CONFIDENTIAL

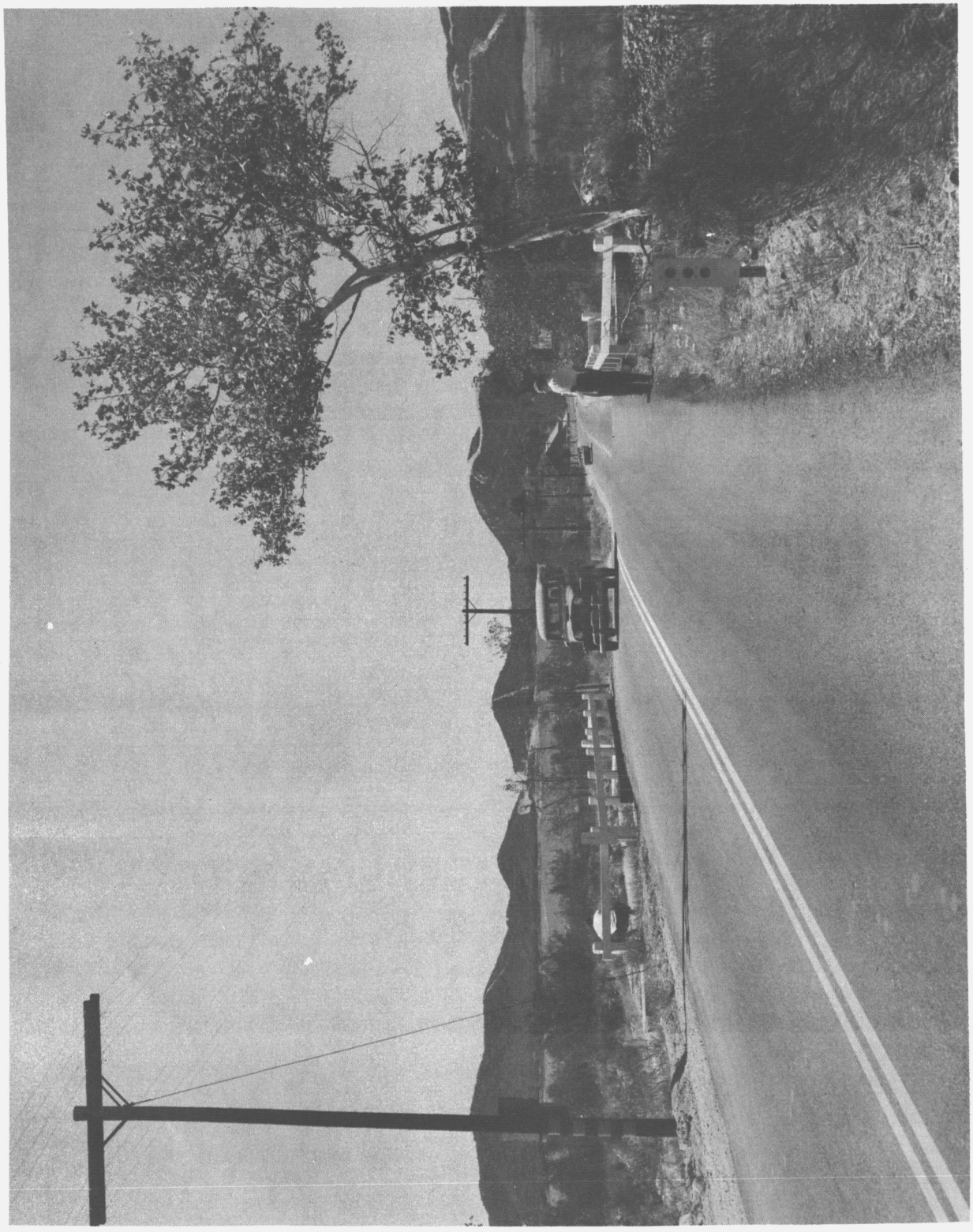

Figure C-10. Bridge on Devore Road, San Bernardino, California (looking southeast)

CONFIDENTIAL

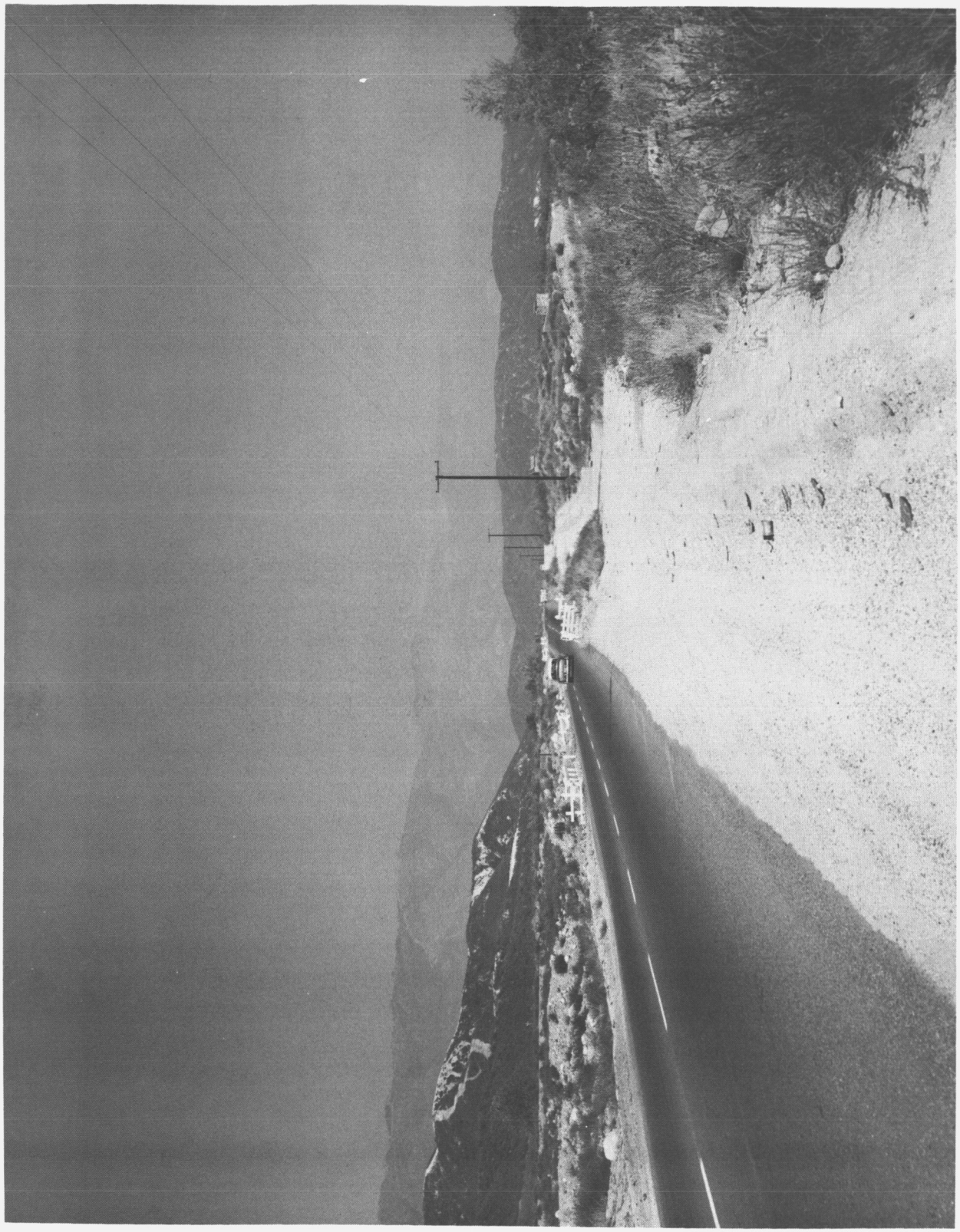

Figure C-11. Bridges and Shoe-fly on Devore Road, San Bernardino, California (looking northeast)

CONFIDENTIAL

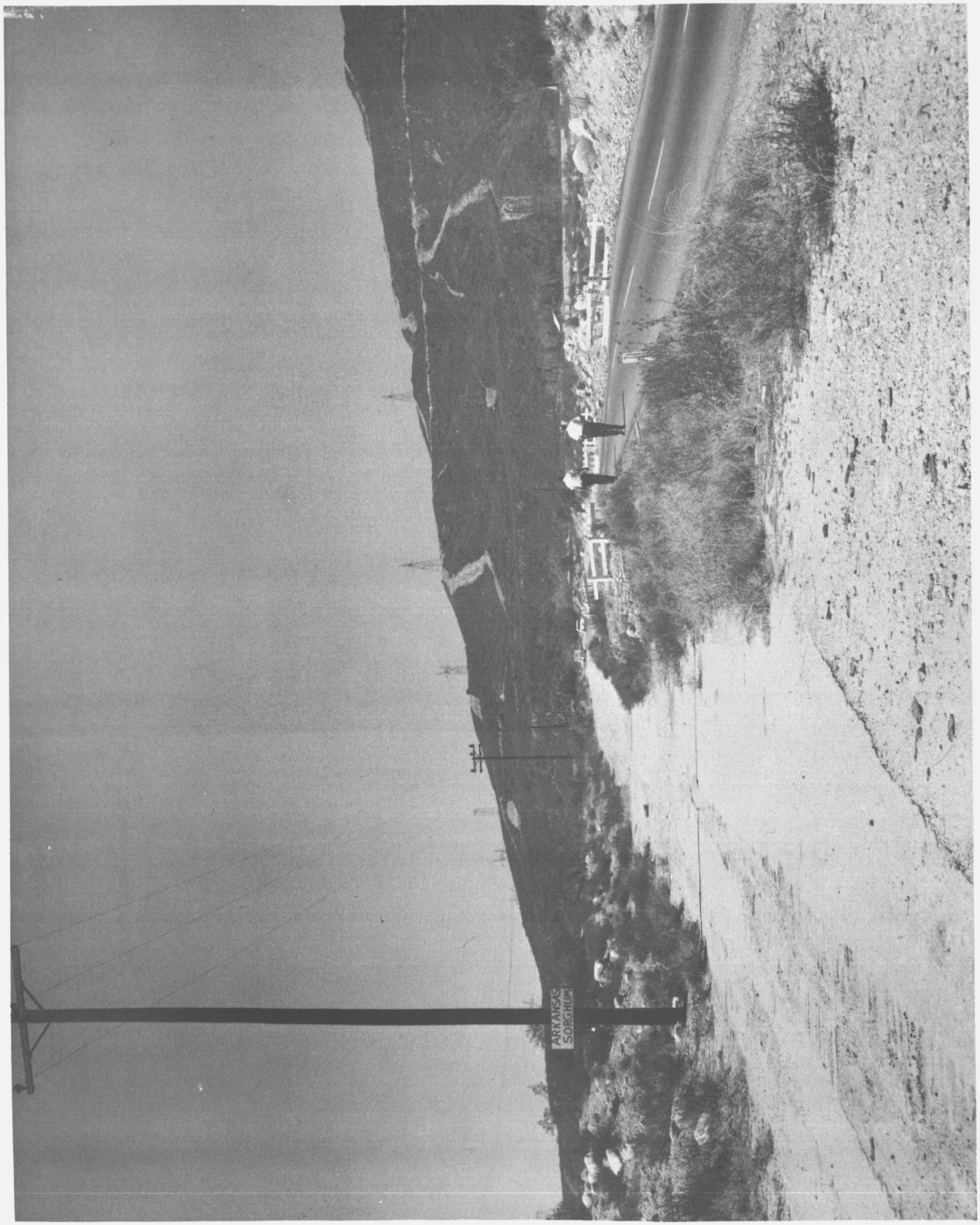

Figure C-12. Bridge and Shoe-fly on Devore Road, San Bernardino, California (looking southwest)

CONFIDENTIAL

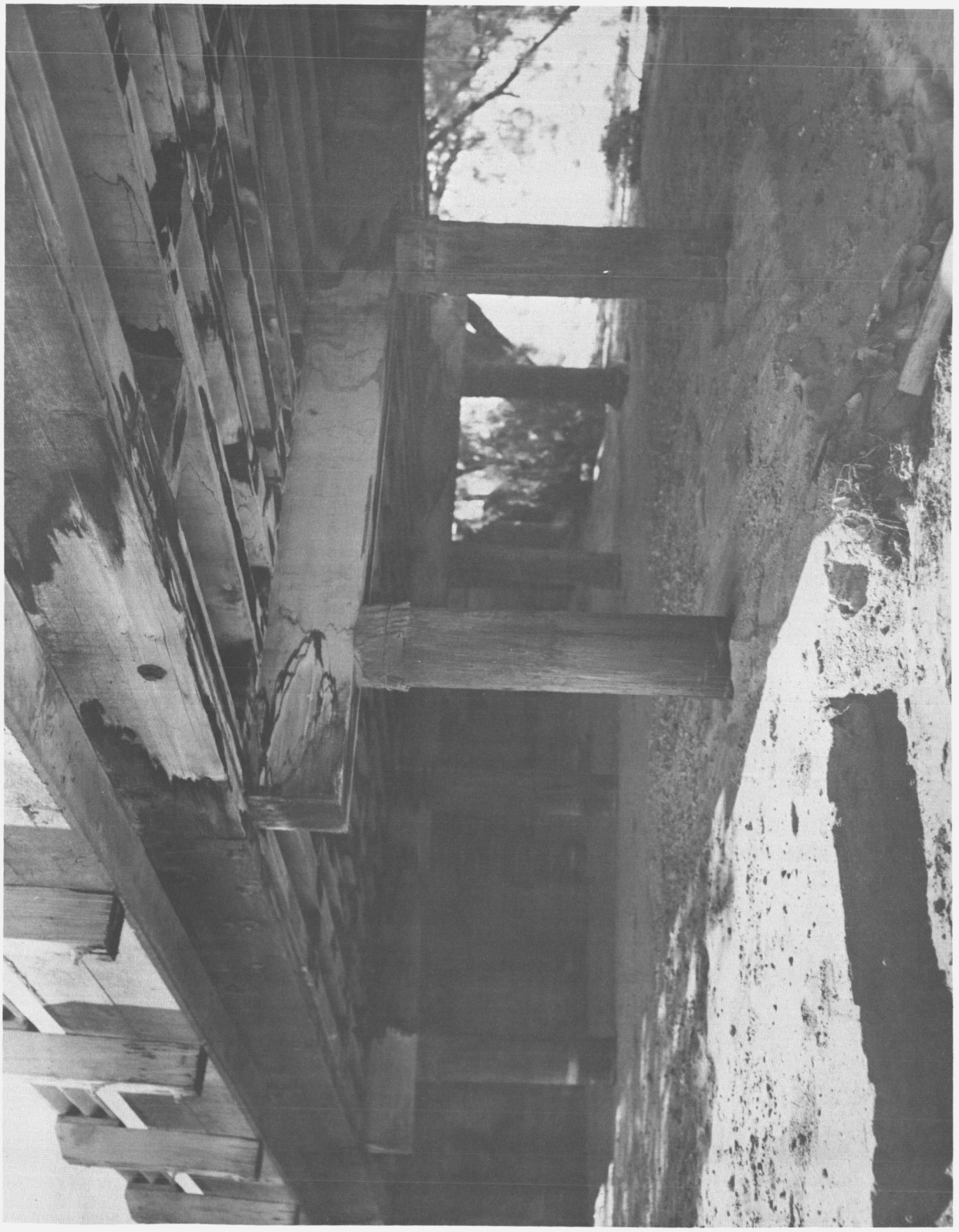

Figure C-13. Typical Bridge Structure of Bridges between Barstow, California and Baker, California

CONFIDENTIAL

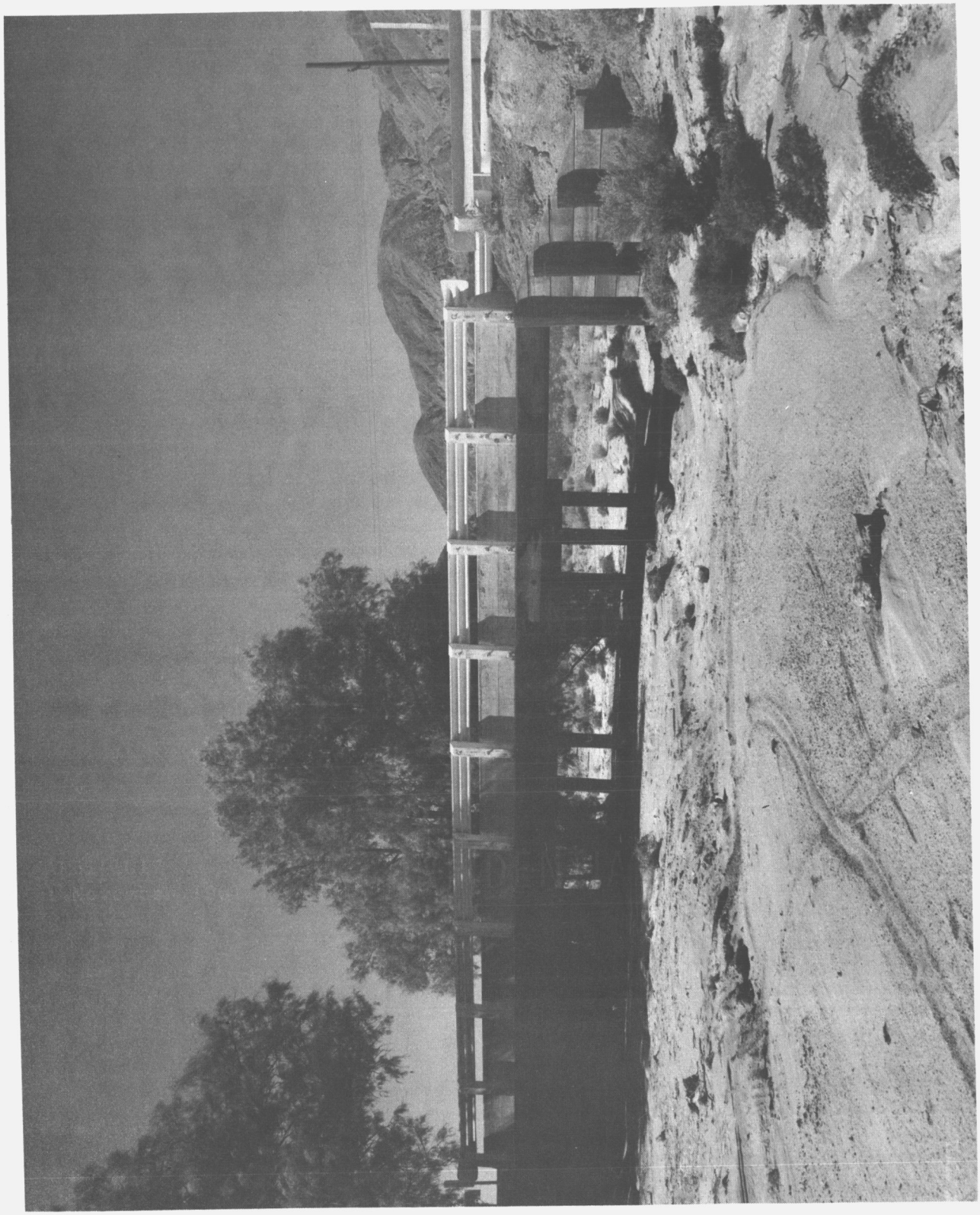

Figure C-14. Bridge, 60 feet long, 12 miles east of Barstow on Highway 91/466

CONFIDENTIAL

lengthwise with the road, and are 20 feet in length, see Figure C-13. Forty-three of these bridges have a span of 20 feet; two bridges have a span of 60 feet (see Figure C-14); and one has a span of approximately 200 feet. The bridges are all wide enough, 26 feet from guard rail to guard rail (no curb), for a large size transport trailer.

The allowable axle loading permitted on bridges from San Diego, California to Riverside, California is presented in Table C-1.

Table C-1 Bridge Loading, San Diego to Riverside

NUMBER OF AXLES	ALLOWABLE AXLE LOADING PERMITTED ON BRIDGE
1 Axle	27,000 lb
2 Axles	46,200 lb
2 Axles with 16 tires	53,100 lb
2 Axles on over width unit (extra tires)	57,300 lb
3 Axles	49,400 lb
Gross loading permitted	152,000 lb (includes tractor, trailer and load)

NOTE: Values quoted by California State Highway Department.

The allowable axle loading permitted on bridges from Barstow, California to California/Nevada State line is presented in Table C-2.

Table C-2 Bridge Loading, Barstow to State Line

NUMBER OF AXLES ON TRAILER	ALLOWABLE AXLE LOADING PERMITTED ON BRIDGE
1 Axle	23,400 lb
2 Axles	40,000 lb
2 Axles (16 tires)	46,100 lb
2 Axles on over width unit (extra tires)	50,100 lb
3 Axles	43,000 lb
Gross loading permitted	130,000 lb (includes tractor, trailer and load)

NOTE: Values quoted by California State Highway Department.

These bridge loadings are conservative and are not considered maximum loadings. A means of increasing the loading of a bridge, if necessary, can be accomplished by planking to distribute the load over a wider area of the bridge.

C.1.4.3 Dips and Humps. There are numerous dips and humps encountered along the route from Etiwanda Avenue (San Bernardino, California) to Lathrop Wells, Nevada. Fill can be moved into dips and be used to shape-up humps which present any problem. Figure C-15 shows typical dips encountered. The dips shown here measure 250 feet from crest to crest.

C.1.4.4 Railroad Crossings. One railroad crossing, 75.6 miles from San Diego, California, on Van Buren Boulevard, in Riverside, California, at the intersection with U.S. Highway 395, may present a problem to trailer road clearance (see Figure C-16). The crossing is forty-eight feet from the west side of U.S. Highway 395 on Van

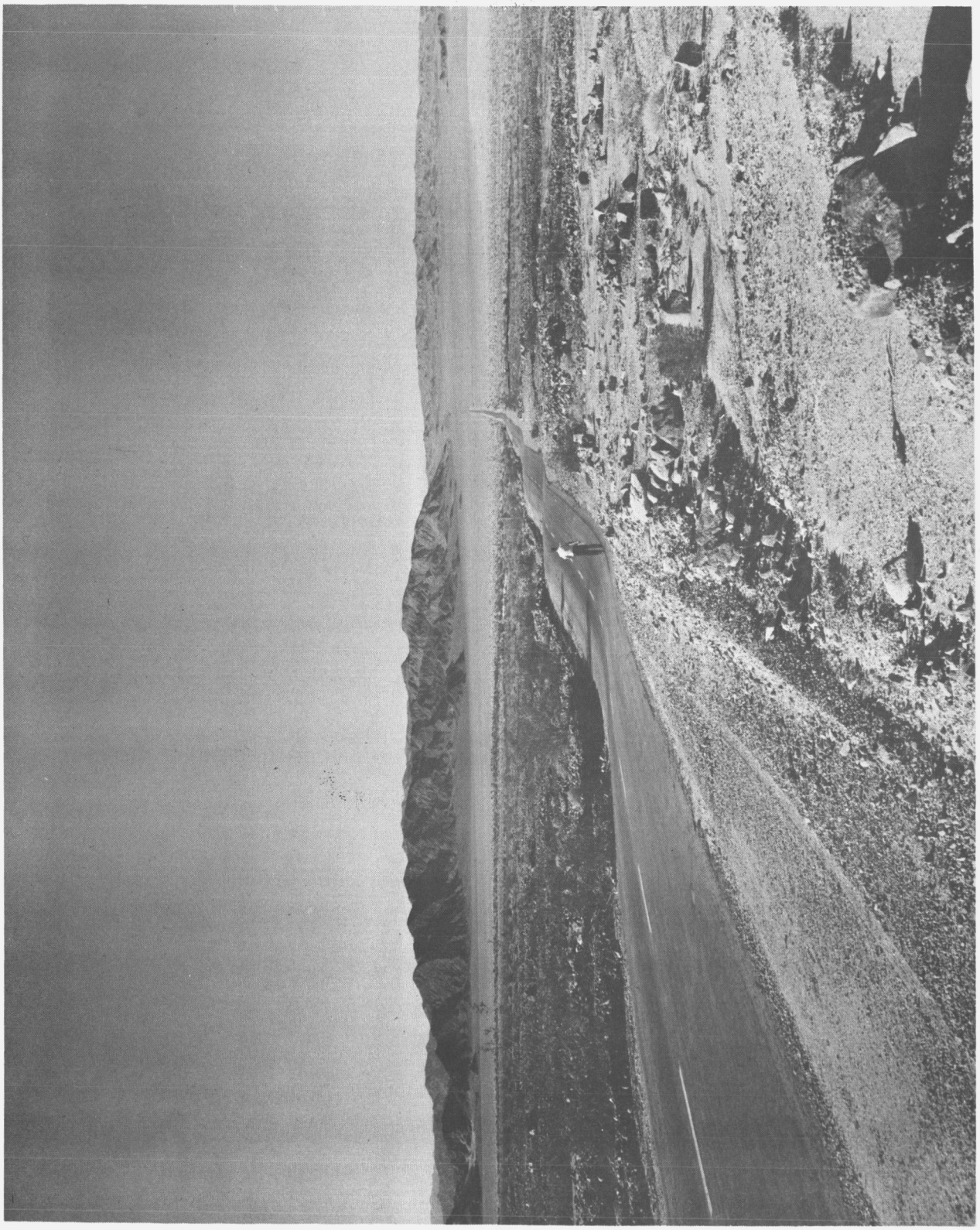

Figure C-15. Typical Dips on California State Highway 127 (looking north)

CONFIDENTIAL

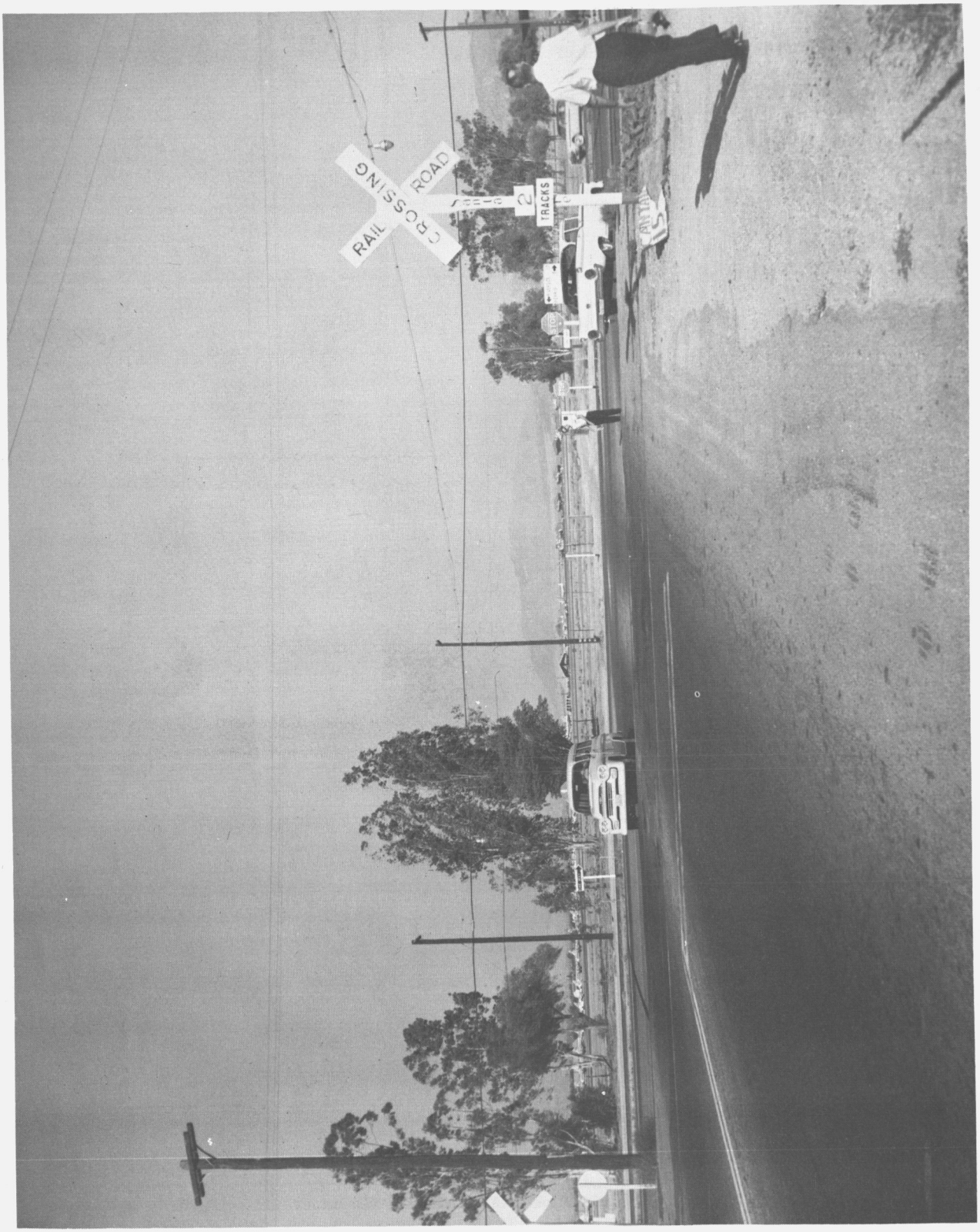

Figure C-16. Railroad Crossing at Intersection of Van Buren Boulevard and U. S. Highway 395 south of Riverside, California (looking east)

CONFIDENTIAL

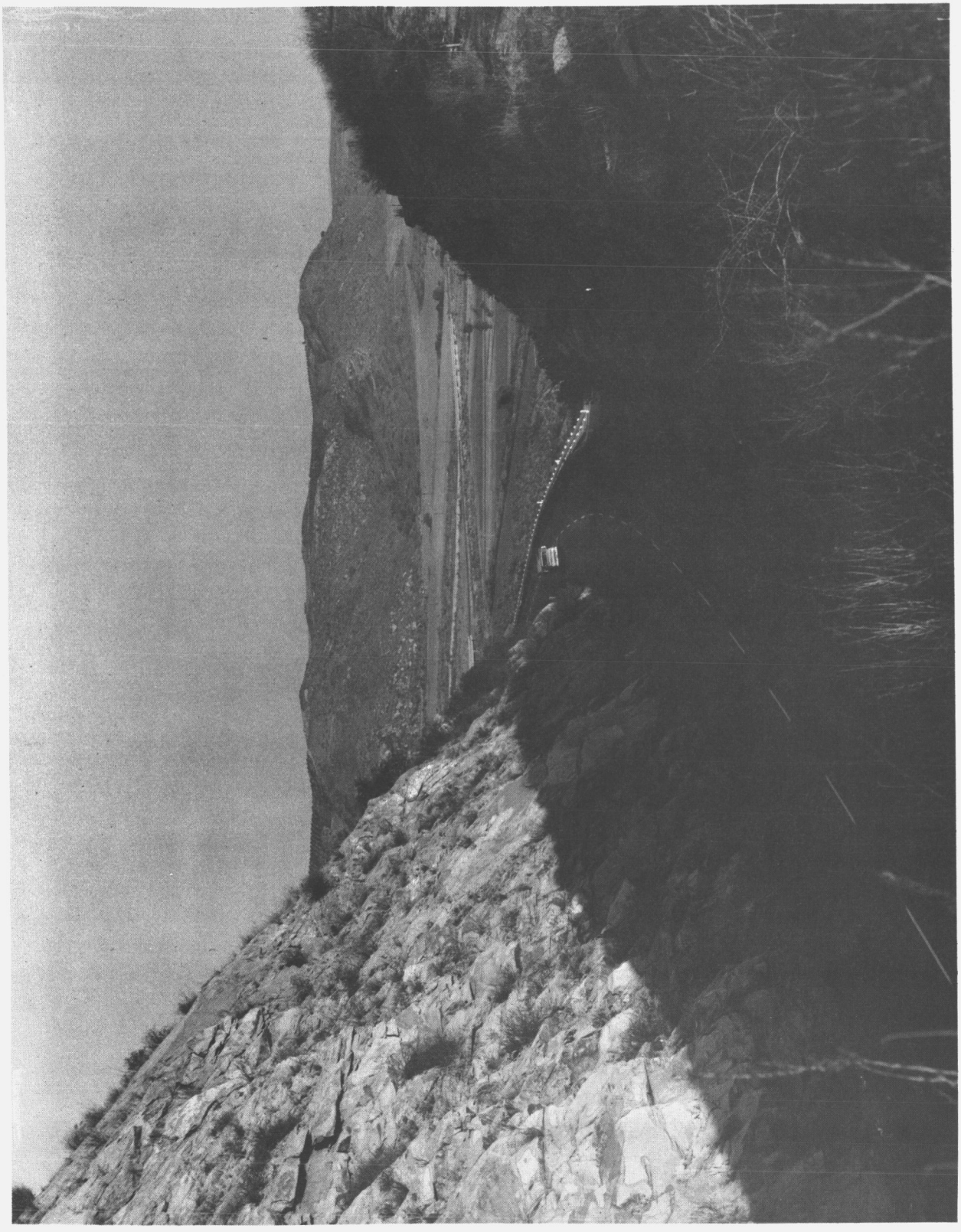

Figure C-17. Typical Curve - This curve is north of Escondido, California on U. S. Highway 395 (looking north).

Buren Boulevard and rises four feet to the crest in this distance. The road levels off at the height of the crest. Fill can be used to decrease the slope at this crossing.

C.1.4.5 Curves. Curves on the route surveyed are not sharp enough to present any problem with the length of trailer suggested. A typical curve, encountered north of Escondido on U.S. Highway 395, 34.4 miles from San Diego, California, is shown in Figure C-17.

C.1.4.6 Against Traffic Travel. At one point in the route, travel must be made against traffic. At a distance of 115.2 miles from San Diego, California on Devore Road, a left turn (north) is made onto Cajon Boulevard (San Bernardino, California) which is old U.S. Highway 66 (see Figure C-18). Traveling south on U.S. Highway 395, Cajon Boulevard is an exit off U.S. Highway 395 and intersects with Devore Road. To proceed north and avoid an overpass on U.S. Highway 395, travel must be made on Cajon Boulevard against traffic until reaching U.S. Highway 395. Southbound traffic on U.S. Highway 395 must be stopped until a crossing can be made to the east side of the highway.

C.1.4.7 Turn, 360 Degrees. At the intersection of State Highway 2/138 and Phelan Road 39 miles north of San Bernardino, California, a 360 degree turn must be made in order to enter Phelan Road. This turn can be accomplished easily since there is a large flat area on the north west side of State Highway 2/138 at the intersection. The turn-area consists of a hard rock/gravel/sand base and grading would present no difficulty.

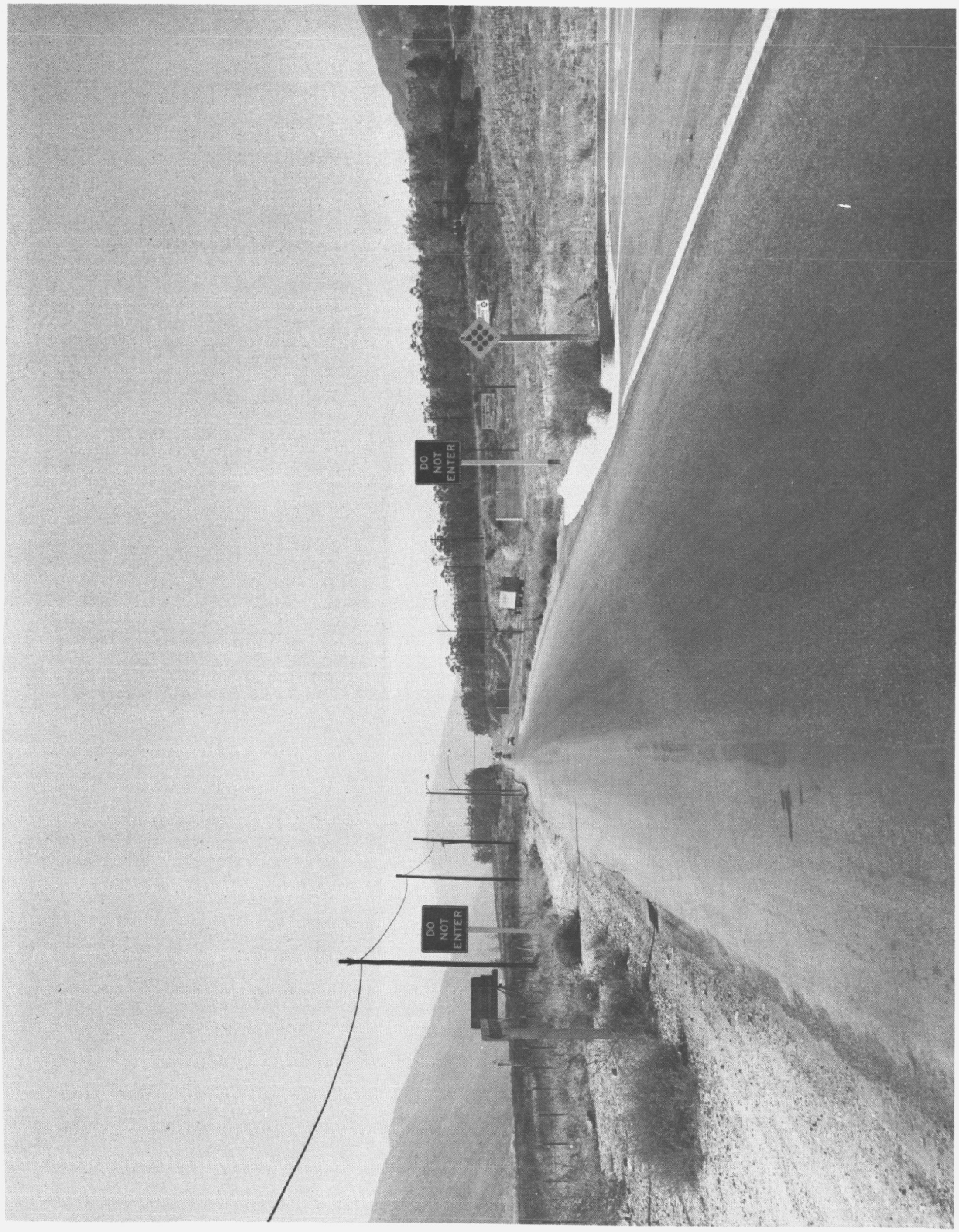

Figure C-18. Cajon Boulevard, North of San Bernardino, California

C.1.5 ROUTE

The route surveyed is described as follows:

a. Leave Gate 1, General Dynamics/Astronautics and proceed north on U. S. Highway 395.

b. Travel north on U. S. Highway 395, 68 miles, to San Jacinto Street at Perris, California.

c. Route through Perris, California, to avoid overpass: Turn left off U. S. Highway 395 onto San Jacinto Street. Turn right off San Jacinto onto Perris Blvd. Turn left off Perris Boulevard onto Nuevo Road. (All intersections can be negotiated easily). Turn right off Nuevo Road onto U. S. Highway 395.

d. Travel north 6.1 miles from Nuevo Road on U.S. Highway 395 and turn left (west) onto Van Buren Boulevard in San Bernardino, California.

e. Continue on Van Buren Boulevard through March Air Force Base and through Arlington, California, to Mira Loma, California. Make a right turn (north) onto Etiwanda Avenue at Mira Loma, California.

f. Proceed north on Etiwanda to Highland Avenue in San Bernardino, California. Turn right (east) onto Highland Avenue.

g. Travel east on Highland Avenue to Sierra Avenue (San Bernardino, California). Turn left (north) onto Sierra Avenue.

h. Travel north on Sierra Avenue to Devore Road (San Bernardino, California). Turn right (northeast) onto Devore Road.

i. Proceed northeast on Devore Road to Cajon Boulevard (San Bernardino California). Turn left (north) onto Cajon Boulevard going against traffic until reaching U. S. Highway 395. Turn left (north) onto Highway 395.

j. Travel north on U. S. Highway 395 to State Highway 2/138 (28 miles north of San Bernardino). Turn left (northwest) onto State Highway 2/138.

k. Proceed northwest on State Highway 2/138 to Phelan Road (Phelan, California). A 360 degree turn must be made here to enter Phelan Road which runs east.

l. Continue east on Phelan Road to junction with U. S. Highway 91/395 (north of San Bernardino). Turn left (north) onto U. S. Highway 395. U. S. Highway 91 continues northeast.

m. Proceed north on U. S. Highway 395 to Kramer, California. Turn right (east) onto U. S. Highway 466.

n. Travel east on U. S. Highway 466 to Barstow, California; here U. S. Highway 466 and U. S. Highway 91 junction. Continue on U. S. 466/91 to Baker, California. Turn left (north) off U. S. Highway 466/91 onto California Highway 127.

o. Continue north on State Highway 127 to California/Nevada state line where State Highway 127 becomes Nevada State Highway 29. Proceed north on State Highway 29 to Lathrop Wells. Turn right (east) onto U. S. Highway 95.

p. Travel east on U. S. Highway 95, 23.5 miles to intersection of road leading to test site. Turn left off U. S. Highway 95 onto test site entrance road. Proceed north on test site entrance road five miles to Main Gate entrance.

Table C-3 Wire Obstructions*

MILES FROM PLANT 71	IDENTIFICATION POINT	POINT TO POINT COUNT CABLES	WIRES	OTHER OBSTRUCTIONS
0.0	Plant 71	0	0	Gate 1, personnel entry to be made removable
0.2	Junc. US 395 and Claremont Mesa Drive			Enter 395 by running over curb on one side 24' wide; side railing 2' high
16.0	Bridge			
46.1	Cross Junc. State Highway 74	9	210	
48.5		1	115	1 light hanging in center of road
67.2	Perris, California Junction State Highway 74	1	91	1 light hanging in center of road
	Left on State Highway 74			1 Highway blinker side of road
67.8	Junc. D St. Right on D St	3	4	
68.7	Junc. US 395. Left on 395	0	17	
75.2	Junc. Van Buren St. Riverside Left on Van Buren	1	29	
94.2	Junc. Etiwanda Ave. Left on Etiwanda	21	377	1 stoplight hanging from post; 2 high-tension wires questionable

Table C-3 Wire Obstructions*
(Continued)

MILES FROM PLANT 71	IDENTIFICATION POINT	POINT TO POINT COUNT CABLES	WIRES	OTHER OBSTRUCTIONS
102.1	Junc. with Highland Ave. Right on Highland	9	330	
106.8	Junc. with Sierra Way Left on Sierra Way	6	62	
109.1	Junc. with Riverside Dr. Left on Riverside	2	6	
111.0	Junc. with Devore Rd. Right on Devore Rd. with dips in Devore Rd.	0	8	
114.0	Junc. with Old 395. Left on Old 395 - have police stop all traffic on old 395			
114.2	Junc. 395 Freeway Left on 395. Do not use overpass	1	20	
122.6	Junc. State Highway 138 Left on 138	1	39	
135.3	Junc. Phelan Rd. Right on Phelan Rd. Make right turn by circle thru Real Estate Office Yard. Watch dips in road. Cross summit, 4802 ft. Elevation	2	96	
146.0	Junc. with U. S. 95 Left on 395	1	51	

Table C-3 Wire Obstructions*

(Continued)

MILES FROM PLANT 71	IDENTIFICATION POINT	POINT TO POINT COUNT CABLES	WIRES	OTHER OBSTRUCTIONS
151.2	Cross Junc. Palmdale Rd.	0	5	1 light hanging in center of road
183.4	Kramer Junc. with U. S. 466. Right on 466 (At this point turn left to Edwards Air Force Base)	0	40	
212.4	Left on U. S. 466 at Barstow	7	235	1 possible tree trimming near Hinckley Rd. Junc.
212.5	Right on U. S. 466	1	16	
213.1	Junc. with U. S. 91 Left on 91	2	16	
271.0	Junc. with State Highway 127 at Baker. Left on 127	4	99	1 light hanging in center of road
373.6	Junc. with U. S. 95 at Lathrop Wells, Nevada Right on U. S. 95	0	36	
395.0	Junc. Mercury Turn-Off Left on Mercury Rd. 5 miles to Test Sites	0	32	
400	Total Mileage Plant 71 to Test Site	74	1986	

* Extracted from Feasibility of Road Transport of Nuclear Stages to the Nevada Test Site, H. Cherin, PDSA37-61, General Dynamics/ Astronautics, 10 May 1961.

Table C-4 Points of Interest Investigated

MILES FROM PLANT 71	POINTS INVESTIGATED
3.7	Bridge - 32 ft wide (rail to rail) Railing - 2.6 ft high Curb - 8 inches
8.7	Bridge - 30.3 ft wide (rail to rail) Railing - 2.4 ft high Curb - 1 ft high Roadbed - 28 ft wide (curb to curb)
14.7	2 through-cuts (not limiting)
15.4	Bridge - (same measurements as bridge at 8.7 mi)
16.6	Bridge - 30 ft wide (rail to rail) Railing - 2.4 ft high Curb - 8 inches Roadbed - 26.2 ft wide (curb to curb)
20.4	Escondido (south) 2 large trees to be trimmed
20.7	SH 78 junctions with US Highway 395
20.9	Bridge - 34.0 ft wide (rail to rail) Railing - 3 ft high Curb - 1 ft high Roadbed - 28.5 ft wide (curb to curb)
22.6	Bridge (same as above)
26.7	Trees to be trimmed
28.5	Trees to be trimmed
30.1	Through-cut, 38 ft from rock face to rock face at road level. Rock is vertical up to approximately 10 ft then widens on a 1 to ¾ slope
30.9	Through-cut 38 ft from rock face to rock face at road level. Rock is almost vertical from road level to height of cut. Would require extensive blasting

Table C-4 Points of Interest Investigated
(Continued)

MILES FROM PLANT 71	POINTS INVESTIGATED
	and blade work to widen this through-cut. This through-cut will limit width of load, however a 36 ft vessel (dia.) could be brought through here for cut is only about 0.2 mi long
34.4	Through-cut 44 ft wide from rock face to rock face at road level. This cut is on a slight curve but should pose no problem for bringing a 120 ft length object through here
35.0	Bridge 28 ft roadbed (not limiting)
35.2	Bridge (not limiting)
35.8	Junction - SH 76 with U. S. Highway 395
46	Bridge over Temecula River (not limiting)
49.5	Bridge - 30 ft wide (rail to rail) Railing - 2.5 ft high Curb - 27 ft (curb to curb)
50.6	Bridge (not limiting, same as above)
51.2	Junction Highway 71 with 395
65.1	SH 74 leaves Highway 395 to right
67.5	Perris, Calif. - Construction of overpass at this point; however it is possible to leave Highway 395 onto up-ramp on right side of overpass, cross road of overpass and enter down-ramp exiting onto 395 again. Rockbed will be 24 ft wide with 6 ft shoulders. No curve will have to be negotiated upon entering 395 again.
**67.2	(An alternate route could be taken through Perris, however, on overpass out of town and entering into 395 using the down-ramp would require negotiating a sharp curve which would present problems with a very long trailer)

Table C-4 Points of Interest Investigated
(Continued)

MILES FROM PLANT 71	POINTS INVESTIGATED
68.0	Left turn off U. S. Highway 395 onto San Jacinto. (no problem)
68.3	Right turn off San Jacinto onto Perris Blvd. There is an empty lot on the right corner of this intersection and a long trailer could make this corner easily. (This is not a limiting intersection)
69.3	Left turn-off Perris Blvd onto Neuvo Road. (This is not a limiting intersection)
69.5	Turn right off Nuevo Road onto U. S. Highway 395. Wheels of trailer may have to go off pavement onto dirt when making this turn but this is a large intersection due to a vacant lot at the corner. (not a limiting intersection)
75.6	Left turn off U. S. Highway onto Van Buren Ave. (March AFB) (not a limiting intersection). Bad hump at RR crossing 4 ft rise in 48 ft
85.6	1 mile row of trees (palm). 45 ft width between trees across road. 23 ft roadbed
86.0	Arlington ATSF crossing. Signals must be removed, and the crossing has a 5 ft rise in 80 ft on the approach and 5.5 ft rise in 126 ft slope leaving the crest of the rise
89.8	Santa Ana river bridge - not limiting
94.8	Turn right off Van Buren onto Etiwanda
97.8	Trees to be trimmed
98.7	Southern Pacific RR crossing
100.4	ATSF crosses Etiwanda
101.2	Foothill Blvd. crosses Etiwanda

Table C-4 Points of Interest Investigated
(Continued)

MILES FROM PLANT 71	POINTS INVESTIGATED
102.3	Trees will need trimming
102.4	Pacific Electric RR crossing
103.2	Turn right on Highland Ave. (This could be the limiting intersection). Dimensions are shown in Figure C-5. Eucalyptus trees line the right side of this road with Palm trees lining the left side. Forty-one ft is the shortest distance between these trees across the road. There are 3 or 4 humps which could cause trouble depending on trailer clearance
107.9	Turn left off Highland onto Sierra Ave. There is an empty lot on the northwest corner which will increase turn-area. Not as limiting as the intersection at Etiwanda and Highland
111.2	Right turn onto Devore Road. Here again the turn will not be as limiting as the intersection at Etiwanda and Highland
111.6	Four wooden bridges - Structural members are 2 X 12 inch wooden beams on end with asphalt covering. Span is 20 ft Width of Bridge, rail to rail, 24 ft Roadbed - 22.5 ft Curb - 8 inches high Railing 2.5 ft high If structure of bridge is not heavy enough to allow weight required to pass over, there is a possibility of bypassing the bridges by means of a shoe-fly on right side of bridge. This shoe-fly is partially paved but would need fill. Three telephone poles would have to be removed There are also dips on this road which might cause clearance trouble. Worst dip is 162 ft from peak to peak and it drops down 3 ft in 30 ft near one peak. Fill may be required.

Table C-4 Points of Interest Investigated
(Continued)

MILES FROM PLANT	POINTS INVESTIGATED
115.2	Turn left off Devore onto old US Highway 66 which is called Cajon Blvd. Vehicle would have to go against traffic until it reaches freeway, cut across freeway to right side of freeway then proceed on 395 north
123.7	Left off US Highway 395 onto SH 2/138. Dips along this road. Counted 25 dips
135.4	Turn off SH 2/138 onto Phelan Road. At this intersection a 360 degree turn must be made in order to enter Phelan Road. This turn can be negotiated easily since the left side of SH 2/138 is essentially bare and would need only a little blade work to prepare the turn area Phelan Road at its minimum width is 17 ft wide. Road work can be done on both sides of roadbed for shoulders are hard and there is plenty of fill nearby. This fill consists of hard gravel, rock, and sand. There are numerous dips and humps on this road but only a few are severe enough to pose the problem of fill.
146.4	High-tension lines, approximately 25 ft high off roadbed level would have to be raised
147.2	Turn left off Phelan Road onto US Highway 395
184.8	Kramer Junction with US Highway 466; turn right off Highway 395 onto US 466
205.6 206.2	Trees to be trimmed
207.2	Cross at SF RR
213.8	Curve here, but should pose no problem
214.6	Curve here should pose no problem
219.5	Overpass being built over US Highway 91 but there is room to go up up-ramp off US Highway 91 over road on overpass then down down-ramp onto frontage road, off frontage back onto US Highway 91. These ramps are 24 ft wide with 6 ft shoulders

~~CONFIDENTIAL~~

Table C-4 Points of Interest Investigated
(Continued)

MILES FROM PLANT	POINTS INVESTIGATED
225.9	Bridge - 26 ft rail to rail (on US Highway 91) No curbs Railings - 2 ft Structure - Wooden 6 X 15 inch members spaced 2 ft apart running lengthwise with road, 20 ft long, 3 spans. Each span is supported by four 12-inch diameter pilings
226.4 to 271.4	44 bridges of wooden construction as previously described at 225.9 mi
271.6	Bridge - 26 ft rail to rail, approx. 200 ft long. Constructed with wooden members as described at 225.9 mi
271.8	Left off US Highway 91 onto SH 127 at Baker
299.3	Dips and rises in road 250 ft from crest to crest
322.0	32 ft wide through-cut with a 1 to ¾ slope on each side of road. Walls rise to about 10 ft. Should not pose a problem
324.5	Trees to be trimmed at Shoshone
325.3	Through-cut 28 ft wide at road level; 32 ft wide at six ft above road level. Widens to 50 ft at top of cut. Right wall (East wall) rises to approx. 15 ft high at a 1 to ¾ slope. Left wall (West wall) rises to approx. 25 ft high with a 1 to ¾ slope. Right wall can be bladed down for it is made of fractured and cracked malapi rock
349.3	Death Valley Junction
371.6	Lathrop Wells
395.1	Turn left off US Highway 95 onto road leading into test site
398.0	Overhead cable to be moved
399.5	Main gate into Test Site

~~CONFIDENTIAL~~

C.1.6 Cost. The cost of transporting a 36 x 100-foot stage from A.F. Plant 71 to Mercury, Nevada, will depend primarily upon the difficulties that arise in relocating and raising the telephone and power lines and cables that presently interfere with the described route. The determination of this exact cost would require a detailed study of each wire and cable along the route and the identification of the specific modification or adjustment required in each case. An analysis of this type was not within the scope of this survey. However, an area cost estimate was developed based on previous detailed transportation studies performed on the S-II. This area estimate is made up of the following costs:

a.	Basic Transportation (prime mover and escort vehicle rental, crew costs, right-of-way permits, police escorts and insurance	$ 20,000
b.	Permanent Route Modifications (tree removal, widening road cuts, minor road changes, sign relocation)	8,000
c.	Temporary Route Modifications (tree trimming, dip filling, etc.)	7,000
d.	Wire, Cable and Signal Relocations	180,000
	First Trip	$215,000
	Subsequent Trips	27,000

Item (d) is based on a semi-permanent change, a large number of which are required regardless of the number of trips that are planned. Temporary arrangements would reduce this approximately 50 percent so that a single trip might be expected to cost about $125,000. If three or more trips were planned, it is likely that permanent wire, cable, and signal changes would be the most economical alternative.

This page intentionally left blank.

APPENDIX D
PRELIMINARY PERFORMANCE ANALYSIS

The first phase of the Saturn D study was conducted using exclusively the preliminary Saturn C-1 and C-2 configurations (257-inch diameter). This appendix summarizes the parametric study that was performed based on use of these configurations; the method of analysis, basic assumptions, payload curves and trajectories are included in this appendix. The design point was maximum payload to escape velocity.

D.1 CONFIGURATIONS. Five configurations emerged from the integration of the C-1, C-2, and the two nuclear stages with thrust levels of 70.5 K and 190 K. All five configurations can perform useful missions of various scope, from orbital to interplanetary. The C-1 configuration is combined with the SN-I or SN-II for a two-stage configuration, and with both the SN-I and SN-II for a three-stage configuration. The C-2 configuration (S-I, S-II) is used in conjunction with the SN-I, or SN-II as third stages. Table D-1 describes the thrust levels, jettison weights, and propellant capacity of each stage.

D.2 PERFORMANCE CRITERIA. The initial performance criterion was a minimum launch thrust-to-weight ratio of 1.2. Previous experience had demonstrated that a lower value evolves excessive gravity losses and creates launch stability problems. A higher initial thrust-to-weight ratio for the three-stage configurations compromises the realization of the nuclear stage full potential. The dynamic pressure at first staging was constrained to 400 psf in accordance with a previous S-I booster dynamics analysis. The jettison weights for the S-I and S-II stages were obtained from preliminary information provided by NASA on the C-1 and C-2 configurations. The nuclear stages' jettison weights were expressed as a function of propellant weight by the formulas:
$Wj = 18{,}500 + 0.0909\ (Wp - 50{,}000)$ for the SN-I and $Wj = 21{,}500 + 0.0909\ (Wp - 50{,}000)$ for the SN-II.

CONFIDENTIAL

Table D-1 Stage Comparisons

	S-I (CHEMICAL)	S-II (CHEMICAL)	SN-I (NUCLEAR)	SN-II (NUCLEAR)
Thrust (lb)	1,500 K	800 K	70.5 K	190 K
Propellant	LO_2/RP-1	LO_2/LH_2	LH_2	LH_2
Propellant Capacity (lb)	650,000 (C-2) 750,000 (C-1)	330,000	Variable	Variable
Jettison Weight (lb)	112,680 (C-2) 115,180 (C-1)	31,460	Variable	Variable
ISP (sec)	257 (S.L.)	428	812	820

These formulas were derived from several design points for a 257-inch tank diameter. A 16 second coast period, in lieu of thrust transient start, was inserted prior to the nuclear stage full thrust. After staging, aerodynamic effects were considered negligible.

D.2.1 Performance Analysis Technique. Trajectories for all configurations were simulated on the 7090 IBM electronic computer. A launch from AMR, a rotating spherical earth and an azimuth of 105° were assumed. Initially full loading of the nuclear stages, compatible with the launch thrust to weight ratio, was adopted. This was varied until a maximum payload to escape was attained. A spectrum of pitch angles and vertical flight times was analyzed in order to minimize gravity, drag, and misalignment losses. In the case of the three stage configurations, propellant off-loading in the S-I and S-II were given careful consideration, and trade-offs were established.

D.3 VEHICLE PERFORMANCE

a. S-I, SN-I. The first configuration analyzed was the two-stage S-I, SN-I vehicle. The S-I stage, fully loaded, consumes 750,000 pounds of propellant. The thrust-to-weight ratio of the nuclear second stage is varied until the maximum payload of approximately 20,000 pounds to escape velocity is attained. This requires a propellant consumption of 90,000 pounds. Figure D-1 illustrates the payload variation versus propellant consumption for several missions. As can be observed, the curves are relatively flat over the range of nuclear stage thrust-to-weight ratios examined. The left side payload decrease is the result of insufficient propellant loading to realize the full nuclear stage potential. The right extremity of the curves demonstrates the effect of excessive velocity losses incurred by low thrust-to-weight ratio. A typical trajectory is plotted in Figure D-2.

b. S-I, S-II, SN-I. In order to obtain an initial thrust-to-weight ratio of 1.2, the launch weight of the three-stage vehicle is fixed at 1,250,000 pounds. This necessitates off-loading of propellant in the chemical stages. Since the S-II has the higher

specific impulse of the first two stages, it is kept fully loaded while the propellant weight in the S-I is decreased to 620,300 pounds. The payload versus nuclear stage propellant weight is plotted in Figure D-3. The maximum payload to escape velocity is 57,700 pounds for an SN-I propellant consumption of 85,400 pounds. A trajectory to the 100 nautical miles orbit for a nuclear stage thrust-to-weight ratio of 0.455 is presented in Figure D-4.

c. S-I, S-II, SN-II. As in the previous configuration, the launch weight was set at 1,250,000 pounds. Since the thrust of the nuclear third-stage is 190 K, the stage weight shows a considerable increase over the nuclear stage weight of the SN-I. As a result, off-loading of both the S-I and S-II stages is necessary. For comparison purpose, trajectories with initial thrust to weight ratio of 1.25 were simulated. The result is a 12 percent net payload loss for escape velocity. The payload curves for launch thrust-to-weight ratios of both 1.2 and 1.25 are shown in Figures D-5 and D-6 and a typical trajectory is plotted in Figure D-7.

d. S-I, SN-II. The technique for payload optimization of this configuration is similar to that applied to the two stage S-I, SN-I vehicle. The thrust-to-weight ratio variation of the nuclear stage, ranging from 0.7 to 0.85 appears to have slight effect on the payload. Figure D-8 illustrates payload for various missions versus nuclear stage propellant weight, and the maximum payload trajectory is plotted in Figure D-9.

e. S-I, SN-II, SN-I. In the analysis of this configuration two approaches were examined. The first one uses a suborbital start of the SN-I while the second method operates the SN-II to the 100 nautical mile orbit, jettisons the empty weight and allows the SN-I to complete the mission. The latter method proves to be the more advantageous. However, as Figure D-10 shows clearly, the SN-I combined with the SN-II does not offer any performance gain over the two stage S-I, SN-II configuration for escape. In fact, the result is a lower payload. However, as the mission velocity requirements increase, the two nuclear stages combined gradually overtake and exceed the single nuclear stage capability.

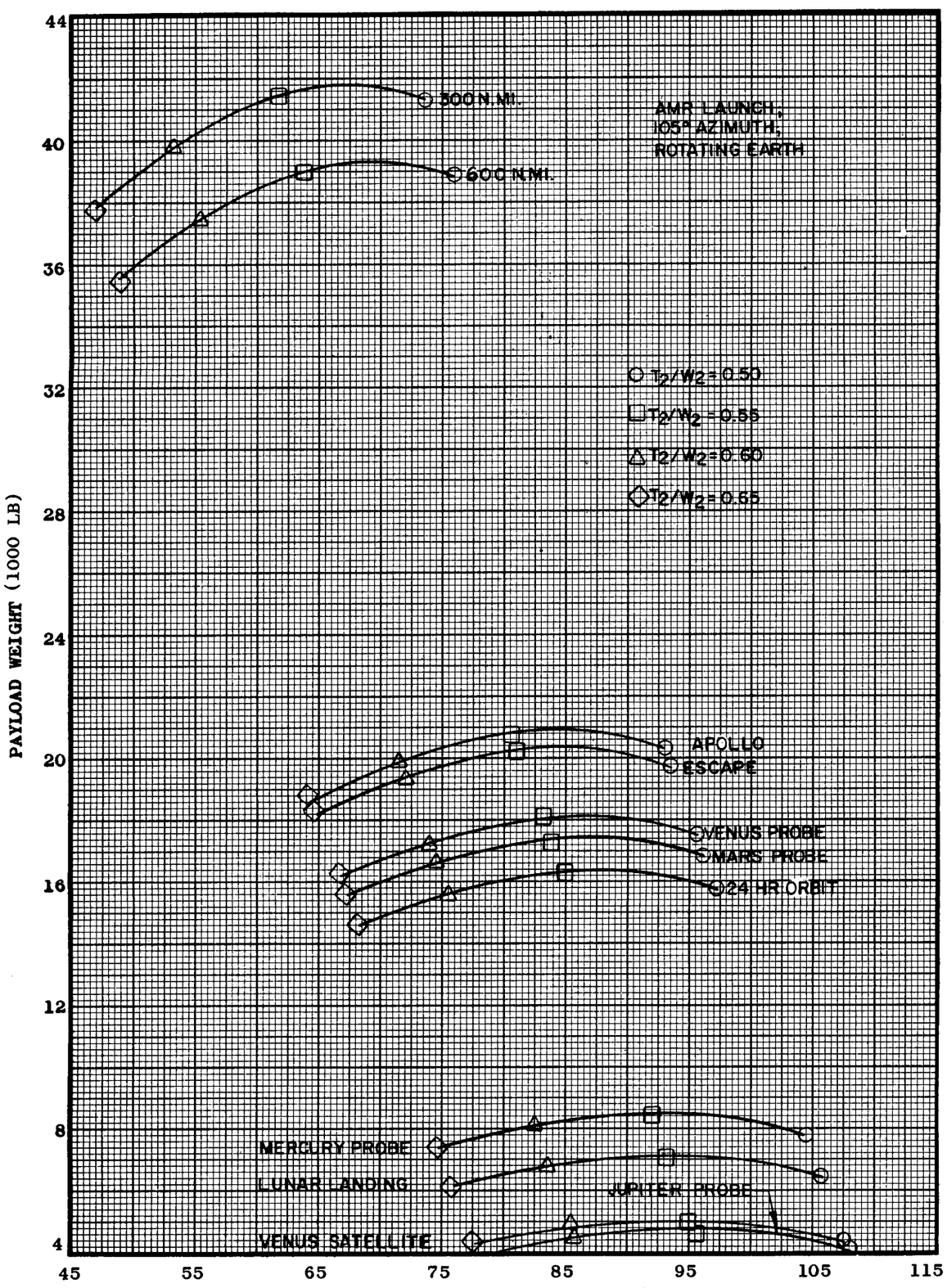

Figure D-1. Payload Vs Nuclear Stage Propellant Weight for S-I, SN-I

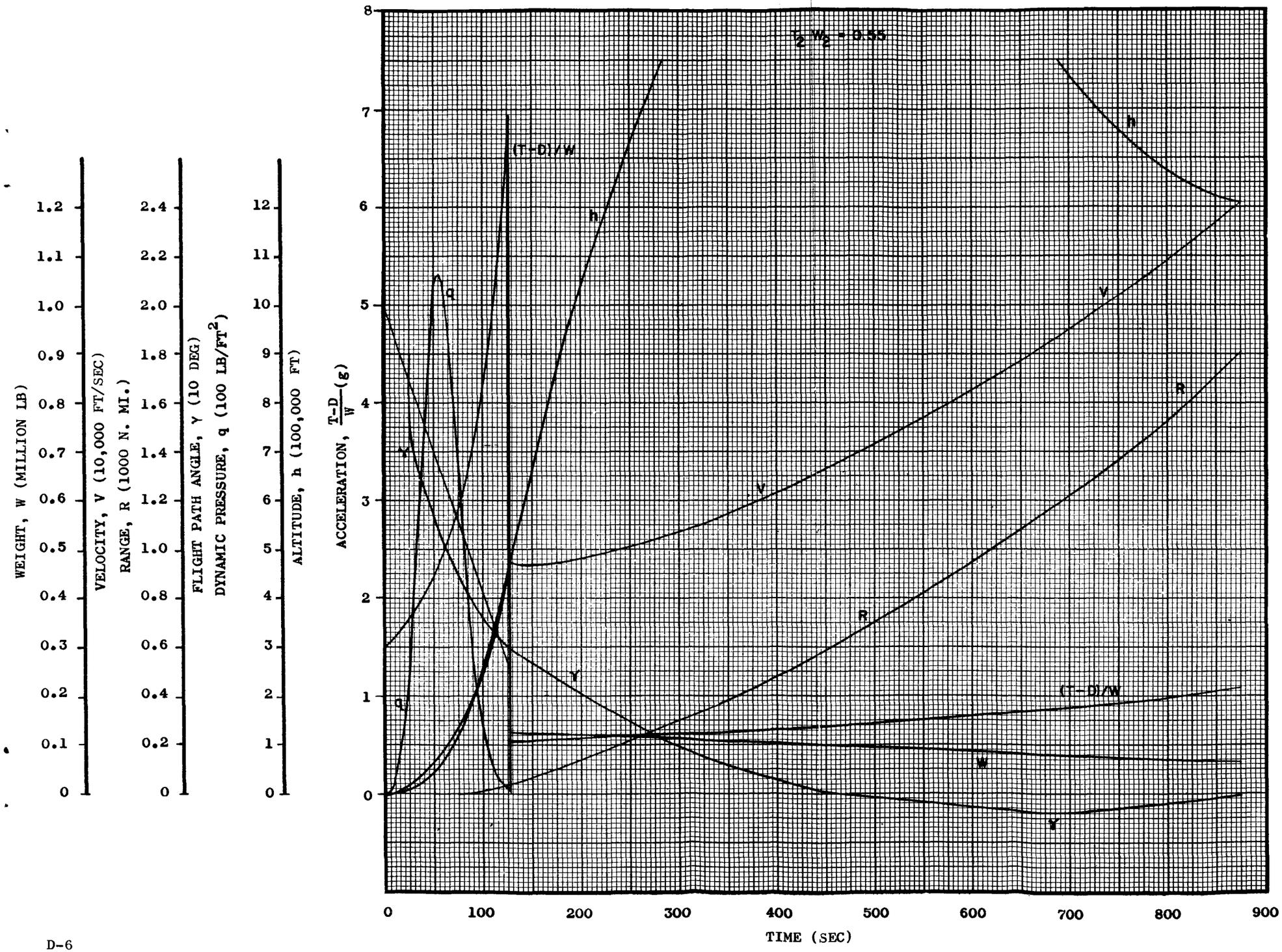

Figure D-2. Typical Launch Trajectory for S-I, SN-I Vehicle

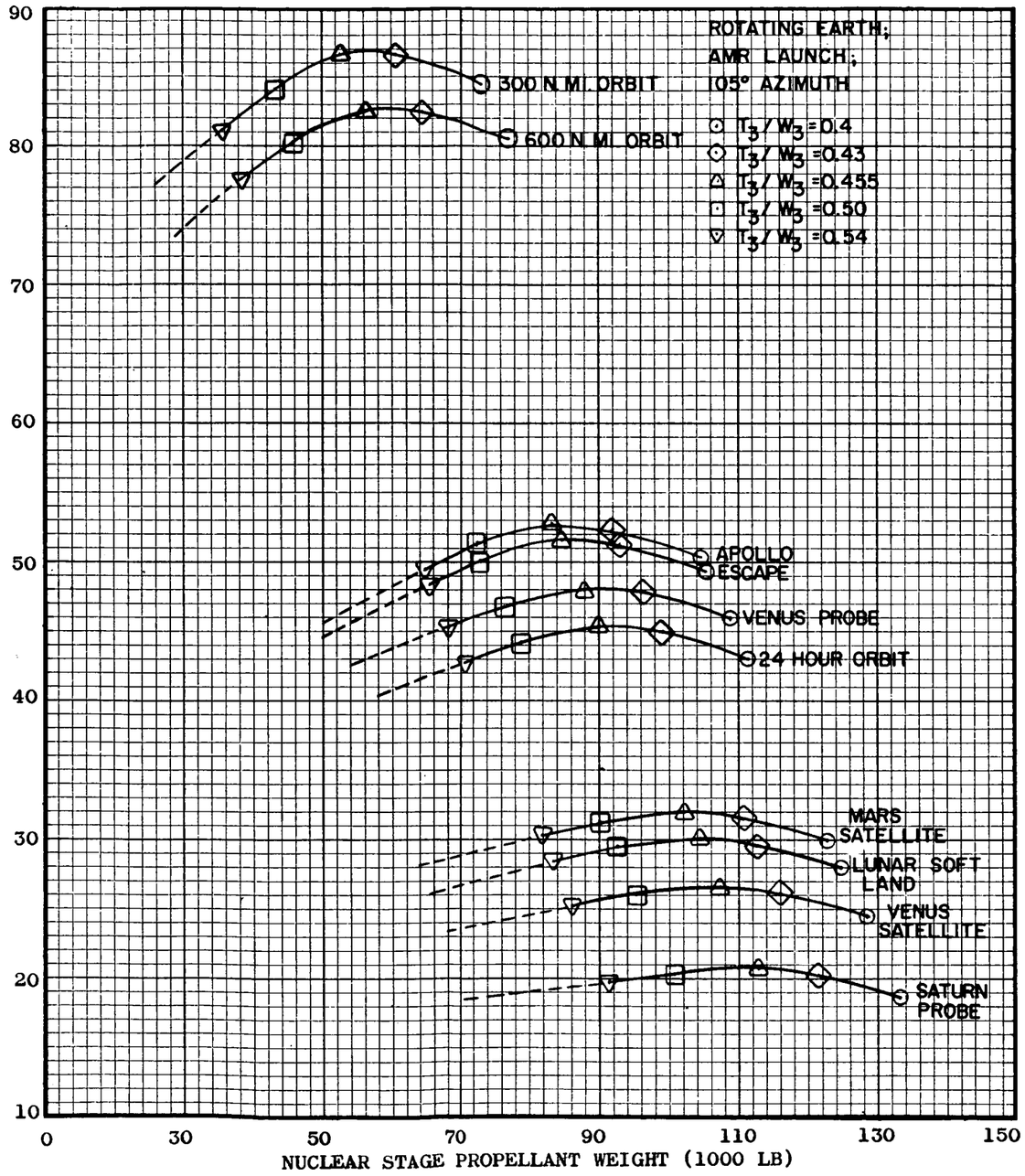

Figure D-3. Payload Vs Propellant Weight for S-I, S-II, SN-I

CONFIDENTIAL

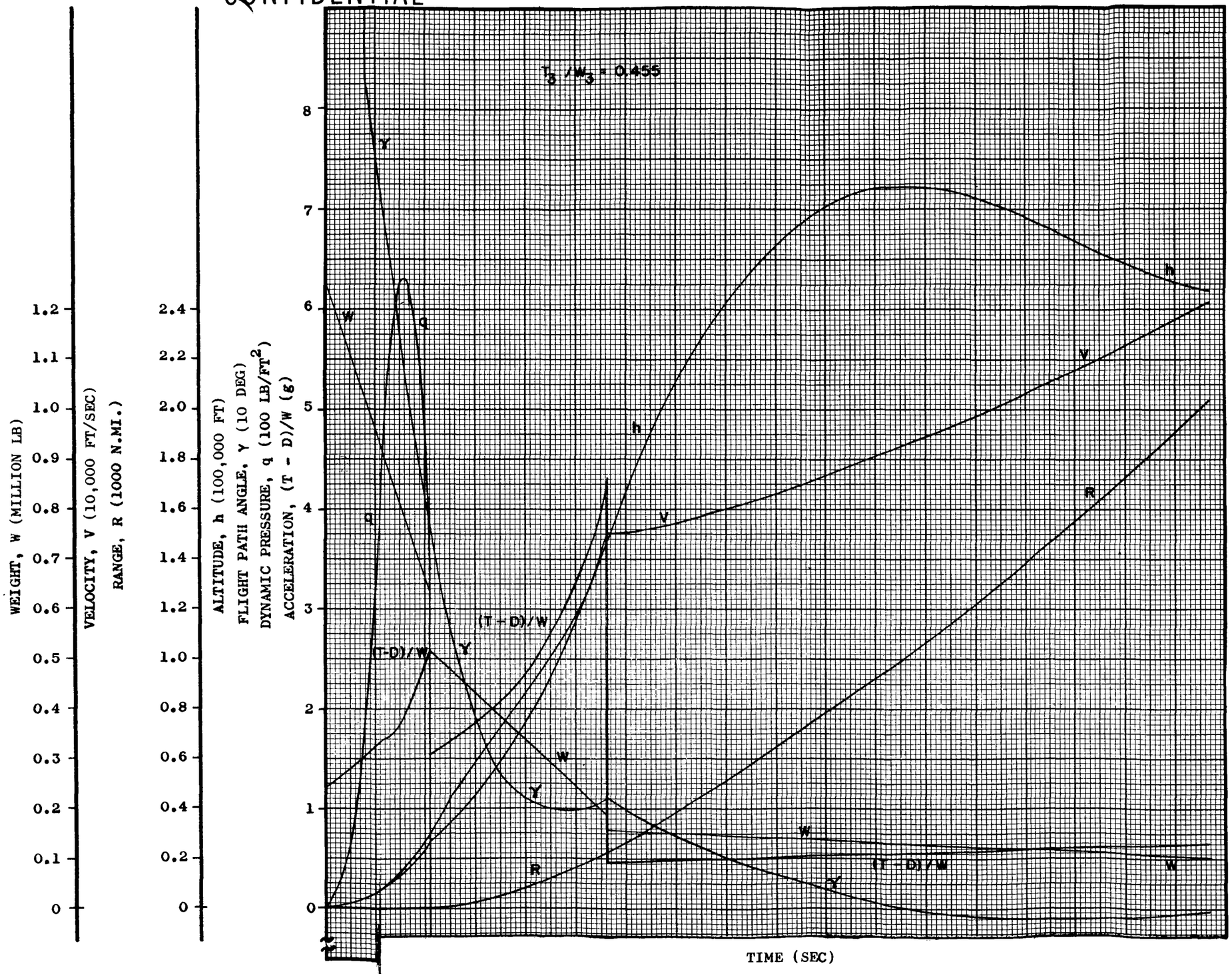

Figure D-4. Typical Launch Trajectory for S-I, S-II, SN-I

CONFIDENTIAL

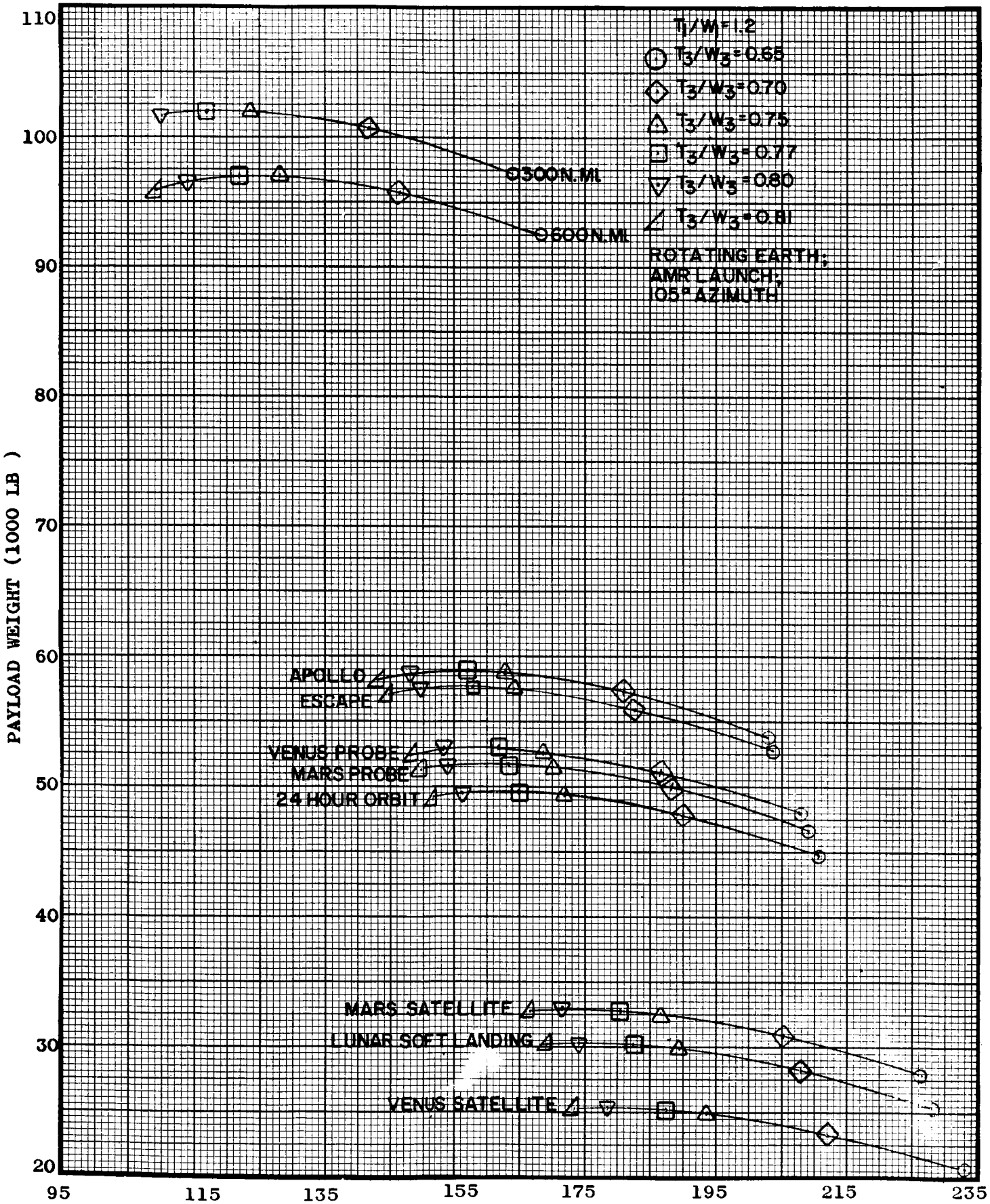

Figure D-5. Payload Vs Propellant Weight for S-I, S-II, and SN-II

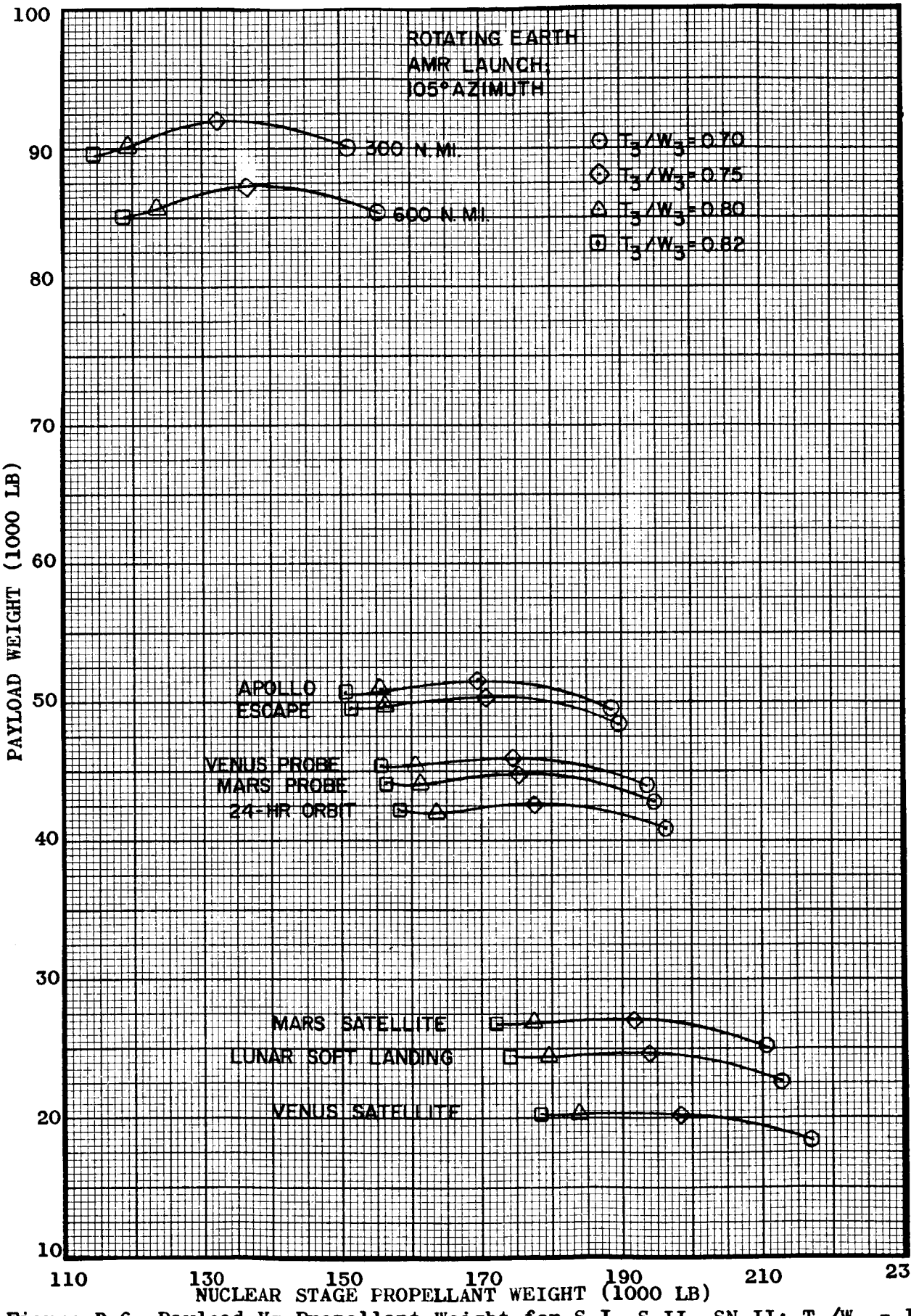

Figure D-6 Payload Vs Propellant Weight for S-I, S-II, SN-II; T_1/W_1 = 1.25

~~CONFIDENTIAL~~

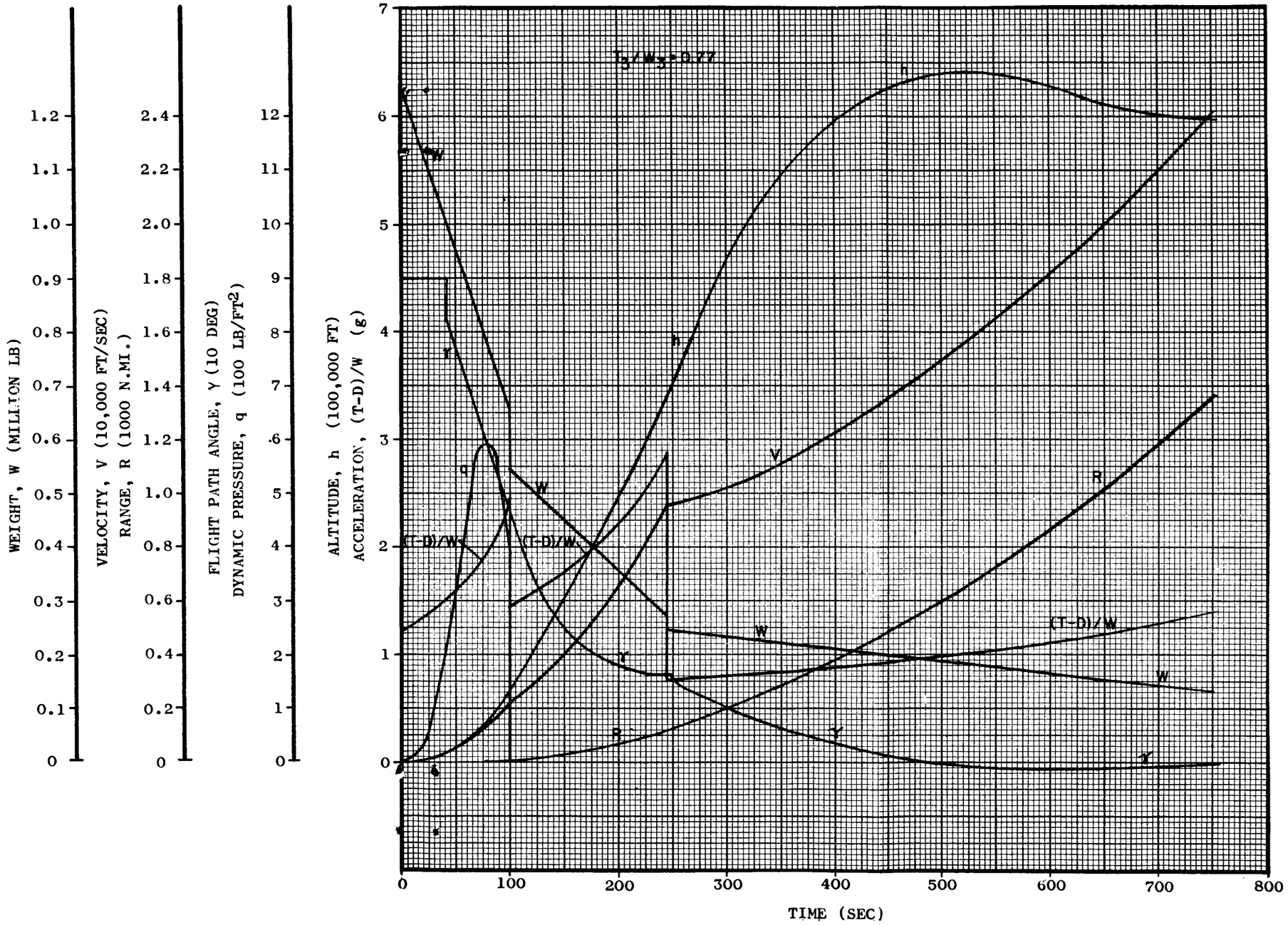

Figure D-7. Typical Launch Trajectory for S-I, S-II, SN-II

CONFIDENTIAL

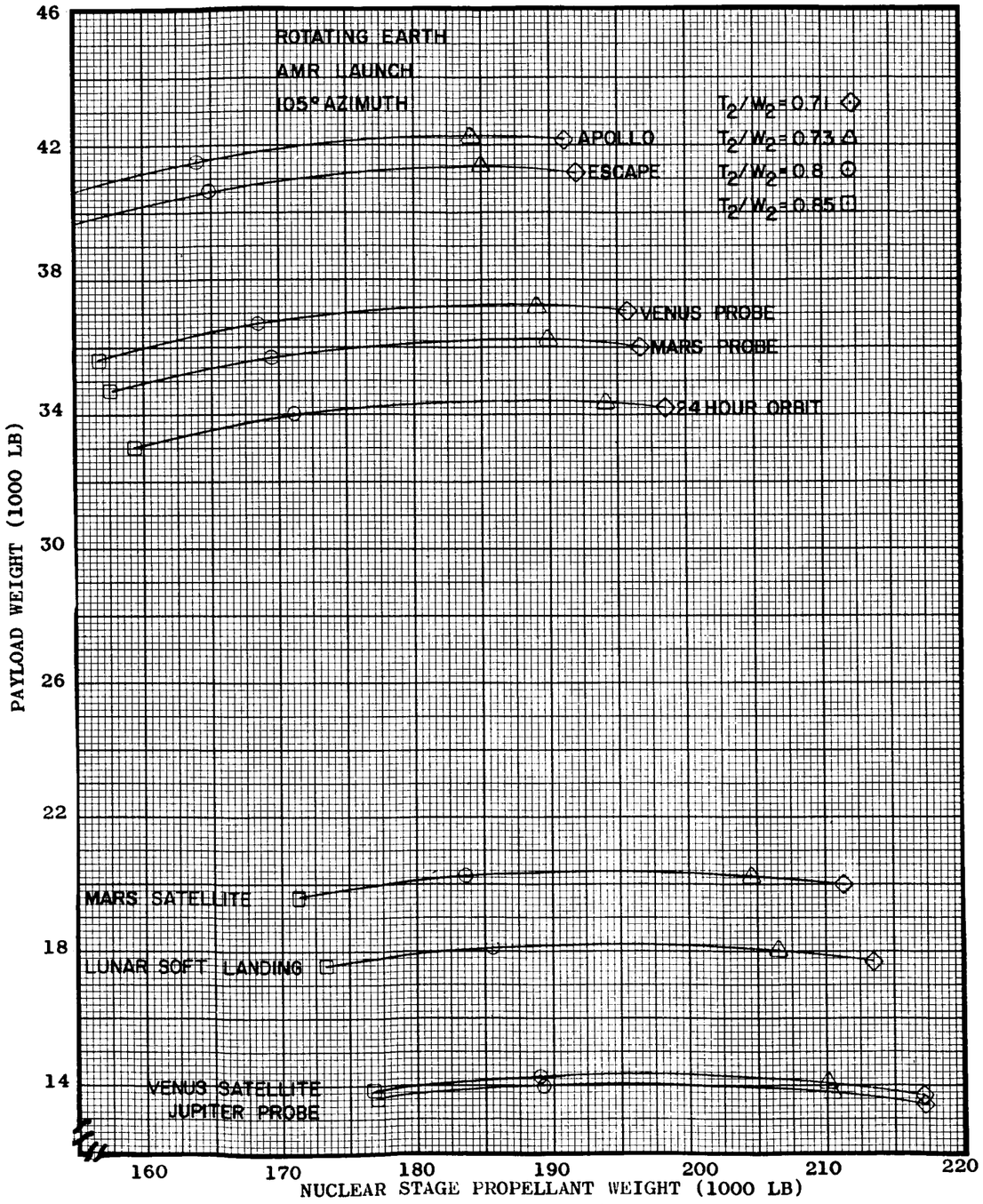

Figure D-8 Payload Vs Propellant Weight for S-I, SN-II

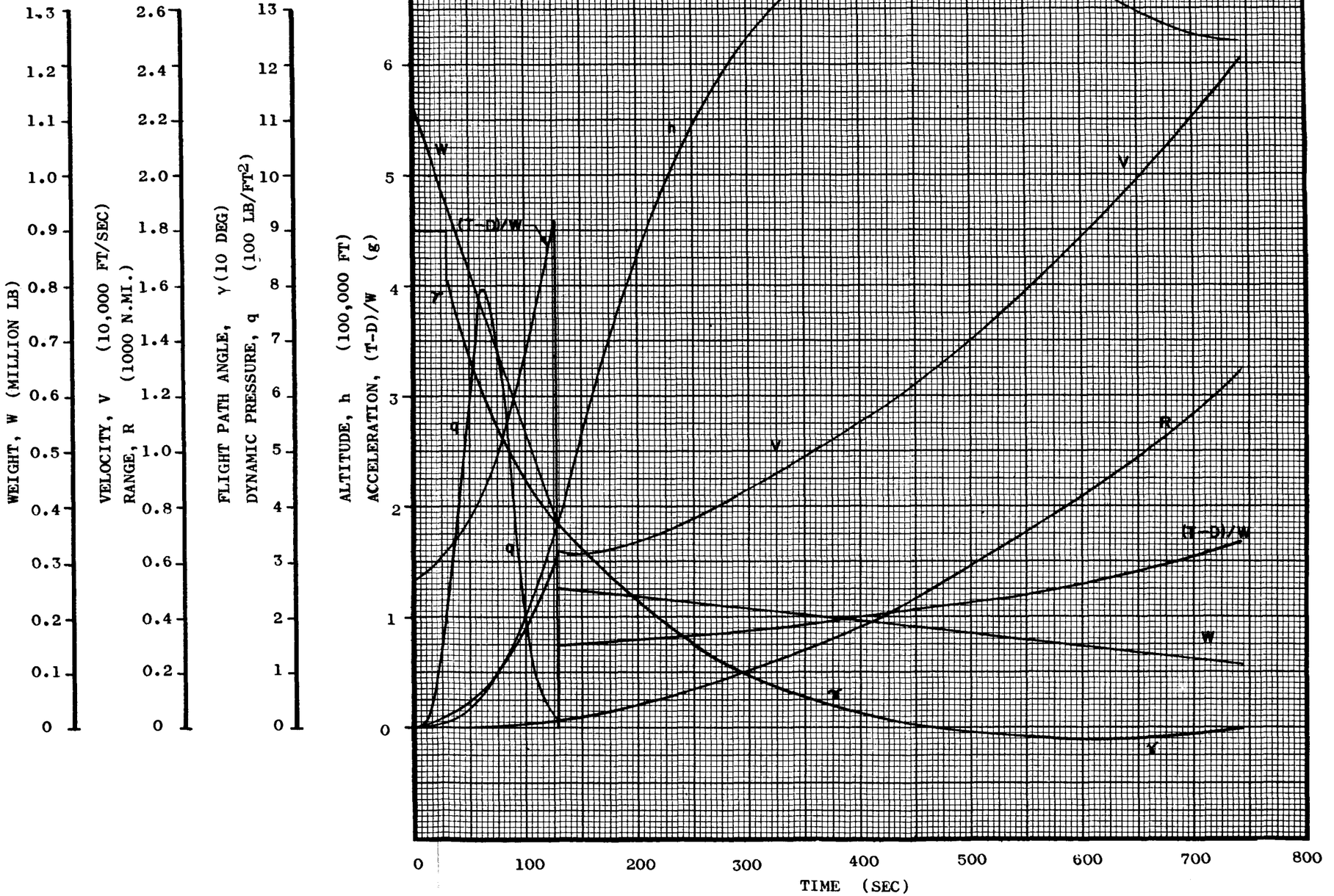

Figure D-9. Typical Launch Trajectory for S-I, SN-II

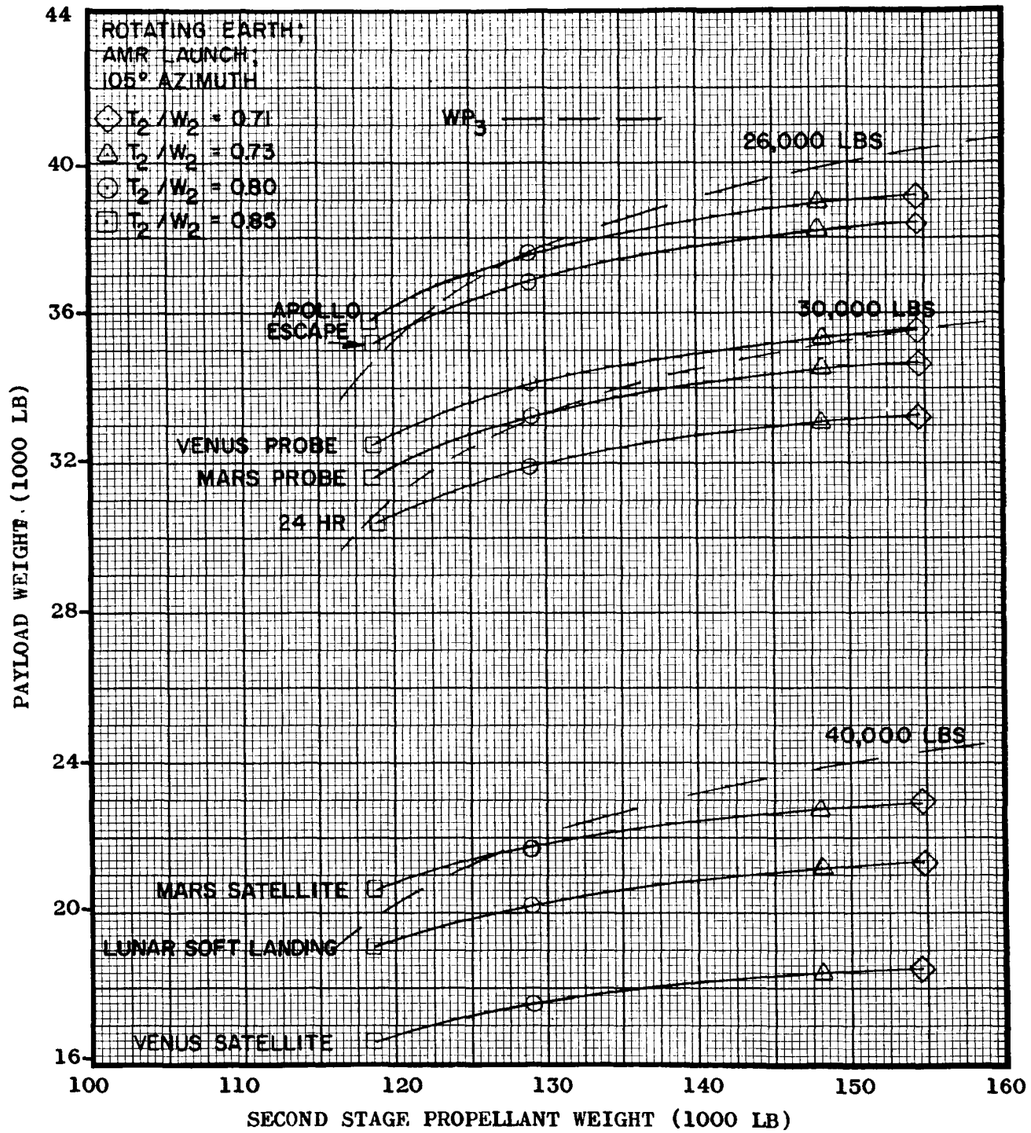

Figure D-10 Payload Vs Propellant Weight for S-I, SN-II (to orbit),SN-1

APPENDIX E

SHIELD MATERIALS

E.1 NEUTRON SHIELD MATERIALS

E.1.1 Beryllium Metal. Beryllium does not readily form alloys. The addition of 3-4 percent of beryllium oxide produces good properties. Brittleness is an undesirable property. Beryllium's brittle-to-ductile transition point is approximately 477°K (860°R). Polycrystalline beryllium exhibits essentially zero elongation at room temperature. The mechanical properties are strongly dependent on the purity of the metal and the degree of anisotropy brought about by working. Extruded castings have from 2 to 3 percent elongation parallel to the extrusion axis. Hot pressed powder has a 2-percent elongation in all directions. Extruded powder has from 15 to 20 percent parallel elongation, and 1 to 2 percent in the transverse direction. Extruded 200 mesh powder, cross-rolled at 1000°C (6 to 10) has 30 to 40-percent elongation in all directions. Generally, beryllium exhibits poor formability. The metal machines fairly well, somewhat like cast iron. It may be joined without sacrificing properties. The best physical properties may be developed through powder metallurgy techniques. No information is available on the effects of radiation on beryllium at cryogenic temperatures. There is reason to believe that damage would be accelerated. Beryllium is subject to nuclear reactions that produce gas atoms by transmutations within the metal lattice. These gas atoms cause blisters. The effects may be more severe at low temperatures. The reactions producing gas are:

a. $Be^9 (n, \alpha) He^6$

$He^6 \rightarrow Li^6$ (.083 sec half-life)

$Li^6 (n_t, \alpha) H^3$ (945 barns)

$2\alpha \rightarrow 2 He^4$

b. $Be^9 (n, 2n) Be^8$

$Be^8 \rightarrow 2 He^4$ (10^{-14} sec half-life)

c. Be^9 (γ , n) Be^8

$Be^8 \rightarrow 2\ He^4$

d. $Be^9 \rightarrow (\gamma , p) \rightarrow Li^8$

$Li^8 \rightarrow Be^8 \rightarrow 2\ He^4$

e. Be^9 (γ , n α) He^4 .

Beryllium is also subject to fast-neutron damage from interstitials, vacancies, displacements, and impurities. Irradiation at elevated temperature produced the following results:

INTEGRATED FLUX	HARDNESS-ROCKWELL B
0	68
2×10^{21} n/cm^2 (fast)	88
6×10^{21} n/cm^2 (fast)	100

INTEGRATED FLUX	TENSILE STRENGTH, PSI
0	33,000
1.5×10^{21} n/cm^2	49,000

A considerable quantity of physical property data is available in the literature. A small quantity is included here in Table E-1 for comparison purposes. The physical properties are highly dependent on the fabrication technique employed. Beryllium generally retains the same tensile and yield strength values at cryogenic temperatures that it has at 0°C.

Table E-1. Properties of Vacuum Hot Pressed Beryllium

STRUCTURAL PROPERTIES

TEST TEMPERATURE, °K	ULTIMATE TENSILE STRENGTH, PSI	YIELD STRENGTH 273°K 2% OFF, PSI	ELONG %
R.T.	33,000-51,000	27,000-38 000	1-3.5
373	32,000-49,000		3-8
473	30,000-43,000		6-15

373	24,000-35,000	12-30
673	22,000-27,000	19-40

Tensile Modulus	44.4×10^6 psi
Compressive Yield 0.2% offset	86,300 psi
Compressive Mod.	43.9×10^6 psi
Ultimate Shear	46,900 psi
Density, gm/cc	1.84

THERMAL PROPERTIES

Melting Point, °K 1558 ±10°K

Specific Heat (cal/gm/°C)

TEMPERATURE, °C	VALUE
-200	0
-100	0.2
0	0.4
100	0.5
200	0.55

Thermal Conductivity (cal/cm-sec-°C)

373	0.39
473	0.36
573	0.35

Coefficient of Thermal Expansion (in/in-°C)

25-100	12.3
25-200	13.3
25-300	14.0

E.1.1.1 Borated Beryllium Metal. Beryllium may be borated. The maximum workable mixture for the borated material is 97 percent by weight of beryllium and 3 percent by weight of boron. The boron is in the form of stable beryllium boride (Be_6B). Beryllium boride is dispersed through the beryllium and the mixture is compacted by employing powder metallurgy techniques. The addition of boron to a metal generally increases the damage from radiation effects. The

burn-up of boron results in a loss of properties. The reaction producing gas is:

$$_5B^{10} + _0n^1 \rightarrow _2He^4 + _3Li^7.$$

This reaction will increase the damage from thermal neutrons. Examination of radiation effects on beryllium metal and borated beryllium indicates more radiation damage in the borated material. Radiation damage at low temperatures would increase. When the boron content exceeds 3 percent by weight, the mechanical and thermal properties of borated beryllium are similar to ceramic materials. The addition of only 1 percent of boron results in a slight increase in beryllium tensil strength and a slight decrease in elongation.

E.1.2 Beryllium Oxide. Manufactured beryllium oxide is a powder of no value unless it is fabricated into a solid. Most of the conventional fabricating techniques, including dust processing, slip casting, ramming, and extrusion may be used to form BeO ceramics from powder. A common process is to press it at 1600-2300°C. Sometimes small amounts of alumina, silica, zirconium oxide, calcium oxide, or beryllium sulfate are added. Rough machining operations may be carried out in a presintered or low fired state (sintered at 1200 to 1500°C) using high speed or carbide tools. Machining to size after firing may only be accomplished by grinding with abrasive tools or cutting with diamond tools. Beryllium oxide could be damaged in a manner similar to the damage of beryllium. No information is available on the effects of radiation on beryllium oxide at cryogenic temperatures. The thermal conductivity of beryllium oxide is known to decrease with increasing radiation dosage. The thermal conductivity was reduced 40 percent at room temperature by an integrated flux of 1.3×10^{20} n/cm^2. Beryllium oxide would be subject to both thermal neutron and fast neutron damage. As in the case of beryllium metal, the fabrication techniques determine the physical properties. This is clearly shown in Table E-2.

Table E-2. Physical Properties of Beryllium Oxide at Room Temperature

DENSITY, GM/CM^3	COMPRESSIVE STRENGTH, PSI	MODULUS OF ELASTICITY, PSI
1.8	10,000	5×10^6
2.0	12,000	10×10^6
2.2	20,000	15×10^6
2.4	35,000	24×10^6
2.6	60,000	33×10^6
2.8	120,000	43×10^6
3.0	---	52×10^6

THERMAL PROPERTIES OF BeO

Melting Point 2823 ± 25°K

Specific Heat (cal/gm/°K

TEMPERATURE, °K	VALUE
173	0.0125
273	0.229
373	0.321
673	0.438

Mean Coefficient of Linear Expansion in./in./°K, 10-6

TEMPERATURE, °K	VALUE
298-373	5.5 ± 1.0
298-573	8.0 ± 0.6
298-873	9.6 ± 0.8

Thermal Conductivity:

(Density 2.6 - 2.7)

(Cal/cm-sec-°K)

TEMPERATURE, °K	VALUE
373	0.5
473	0.4
673	0.2
873	0.1

E.1.2.1 Borated Beryllium Oxide. Since borated beryllium oxide classifies as a ceramic, and beryllium-boron intermetallics are known to exist, there is reason to believe that good borated beryllium oxide ceramics are possible. No published information could be located on borated beryllium oxide. The addition of boron to a metal generally increases the damage from radiation effects. The burn-up of boron results in loss of properties. The reaction producing gas is:

$$_5B^{10} + _0n^1 \rightarrow _2He^4 + _3Li^7$$

This results in an increase in the damage from thermal neutrons. Examination of radiation effects on beryllium metal and borated beryllium indicates more radiation damage in the borated materials. Radiation damage at low temperature would be accelerated. The physical properties of borated beryllium oxide are not available.

E.1.3 Lithium Hydride. Lithium hydride is a white, crystalline solid which may be fabricated into blocks. It is essentially stable in an inert atmosphere up to 975°R. Since lithium hydride reacts readily with water, it must be canned.

Lithium hydride shields are usually constructed from a series of pressed blocks. The lithium hydride blocks are fabricated by either hot or cold pressing. The major difference is in the amount of force required to compress the lithium hydride power. A 500°C hot-pressed block will reach 98 percent of theoretical density with only 2500 psi, while cold pressing requires 20,000 psi to approach 92 percent of theoretical density. An inert atmosphere must be maintained over the heated die, since the material is extremely sensitive to atmospheric moisture and oxygen at elevated temperatures. It is possible to obtain partial relief from some of the fabrication difficulties if a binder (organic or metallic) can be used with the lithium hydride.

Large crystals retain their gross structure when exposed to pile rediation in the order of 10^{17} n/cm^2. However, polycrystalline

aggregates develop from thermal spikes. Irradiation damage is accelerated at liquid nitrogen temperature. Irradiation of cast and pressed lithium hydride confined tightly in stainless steel containers resulted in negligible pressure or expansion effects after irradiation of 6×10^{18} n/cm^2 at 535°C. Unconfined lithium hydride will expand when exposed to integrated fluxes as low as 10^{16} n/cm^2 at 315°C. The physical properties are highly dependent upon the method of fabrication (see Table E-3).

E.1.4 Polyethylene. The term "polyethylene" is not descriptive of a definite structure. Generally, two types of polyethylene are available for the production of shields. They are the low density polyethylene, containing a greater proportion of chain branches, and high density (or linear) polyethylene, containing considerably less chain branches. The linear polyethylene has the highest hydrogen content per unit of volume and has more desirable physical properties.

Polyethylene is produced as a powder and must be hot-compression molded. For this reason, it is normally used in sheet form. The material forms well and is easily machined. The bonding of polyethylene to itself or another material is extremely difficult.

Table E-3. Physical Properties of Lithium Hydride

MECHANICAL PROPERTIES:	
Density g/cm^3 at 20°C	
Theoretical	0.82
Commercial Pressed Powder	0.7
Commercial Loose Powder	0.3
Compressive Strength	
Cold Pressed	10,800 psi
Hot Pressed	24,300 psi
Modulus of Elasticity	
Cold Pressed	7.1×10^6 psi
Hot Pressed	10.8×10^6 psi

Modulus of Rigidity	
Cold Pressed	$2.7 - 3.1 \times 10^6$ psi
Hot Pressed	$4.3 - 5.0 \times 10^6$ psi

THERMAL PROPERTIES:

PROPERTY	VALUE
Melting Point, °C	680
Specific Heat (g-cal/g-°C)	
0°C	0.98
50°C	1.07
Thermal Conductivity (cal/cm-sec-°C)	0.0222
Coefficient of Thermal Expansion (in/in/°C)	3.9×10^{-5}
Decomposition Point (Equilibrium H_2 pressure, mm Hg)	
600°C	110 mm Hg
700°C	300 mm Hg
800°C	700 mm H

Some success, however, has been claimed with newer adhesives.

Polyethylene is affected by both gamma and neutron irradiation, but shows very little physical property change up to a dose of 1×10^7 rads. However, the material will liberate gases during irradiation. The primary effect of irradiation beyond 1×10^7 rads is a decrease in elongation and an increase in brittleness. The melting point is increased upon exposure to 5×10^6 rads. The low-temperature properties would be expected to be severely adversely affected.

The low melting point of polyethylene makes the physical properties highly dependent upon temperature. Table E-4 summarizes its properties.

Table E-4. Physical Properties of Polyethylene

STRUCTURAL PROPERTIES (at 298°K)	
Density	0.96 gm/cc
Tensile Strength (psi)	4000
Compression Strength (psi)	2440
Shear Strength (psi)	3600
Elastic Modulus (psi)	19,000
THERMAL PROPERTIES:	
Melting Point, °C	105-120
Specific Heat (g-cal/g/°C	0.55
Thermal Conductivity (cal/sec-cm-°C)	0.00062-0.00083
Coefficient of Thermal Expansion (in/in/°C)	11-18 x 10^{-5}
Heat Distortion Under Pressure of 264 psi	50°C

E.1.4.1 Borated Polyethylene. Refer to the information for "polyethylene." Both low-density and high-density polyethylene may be borated. Boron carbide (B_4C) is normally used. The fabrication procedures for borated polyethylene are essentially the same as those for polyethylene. The effects of radiation will be increased through the addition of boron. The reaction:

$$_5B^{10} + {}_0n^1 \rightarrow {}_2He^4 + {}_3Li^7$$

produces damage from thermal neutrons, adding to the damage from fast neutrons and gamma rays. The heat produced from this reaction is appreciable. Some properties typical of a 6-percent borated polyethylene may be illustrated by the following.

STRUCTURAL PROPERTIES AT 298°K	
Density	1.0 gm/cc
Tensile Strength	3930 psi

Compression Strength	2700 psi
Shear Strength	3560 psi

E.1.5 Graphite. Graphite has one of the most anisotropic structures known. The physical properties of the final product are highly dependent upon the choice of raw materials and the method of forming. Graphite also possesses unique refractory properties.

Items fabricated from manufactured carbon and artificial graphite are made of a filler and binder mass which is shaped and heat-treated. The filler and binder are mixed at a suitable temperature. The resultant mass is formed by molding or estrusion and is then baked at 1450°F to 2750°F to set the binder. Subsequently, the shape may be impregnated with coal tar pitch or reheated. The reheat temperature may be 4200°F to 5500°F, and the resultant product, if made of petroleum coke bonded with coal tar, is artifical graphite. Nuclear grade graphite requires control of the impurities in the petroleum coke and the coal tar. Pyrolitic graphite may be produced by the deposition of carbon from a vapor phase onto a substrate which is maintained at elevated temperatures.

Commercial graphite products are relatively soft and can be machined with wood or metal working tools. However, for machining large quantities of reactor-grade graphite, carbide cutting tools have been more satisfactory. In milling operations, the life of a tungsten-carbide cutting tool is shorter than that of the same cutter used on ordinary steel. Graphite may be joined by using molybdenum disilicide as a weld material and heating the assembly to 3900°F.

Since graphite is anisotropic, it is susceptible to structural damage. The lattice vacancies within the planes causes a marked alteration in the vibrational frequencies in their vicinity, and the interstitial atoms will cause a buckling of the adjacent lattice planes which affect the lattice spacing. The bending of the lattice planes by individual interstitials and complexes of interplanar atoms tends to restrict the normal easy gliding of

one lattice plane over another. Irradiated graphite can become extremely hard and has good abrasive qualities.

Most commercial graphites show large physical distortion under room temperature irradiation; however, certain graphites have shown excellent dimensional stability. Under room temperature irradiation the thermal conductivity decreased markedly. The bending strength, compressive strength, and modulus of rupture increase rapidly. The thermal conductivity of transverse-cut CSF graphite at 30°C is expressed below

INTEGRATED FLUX	RATIO OF IRRADIATED/CONTROL
2.5×10^{19} n/cm^2	0.22
7.75×10^{19} n/cm^2	0.091

Modulus of Elasticity

INTEGRATED FLUX	RATIO OF IRRADIATED/CONTROL
5×10^{18} n/cm^2	1.5
1×10^{19} n/cm^2	2.0

As previously discussed, the physical properties are highly dependent upon the method of fabrication. Some examples are given in Table E-5.

Table E-5. Physical Properties of Graphite

STRENGTH PROPERTIES:	
Tensile Strength, psi, 273°K	
AUF (Parallel)	3500 psi
AGX (Parallel)	2200 psi
AGHT (Parallel)	2200 psi
AGHT (Perpendicular)	600 psi
Com. Graphite C-18 (Per. & Para.)	2400 psi
Pyrolytic (Parallel)	14,000 psi (302°K)
(Note: Graphite increases in tensile strength with increasing temperature.)	

Flexural Strength at 775°K		
Pyrolytic (= to plane)		22,000 psi at 302°C
Pyrolitic (⊥ to plane)		1,500 psi at 302°C
Compressive Strength at 775°K		
Pyrolitic (= to plane)		14,000 psi at 302°C
Pyrolitic (⊥ to plane)		68,000 psi at 302°C
Elastic Modulus		
Com. Elec, Graphite, 0°C		
Parallel		1.2×10^6 psi
Perpendicular		0.4×10^6 psi
Density, gm/cm^3	Normal	1.5 - 1.9
	Pyrolytic	2.2

THERMAL PROPERTIES:

Melting Point, °C	Sublimes 3200°C
Specific Heat, cal/g/°K	
TEMPERATURE: °K	
298	0.172
400	0.237
600	0.336
800	0.396
1000	0.428

Thermal Conductivity (373°K)	
cal/cm-sec-°C	
Average Parallel	0.45
Average Perpendicular	0.30
Coefficient of Thermal Expansion	
in/in-°C @ 25°C	
Average Parallel	2×10^{-6}
Average Perpendicular	6×10^{-6}

E.1.5.1 Borated Graphite. Borated graphite is a complex of boron carbide (B_4C) suspended in graphite. The material can be borated to approximately 20 percent by weight of boron. The boron carbide is blended with the petroleum coke and its semifluid binders during the initial stages of the graphite manufacturing process. A stand-

ard grade of graphite is commonly used in this process but the manufacutrers indicate that high purity reactor grade can be borated without difficulty. The presence of the boron would undoubtedly increase the radiation damage through the reaction:

$$_5B^{10} + {}_0n^1 \rightarrow {}_2He^4 + {}_3Li^7$$

Thermal and fast neutrons would then produce damage.

The following information on the physical properties of borated graphite at 298°C is available.

Density	1.65 gm/cc
Flexural Strength	1500 psi
Tensile Strength	2000 psi
Compression Strength	2000 psi
Melting Point	Sublimes 3650°C

Borated pyrolytic graphite may produce better properties. Refer to the section on graphite for additional properties.

E.1.6 Zirconium Hydride. Zirconium hydride is a dark gray solid. It has a face-centered cubic crystalline structure.

The structural material may be prepared in two ways. The zirconium hydride may be vacuum sintered, or the pure zirconium metal may be hydrided. The latter method allows a variable amount of hydrogen addition. The vacuum sintering method usually involves heating for three hours at 2300°F and subjection to 65 tons/in.^{2} pressure. Massive hydriding of the metal requires that the zirconium be fabricated to its desired shape and then be heated in a purified hydrogen atmosphere. Machining should be performed in an inert atmosphere.

The intermetallic $ZrH_{1.86}$ was irradiated at 45°C to the integrated flux:

Thermal 2.45×10^{18} n/cm^2

Fast 2.45×10^{17} n/cm^2

No changes were noted in the physical properties. No information is available on irradiation at cryogenic temperatures.

The physical properties will be dependent on the method of fabrication. The vacuum sintering and the massive hydriding technique both introduce the posibility of variable properties. Typical properties are shown in Table E-6.

Table E-6. Physical Properties of Borated Graphite

TYPICAL STRUCTURAL PROPERTIES:	
Density - gm/cc	5.6 to 6.5
Compressive Strength	93,200 psi
Yield Strength	32,400 psi
Tensile Strength	
800°F	40,000 psi
1200°F	9,000 psi
1600°F	4,000 psi
THERMAL PROPERTIES:	
Melting Point, °C	1857
Decomposition Point - Air - °C	430
Heat Capacity, gm-cal/gm-°C	
TEMPERATURE, °C	
0-100	0.0823
100-200	0.1006
200-300	0.117
300-400	0.1273
400-500	0.1466
Thermal Conductivity (cal/sec-cm-°C)	0.52
Coefficient of Thermal Expansion (in/in/°F)	
TEMPERATURE, °F	
1000	6.5×10^{-6}
1600	5.0×10^{-6}

E.2 GAMMA SHIELD MATERIALS

E.2.1 Depleted Uranium. Depleted uranium is produced by removing almost all of the U^{235} from natural uranium. Tuballoy, a common designation for this material, has an alpha-to-beta transformation at 666°K, and a beta-to-gamma transformation at 771°K. The U^{235} content usually exceeds 0.4 percent by weight.

Uranium may be fabricated by a variety of methods including rolling, extrusion, forging, and powder-metallurgy. The material may be easily machined.

Nuclear radiation effects on depleted uranium will be highly dependent upon:

a. The fast neutron flux in the depleted uranium shield.
b. The amount of U^{235} remaining in the uranium.
c. The thermal cycling of the shield.

The fast neutron damage to uranium is the result of two effects:

a. The production of interstitials, vacancies, and displacements.
b. The fast neutron fission effects.

The energy of fission fragments is approximately 100 Mev. These produce additional interstitials, vacancies, displacements, and impurities. Studies of natural uranium have shown that below 600°K (1077°R) there is little volume change from fission damage, but above 700°K (1299°R) significant volume changes can result. The swelling is attributed to atomic volume increase, inert gas production, and the formation of gas pockets.

Experimental evidence indicates that irradiation effects may start to appear at integrated fluxes as low as 1×10^{15} n/cm^2 but probably would not start to become significant until integrated fluxes of 1×10^{17} n/cm^2. An atomic burnup of 7×10^{-6} atom/atom appears to be a point at which fission damage could appear and add to fast-neutron damage.

Uranium is subject to pronounced elongation from thermal cycling. The elongation is influenced by the maximum temperature, range of temperature, length of time at elevated temperature, heating and

cooling rates, and prior mechanical treatment (See Figure E-1).

The physical properties are highly dependent upon the prior metallurgical history. Because of the inconsistent nature of uranium, it is difficult to present precise representative tensile data. The situation is further complicated by a low proportional limit. It is difficult to determine offset yield strength by the standard initial tangent method. The testing temperature has a marked effect on the properties (see Figure E-2). Refer to Table E-7.

Table E-7. Representative Structural Properties of Alpha Uranium at 298°K

Density	19 gm/cc	
Compression Strength	Variable 100,000 psi	
Tensile Strength & Elongation		
Case	60,000-85,000 psi	5-10%
Gamma Extruded	85,000-120,000 psi	10-18%
Beta Rolled	80,000-95,000 psi	10-15%
Alpha Rolled-Alpha Annealed	80,000-110,000 psi	10-15%
Alpha Rolled-Beta Annealed	55,000-65,000 psi	6-10%
Thermal Properties		
Melting Point, °C	856	
Specific Heat (cal/gm-°C)	0.028	
Thermal Conductivity - 25°C (cal/sec-°C)	0.061	

The thermal expansion of uranium is highly dependent upon crystallographic directions. For this reason it is best to express the mean volumetric expansion (see Table E-8).

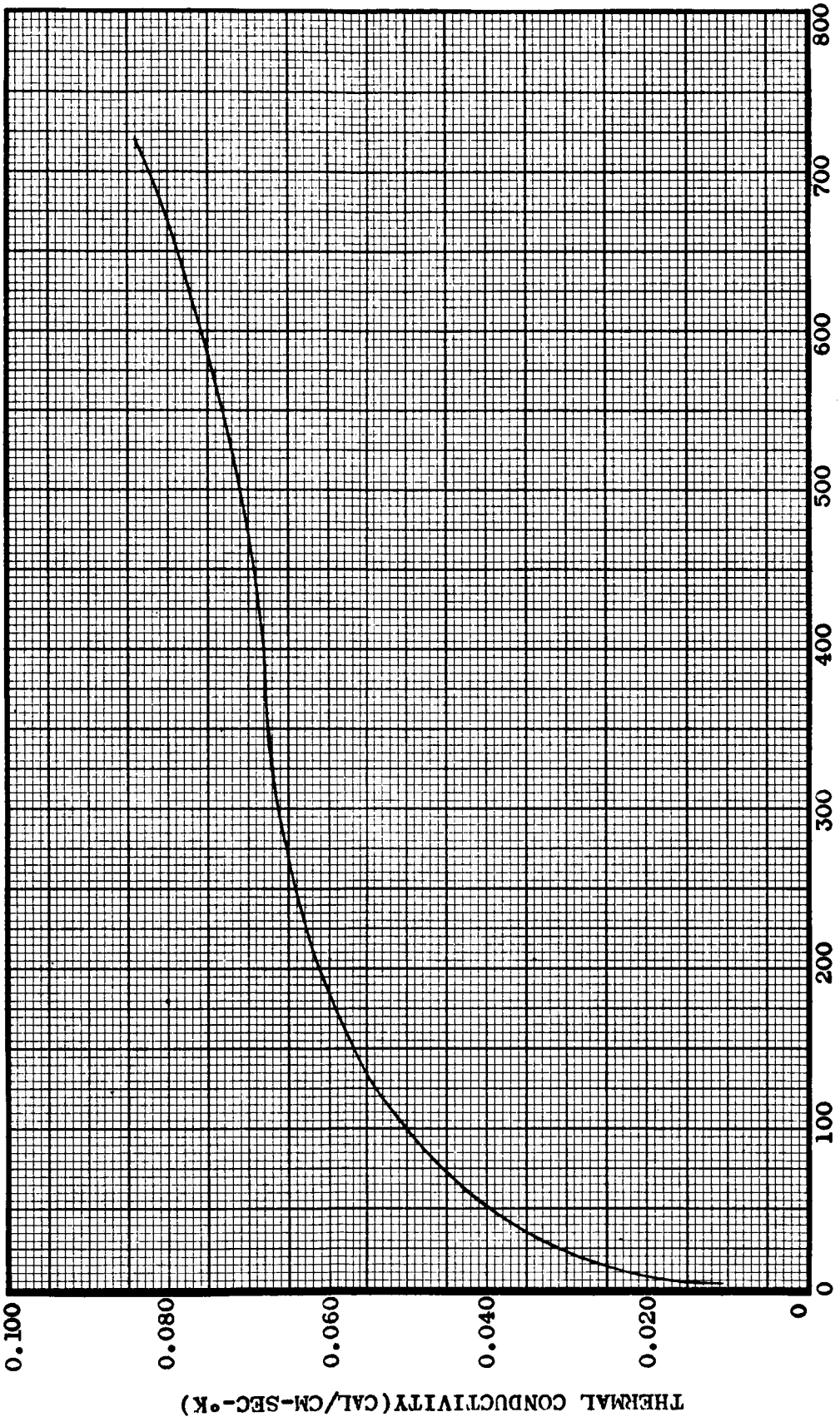

Figure E-1. Uranium Thermal Conductivity Vs Temperature

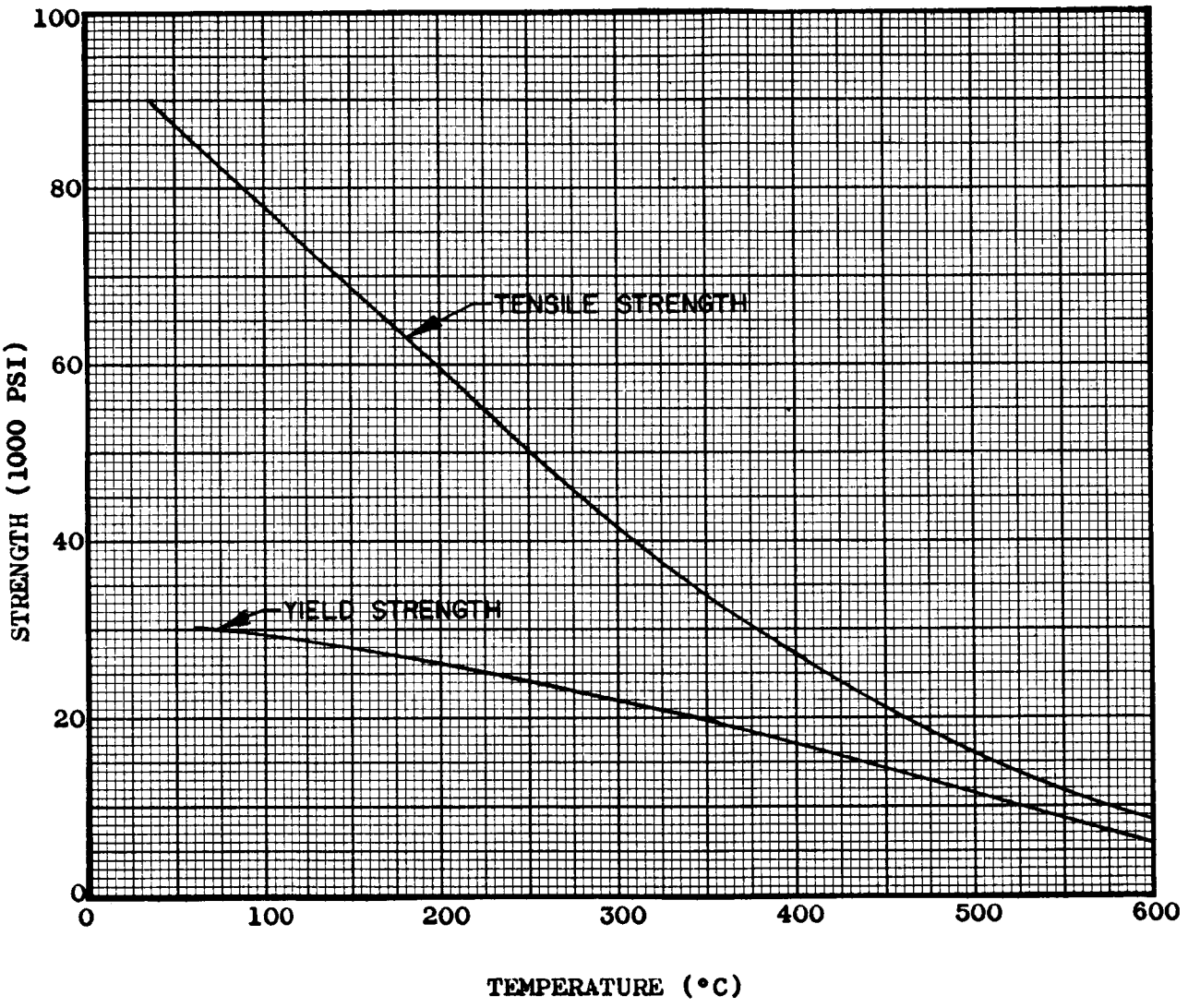

Figure E-2. Uranium Tensile and Yield Strength Vs Temperature

Table E-8. Mean Volumetric Thermal-Expansion Coefficients of Alpha Uranium (in/in/°C x 10^{-6})

TEMP RANGE °C	VALUE
0-50	43.44
0-100	44.41
0-150	45.62
0-200	46.62
0-400	52.17

E.2.2 Stainless Steel. A large number of stainless steels are available for shields. The properties of the steels at cryogenic temperatures will be determining factors in the selection.

The wide variety of methods of fabricating stainless steel are well known and no detailed discussion will be attempted. Stainless steels in general and austenitic grades in particular are more difficult to machine than ordinary steel. Special treatments of welds are required when unstabilized stainless steels are joined.

Extensive data is available regarding the effects of nuclear radiation on stainless steels, including data at cryogenic temperatures obtained by General Dynamics/Astronautics. Representative data at non-cryogenic temperatures is presented in Table E-9.

Table E-9. Yield Strength of Various Stainless Steels at an Irradiation Temperature of 200°F

ALLOY	CONDITION	YIELD STRENGTH 0.2% OFFSET, PSI
301	Control	38,400
	Irrad	87,000
302	Control	33,840
	Irrad	84,000
305	Control	32,100
	Irrad	71,400
347	Control	37,000
	Irrad	96,500

Irradiations at -423°F of CRES 301 and CRES 310 to an integrated flux of approximately 2 x 10^{17} n/cm^2 indicated very little change in yield strength, but some decrease in ultimate tensile strength.

There is extensive data on physical properties of stainless steels at cryogenic and elevated temperatures. This data will not be repeated in this report. Reference National Bureau of Standards, Cryogenic Materials Handbook, and General Dynamics Reports. Thermal properties are indicated below.

THERMAL PROPERTIES

Melting Point (°C)	1400
Thermal Conductivity (cal/sec-cm-°C)	0.4-0.6
Mean Coefficient of Thermal Expansion (in/in/°C)	9-12 x 10^{-6}

E.2.2.1 Borated Stainless Steel. Refer to the section on stainless steels. Borated stainless steel is essentially a two-phase alloy composed of a complex borite phase in an austenitic chrome-nickel-iron matrix. A common alloying stainless steel is CRES 304. Most of the commercial materials contain less than 2 percent by weight of boron. The effectiveness of the boron can be increased by enriching the boron with B^{10}. Some have felt that vacuum-melted borated stainless steel alloys are superior to air-melted alloys. Concentrations of boron above 1.0-1.5 percent by weight have been difficult to forge or work on rolls. Casting of plates of higher boron concentration has been considered. When boron containing stainless steels are welded there is a tendency for the boron to diffuse into the weld, resulting in difficulties.

The addition of boron to stainless steel greatly increases the radiation damage. The primary reaction is:

$$_5B^{10} + {}_0n^1 \rightarrow {}_2He^4 + {}_3Li^7 .$$

The resulting damage is therefore from both thermal and fast neutrons. In addition, there is the possibility of gas build-up.

Cracks of unknown origin are found in material experiencing high burn-up. The addition of boron to stainless steel generally increases the tensile strength and decreases the elongation. The effect on yield strength is variable (refer to Table E-10).

Table E-10. Physical Properties of Irradiated Boron Steels

NATURAL BORON CONTENT	INTEGRATED FLUX N/CM^2	ULTIMATE TENSILE, PSI	YIELD STRENGTH 0.2% OFFSET, PSI	ELONG., %
1.18	0	96,200	39,000	18
	3.4×10^{20}	151,000	130,000	Slight
1.64	0	101,000	42,000	14
	0.97	117,400	96,000	Slight
1.8	0	84,200	41,300	8
	5.8	148,600	134,000	None
2.04	0	47,000	47,000	5.4
	7.3	137,000	138,000	None

E.2.3 Tungsten. Tungsten is attractive as a gamma shield because of its high density. It is generally produced by powder-metallurgy techniques. Pressures of 25,000 psi are employed. The compacts are presintered at 1800 to 2200°F. Machining of tungsten is difficult and most finishing is done by grinding. Rolling is possible at 1300 to 1400°C and welding is possible, but the joints are brittle.

Little data is available on the effects of radiation on tungsten. Exposure to 1×10^{19} n/cm^2 thermal neutrons and 5×10^{19} fast neutrons did not affect the hardness of tungsten. The density decreased from 0.1 to 0.15 percent. After a similar exposure tungsten wire decreased in tensile strength approximately 22 percent.

The physical properties of tungsten are highly dependent on the previous history of the metal (refer to Table E-11).

Table E-11. Properties of Tungsten

Representative Structural Properties	
Density	16-18.5 g/cm^3
Tensile Strength	16,000 psi
Thermal Properties	
Melting Point, °C	3410 ± 20
Specific Heat (cal/gm/°C)	
20°C	0.033
1000°C	0.036
Coefficient of Linear Expansion per °C	
25-500°C	$4.45\text{-}5.0 \times 10^{-6}$
Thermal Conductivity cal/sec-cm-°C	
-183°C	0.46
-78°C	0.41
0°C	0.40
1225°C	0.28

E.2.3.1 Tungsten Alloys. Tungsten alloys provide the density of tungsten plus improved fabrication properties. The available alloys include:

ALLOYS	COMPANY
Mallory 1000	(P.R. Mallory Co.)
Hevimet	(General Electric)
Fansteel 77	(Fansteel Metallurgical Co.)
Densalloy	(Welded Carbode Tool Co.)

The alloying materials are primarily nickel and copper.

The alloys are fabricated by employing powder-metallurgy, and the alloys are machinable. Radiation damage data for these alloys is not available. Refer to the section on tungsten. Physical property data is available on numerous alloys of nickel, copper, and tungsten (refer to Table E-12).

Table E-12. Properties of Tungsten Alloys

Representative Structural Properties	
Density - gm/cc	
Mallory	16.96
Fansteel 77	17.2
Tensile Strength, psi	
Mallory 1000	112,000
Fansteel 77	70,000
Hevimet	118,000
Yield Strength (psi) - Mallory 1000	75,000
Compressive Strength (psi)	162,000
Representative Thermal Properties	
Melting Point, °C	3400
Thermal Conductivity, cal/cm-sec-°C	0.235
Coefficient of Thermal Expansion, in/in/°C	5.4×10^{-6}

E.2.4 Lead. Lead is extensively used as a gamma shield, but generally has poor structural properties for a metal. It is easily cast, very ductile, and may be fabricated by standard metal-working techniques. Lead is often employed in sheet form. Normally, lead is supported by structural support members when it is used. Bonding to the structural support may be accomplished by lead burning, chemical adhesives, or fasteners. Composition is extremely important in lead-bonding operations. There is no data which indicates that lead is affected by radiation exposure. Lead is alloyed to improve mechanical properties. Antimony is commonly used (see Table E-13).

Table E-13. Physical Properties of Lead

Representative Structural Properties

	COMM. PURE	4% ANTIMONIAL
Density gm/cm^3	11.34	11.04
Tensile Strength (psi)	2380-2630	4020
Yield Strength		
20°C	1180-1320	- -
-300°C	1200-1400	- -
Elastic Modulus	2.56 x 10^6 psi	- -
Stress to Produce Creep 1% per Year	200 psi	

Thermal Properties

	COMM. PURE	4% ANTIMONIAL
Melting Point, °C	327	300
Specific Heat, gm-cal/g/°C	0.031	0.0318
Thermal Conductivity, cal/sec-cm-°C	0.083	0.073
Coefficient of Thermal Expansion, in/in/°C	2.9 x 10^{-6}	27.8 x 10^{-6}

E.2.4.1 Lead-plastic Matrix. The employment of lead-plastic matrix material in some instances might be more desirable than lead or another shielding material. Finely divided lead is incorporated into a plastic material prior to molding. The lead content is believed to be limited to approximately 95 percent by weight. The resulting material is fabricated by plastic or elastomer fabrication techniques dependent upon the organic material employed.

Radiation damage will depend upon the plastic used. Maximum radiation resistance would probably be accomplished by using epoxy, phenolics, or aromatic polyurethanes as the organic binder.

Detailed physical property data is not available for lead-plastic matrix materials suitable for shielding applications. It is believed that the tensile strength would be less than 1000 psi and the elongation approximately 100 percent.

E.2.5 Bismuth. Bismuth has a relatively high density and may be applicable as a gamma shield. The material is brittle and is usually cast into the desired shapes rather than being machined or rolled. Little radiation damage information is available. Bismuth metal exposed to an integrated fast neutron flux of 2×10^{18} n/cm^2 (E >1 Mev) at 100°C showed no indication of radiation damage. Physical properties are summarized in Table E-14.

Table E-14. Properties of Bismuth

Mechanical Properties:		
Density		9.8 gm/cc
Thermal Properties:		
Melting Point, °C		271
Specific Heat, cal/g		
Temp, °C		
-150	0.0264	
-100	0.0273	
0	0.0291	
20	0.0294	
100	0.0304	
Coefficient of Thermal Expansion, in/in/°C		
Temp, °C		
-180 to +15	12.98×10^{-6}	
19 to 101	13.45×10^{-6}	
Thermal Conductivity, cal/sec-cm-°C		
Temp, °C		
-186	0.025	
0	0.0177	